國 立 交 通 大 學

電 機 與 控 制 工 程 研 究 所

碩 士 論 文

用於窄波段腸胃道影像之遞迴式解馬賽克演算法研究

Study on Recursive Demosaicking Algorithm for Narrow-band Gastrointestinal Image

研究生：賴貫康

指導教授：董蘭榮　博士

中華民國九十七年九月

Study on Recursive Demosaicking Algorithm for

Narrow-band Gastrointestinal Image

Advisor: Dr. Lan-Rong Dung

Graduate Student: Kuan-Kang Lai

September 2008

Graduate Institute of Electrical and Control

Engineering

National Chiao Tung University

Hsinchu, Taiwan, ROC

Study on Recursive Demosaicking Algorithm for Narrow-band Gastrointestinal Image

Graduate Student: Kuan-Kang Lai   Advisor: Dr. Lan-Rong Dung

Department of Electrical and Control Engineering

National Chiao Tung University

Abstract

The objective of this dissertation is to develop a demosaicking algorithm which is suitable for narrow-band gastrointestinal image. We present a hybrid recursive demosaicking method which utilizes the inter-plane and the frequency correlation efficiently. Processing the iteration can improve the image quality and reduce the aliasing and color artifacts. However, too many iterations may cause the zipper effect and tend to de-saturate the color of image. So we set a stop criterion to judge the image is suitable and stop the iteration adaptively. For Bayer CFA, we compare the proposed method using several test images with some existing techniques. Our method performs better both in visual and by the performance measurement indexes. In order to process the demosaicking algorithm for narrow-band gastrointestinal image, the CFA need to withdraw one G component. Through our discussion, we found the CFA which been arranged similar to Bayer pattern can achieve better results. Compare to conventional Bayer CFA, our proposed demosaicking algorithm can lose only 1.0185dB in average by only three samples in 2-by-2 CFA block.

用於窄波段腸胃道影像之
遞迴式解馬賽克演算法研究

學生：賴貫康　　　　　　指導教授：董蘭榮　博士

國立交通大學
電機與控制工程學系研究所

摘要

　　這篇論文的目標是發展一個專為窄波段腸胃道影像設計的解馬賽克演算法。我們提出了一種遞迴式的演算法，這個方法有效的利用了三原色平面間的相關性以及頻域上高頻頻段的高度關聯性。透過利用疊代的方式，可以提升影像的品質並且消除一些解馬賽克容易產生的失真或是顏色上不正常的變化。然而，使用太多次疊代可能會造成拉練效應並且可能會使整張影像的顏色變得不飽和。為了解決這個問題，我們設立了一個停止疊代的機制，這個機制能判斷這張影像是否適合用疊代來改良品質，適合的話再執行，並且適應性的停止疊代。針對傳統的貝氏彩色濾光陣列，我們和一些已經現存的方法做比較，透過一些常用的測試影像，我們的方法無論在視覺上或是評估指標上都表現得比較好。為了把這樣的演算法適用於窄波段腸胃道影像，彩色濾光陣列裡的綠色成分會被窄波段藍光替換。透過諸多的討論，把貝氏彩色濾光陣列裡的綠色成分替換掉，這樣的排列效果是最好的。針對這個特別設計的彩色濾光陣列，我們的演算法在一個二乘二的彩色濾光區塊中只有三個取樣成分下，還是可以把影像解馬賽克出來。跟傳統的貝氏彩色濾光陣列比較，品質上只損失了 1.0185dB。

Acknowledgement

I would like to thank my advisor, Dr. Lan-Rong Dung for all his support and earnest teaching. During these two years, he instructed me industrious and gave me directions when I get stuck in difficulty. His innate ability to discuss problem on the basis of scientific intellect also taught me the manner of dealing and research.

Many thanks to Mr. Ying-Yi Wu and Mr. Hsiang-Neng Hsieh in Chung-Shan Institute of Science and Technology for their assistance and guidance. Without their help, the narrow-band experiments can not work on. Also, I wish to thank B. K. Gunturk, X. Li and K. Hirakawa for providing their demosaicking programs. Their skills and coding style give me to reap no little benefit

Besides, I would like to thank my classmates, Yunling, XT, Kong, Landers, J, Weiyin, ICE, Cosmic, Eric and Aaron in this lab. In the last two years, they helped me review my work, resolve my confusion in study, encourage me, and help me sort things out.

At last, I want to thank my parents, Hudson and Angela and my brother, Peter for providing suggestions in every decision I made; Joanna, for being there with me, reminding me in details and understanding my personality.

To all persons concerning me, thank you.

Contents

List of Tables

List of Figures

viii

Chapter 1 *Introduction*

1.1 Demosaicking

The natural images contain three different spectral channels, i.e. red (R), green (G) and blue (B). However, each individual optical sensor is able to capture only one single color of the three color bands. That's means we need three sensors to get the full color in one pixel. In order to reduce the cost and size, most digital still cameras (DSC) today using a single-chip CCD or CMOS sensor array whose surface is covered with a color filter array (CFA). The CFA is located between the lens and the sensors. The following figure describes this system.
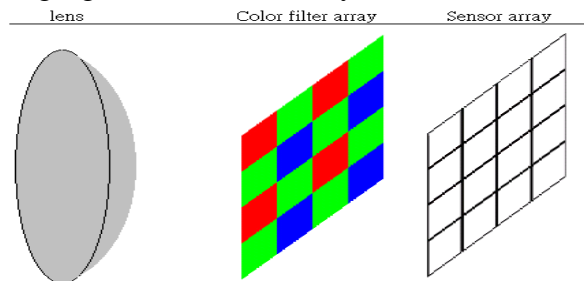
Fig. 1.1 Optical system in digital still camera

According to this arrangement, there is only one color be sampled of each pixel. To get a full-color image, other colors must be estimated or interpolated from the neighboring samples. This color filter array interpolation is known as demosaicking.

Bayer pattern [1] is the most popular type of color filter array. It has four possible arrangements which can be described as Fig. 1.2.
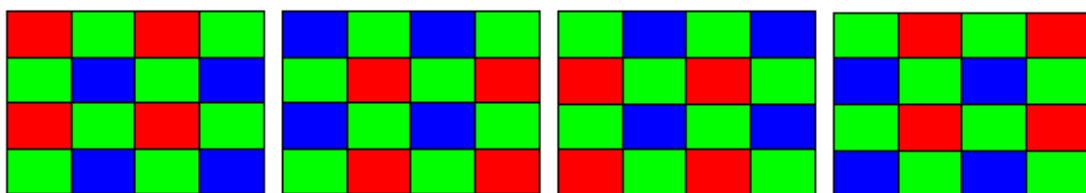
Fig. 1.2 Four possible arrangements of Bayer CFA

As we see, G samples are obtained by a checkerboard lattice and R and B samples are obtained by a rectangular lattice. The G pixels are sampled at a twice rate than others as the human eye is more sensitive to G compared to R and B.

However, we choose the first arrangement of Fig. 1.2 for the whole discussion.

1.2 Narrow-band Image

For the last few years, endoscope has been spread widely for diagnosing abnormal pathological changes. Except for its less invasive, for the most important point, it is capable of identifying early-stage lesions of cancers. Early detection and treatment of cancers has become a demanding goal in the diagnosis field.

Physician detects those abnormal regions based on the color, shape, and the surface pattern of patient's mucosa. Throughout the judgment, if the lesions is observed and identified as a tumor, treatment is decided among surgery or other therapy. In order to afford complete cure by endoscope, lesions must be found at the early stage. Therefore, for the sake of better identifying of abnormal findings and more accurate diagnostic performance, several investigators and researches have been done for the same object, the improvement of the endoscope system and the enhancement of its observation.

Narrow-band Image (NBI) [28], [29] can achieve the goal we mentioned above. This kind of endoscope enables physicians to detect tumors in the deep layer of mucosa. Under the narrow-band light, due to the absorption of hemoglobin, the fine vessels of mucosa can be displayed clearer than under the white light. K. Gono in [27] had proved that center wavelengths of 415nm and 540nm enable to emphasize images of vessels. According to the experiments of backside mucosa of human tongue, as shown in Fig. 1.3, the 415nm image can display the structure of fine vessels at the
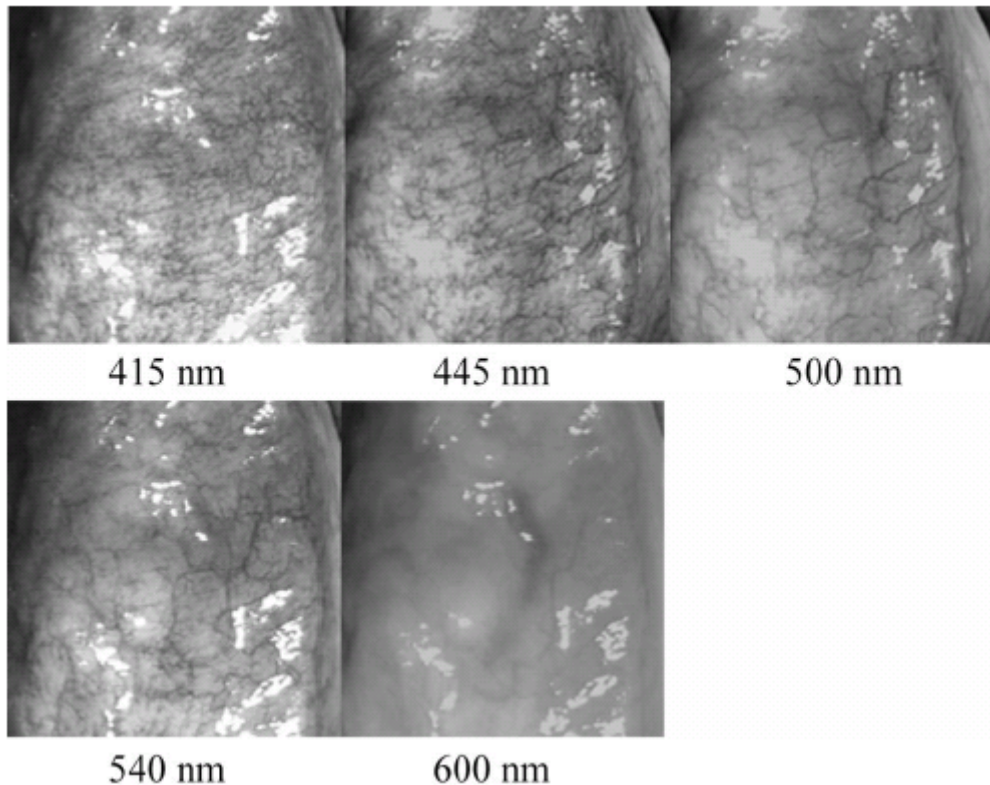
Fig. 1.3 Images of backside mucosa of human tongue under the light of different wavelengths.[1]

superficial layer, and the 540nm image can present the vessel structure in the relatively deep layer of mucosa if the living tissue is observed under narrow band light 415 and 540nm. Besides, Gono also proved that under the same center wavelength 415nm, broad-bandwidth (100nm) of 415nm light is not enough to show the fine vessels of mucosa. However, narrow-bandwidth (60nm) of 415nm light can increase the contrast of micro vessels in superficial layer.

Nowadays, NBI has been popularly used in endoscope throughout the world. Olympus developed the first endoscope system and now its latest platform "EVIS LUCERA SPECTRUM" imaging platform (SPECTRUM) offers not only NBI, but also provides autofluorescence image (AFI) and infrared image (IRI). All of them are HDTV image quality. In order to display NBI in color image, SPECTRUM is designed so that 415nm image is assigned to B and G plane and 540 nm image is assigned to R plane. This assignment of the final image let the fine vessels are displayed in brownish-red, and thicker vessels in the deep layer are displayed in cyan color. Physicians observed the abnormal findings when making overall judgment, they can switch to NBI mode to investigate any pathological changes through the high-contrast image of the vessels.

---

[1] This figure refers to [27]

1.3 Motivation

The object of our experiment is to design the gastrointestinal capsule endoscope with NBI image. The sensor of existing NBI system has two layers of optical filters [27]. The first layer is mode selector for choose the vision mode of white light image (WLI) or NBI. The second layer is used to sense RGB color. However, it is not practical to place two layers of sensors to capture RGB and NB color individually. Similar to the reasons of most commercial digital cameras today, demosaicking is a way to solve this difficulty. The following figure describes the existing system diagram. We use two different light sources: white light and NB light. And the CFA
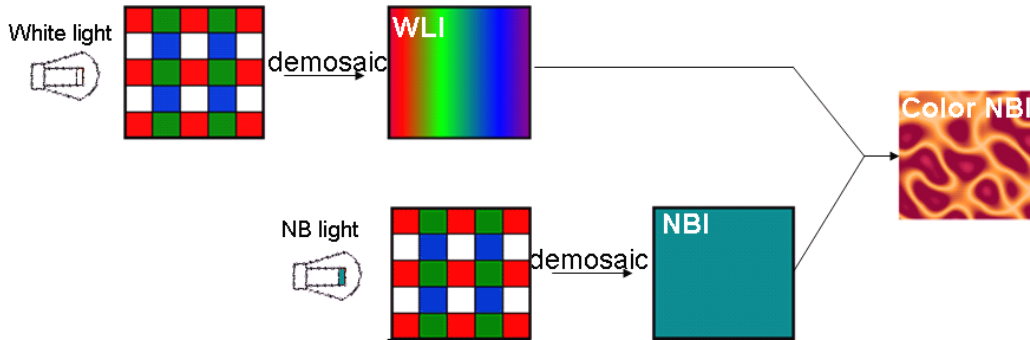
Fig. 1.4 Sensor structure of existing capsule endoscope system

we used is similar to Bayer pattern but withdrawing one G sample, as shown in Fig. 1.4. When the capsule endoscope captures the image, these two sources are emitted continually. While the source is white light, the CFA is open for sense mosaic RGB color. Otherwise, the sensor is record the N information under gray-level resolution at the location of withdrawing G.

Now we desire to develop a demosaicking algorithm with satisfied results so that we can make use of it on the endoscope system. Demosaicking problem has been studied and researched broadly in recent years. Lots of demosaicking algorithms are also presented continually. The simplest way is the bilinear interpolation. Although it is easy to implement, the reconstructed image can not maintain the edge information and high-frequency component. Later, many characteristics or correlations have been utilized in order to get better results. Some may aim to suppress artifacts around edge, and some may exploit the strong inter-plane frequency correlation to improve the high-frequency component. Among several ways, recursive methods can achieve a better result [2]. The iteration had been widely used in demosaicking since the closed-loop estimation can approximate the original color values and hence enable to reduce these artifacts. However, too much iteration may cause the zipper effect and tend to de-saturate the color of image [20]. Besides, in our research, we found that some output images can be closed to the original one after many times of iterations

but some can not. If we can diagnose the image is suitable to execute the iteration beforehand, we can decide to enter the image to the recursive step or not. Thus, the discussion of how to adaptively use the iteration as we proceeding demosaicking is also an important part in this dissertation.

1.4 Outline

This thesis is structured as below:

Chapter 2   Background

This chapter makes a review of color fundamentals and some color models, which builds the foundation of following discussion. Besides, some measurement indexes which used to compare the outputs of image processing are introduced as well. Then, briefly introductions of some existed demosicking methods which are popularly discussed throughout this field are described.

Chapter 3   Demosaicking using Iterative Approach

This chapter presents the demosaicking methods which utilize the iteration to improve image quality. A discussion about the number of iteration is also shown in this chapter. Following is the demosaicking algorithm we proposed and the plan concentrates on how to adaptively use the iteration is take on, too. At last, some comparisons are made on test image and highlight their pros and cons.

Chapter 4   Demosaicking Problems of Gastrointestinal Narrow-band Image

In this chapter, we modify the demosaicking algorithm in order to process on narrow-band gastrointestinal image. Besides, the CFA is no longer Bayer CFA and need to withdraw one G component. Discussions about the effects and performances of different CFA arrangements are also presented.

Chapter 5   Conclusion and Future Work

This chapter concludes this dissertation and its findings. The possible improvements are also described in this chapter.

Chapter 2 *Background*

2.1 Introduction

As we research or conduct experiments on image, the color fundamentals are the basis for the whole processing. Color is an important part of human expression, likewise, it also define the way we recognize the image. In general, we sense color owing to the spectrum of light source and the reflectance of observed object. This relationship is depicted as Fig. 2.1. Note that the spectrum of observer is obtained from the convolution of waveform of light and reflectance.
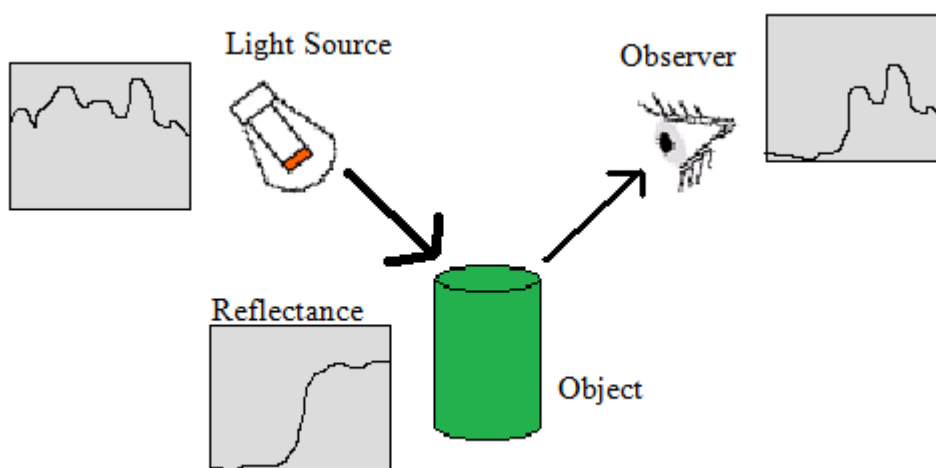
Fig. 2.1 The relationship between the light source and observer

The output waveform of Fig. 2.1 is actually color and brightness we absorbed. Retina, located the inner layer of human eye, is in charge of the vision of human. It contains two different kinds of receptors, cones and rods. Cones provide the color vision under normal illuminance, however, rods provide the monochromatic vision under low illuminance environment [31]. Typically, only features of light could be detected by cones, that is, specific range of wavelength spectrum would be catch by humid vision system. What image processing has done is virtually base on this specification.

Next, when image processing has finished, regardless of image compression or transmission is, we need to check the result is the same to original one. If negative, we should know how much does the output image differ from the input? Some performance measurement indexes have been used to assess this issue. Discussion of these indexes would be shown as following.

The rest of this chapter gives briefly introductions of some existed demosicking methods. These discussions in sequence can also get a glimpse of the process of its evolution and progress in the demosaicking field

2.2 Color Models

So far, the perception of color in human brain and its interactions are still unclear and ambiguous. However, the physics of color can be defined by the results of experiments and theory. The first experiment was conducted by Newton in 1666 [30]. He observed that the rays after sunlight passing the prism of glass are not white light. This detection is opposed to the argument which said sunlight is just a homogeneous entity that almost everyone believed at that time. Newton continued his experiment; he made a small hole in a dark room. The sunlight passes through the hole and forms the direct rays in the dark room. After that, taking an optical prism and placing it in front of the hole, he observed the light radiate into a spectrum, as shown in Fig. 2.2.
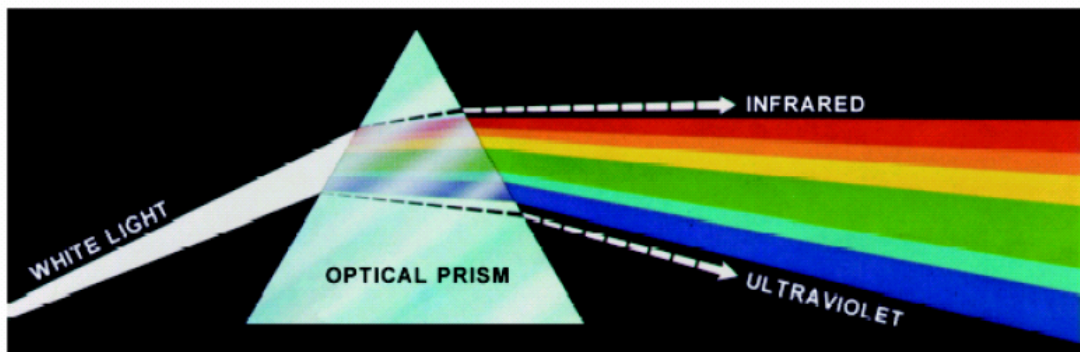
Fig. 2.2 Color spectrum seen by passing white light through a prism[2]

The spectrum is actually the specification we mentioned last section. We display the spectrum in detail in Fig. 2.3. This range is called the visible light and the wavelength of this range is roughly from 400nm to 700nm. This range is just a minor part of the electromagnetic spectrum.

---

[2] This figure refers to [32] and courtesy of the General Electric Co., Lamp Business Division.
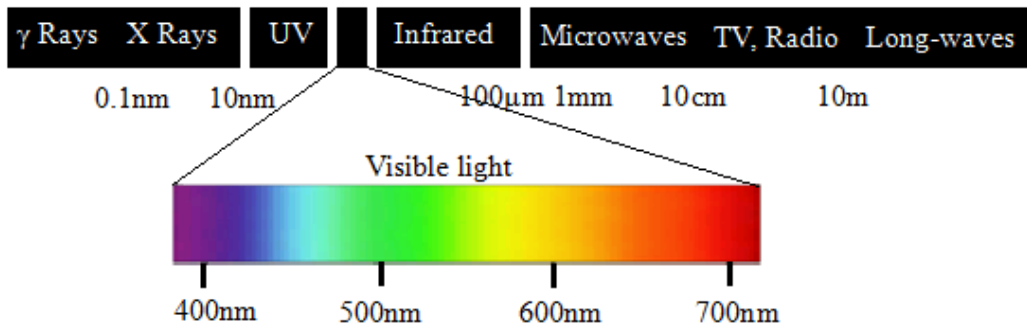
Fig. 2.3 Wavelengths of visible light of the electromagnetic spectrum

The trichromacy which introducing the principle of three color measurements was began in the 18th century. This theory showed that people need three different photoreceptors to create the visible range of color. Those receptors are called cone cells with different absorption. Therefore, the evaluation of color should require three different spectral weighting functions. That is to say, by linear combination of three primaries, it can produce a region in the color space. The following statement will introduce some color models which popularly used.

2.2.1 RGB Color Model

This color model comes from the color matching experiment conducted by Grassmann in 1853. The experiment schematic was described as Fig. 2.4.
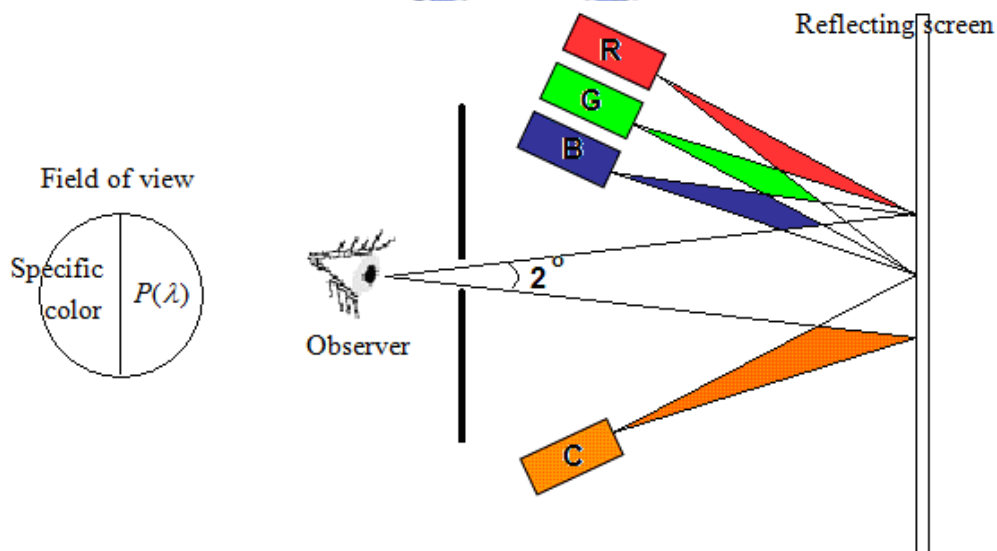
Fig. 2.4 The experimental schematic of trichromatic color matching

8

And this experiment has some important requirements as below:

1) The three primaries must have linearly independent spectra.
2) The angular size of the viewing field is limited to 2 degree.
3) The observer must have normal color vision.

Note that the RGB color model does not define three primaries. All discussions below are relative to the primary colors. When the exact primaries are defined, the color model then specified as absolute, such as sRGB or Adobe RGB.

According to the trichromacy theory, spectral color can be matched by the three primaries. Equation 2.1 showed this combination.

$$P(\lambda) = r(\lambda) \cdot R + g(\lambda) \cdot G + b(\lambda) \cdot B \qquad (2.1)$$

The target of this experiment is let $P(\lambda)$ match the specific color spectrum. The observer checks color to be the same in the field of view. Different wavelength should have different weighting functions. International Commission on Illumination (CIE) in 1931 summarized the various experiment results from various primaries and different observers. They obtained the wavelengths of three primaries were chosen as R (700nm), G (546.1nm) and B (435.8nm) [34][35]. Based on the same principle, the experimental result is depicted as Fig. 2.5. These functions are called color matching function.
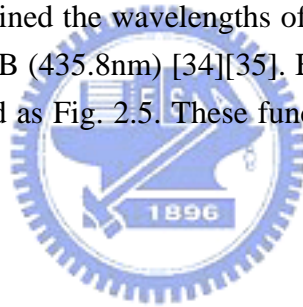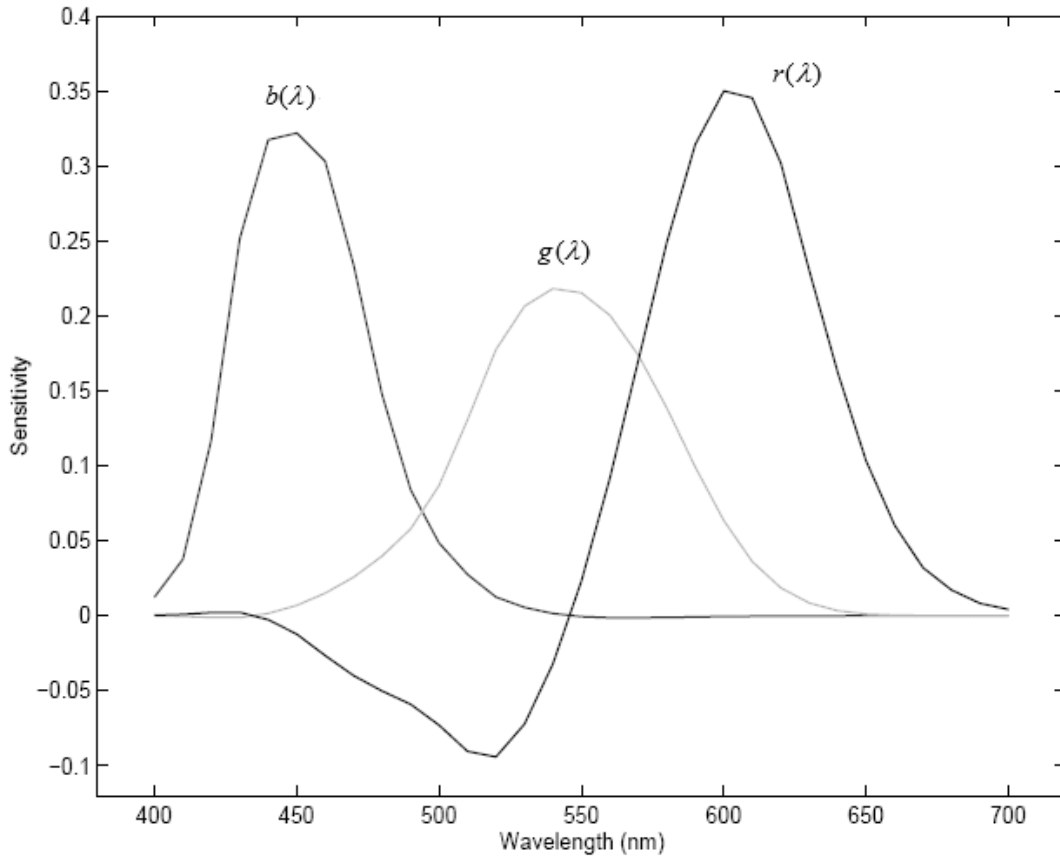
Fig. 2.5 The CIE 1931 RGB color matching function

According to the figure above, the color matching function can be used to determine the amounts of R, G and B which needed to compose any available color. The values of R, G and B are regard as tristimulus values. Nevertheless, some tristimulus values of RGB color model are negative. That's because some color spectrum can not be combined by equation 2.1. At that condition, one light source of three primaries needs to be moved to another side in order to match the specific color. The equation then becomes equation 2.2.

$$P(\lambda) + r(\lambda) \cdot R = g(\lambda) \cdot G + b(\lambda) \cdot B$$
$$\Rightarrow P(\lambda) = -r(\lambda) \cdot R + g(\lambda) \cdot G + b(\lambda) \cdot B$$

(2.2)

These negative values of tristimulus are not desirable as the electron beams are not able to produce "negative" input.

Nowadays, the RGB color model is the most common way to encode color in computing. The mainstream of quantization number is 8 bits each primary color. RGB values encode in 24 bits per pixel (bpp) and represent the intensities of R, G and B using the range from 0 to 255. The color cube shown in Fig. 2.6 describes the 24bpp

RGB color space.
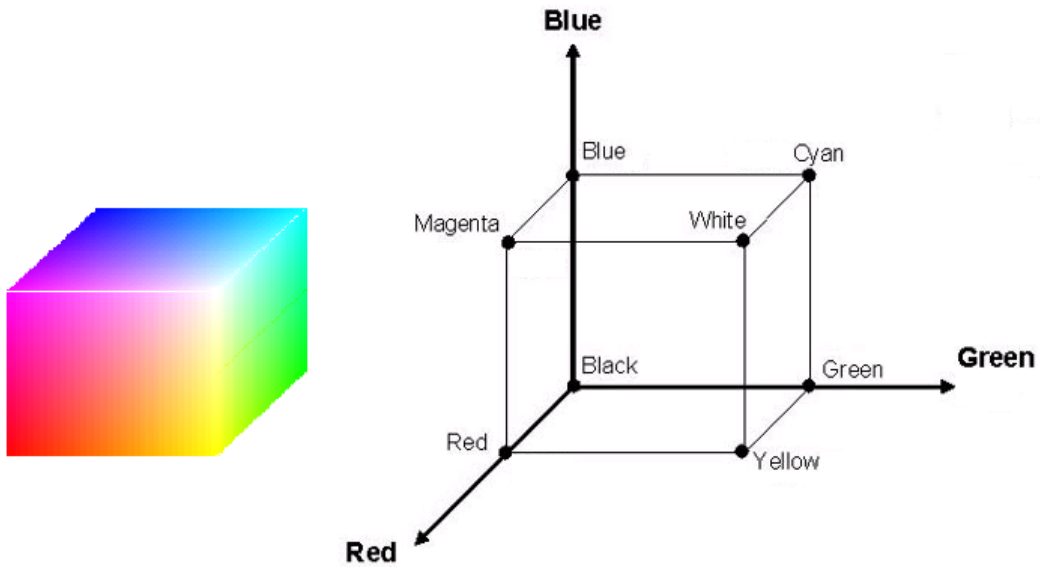
Fig. 2.6 RGB Color cube

2.2.2 XYZ Color Model

In order to modify the problem of negative input in RGB color space, CIE discovered a new color model such that the tristimulus values were not negative. XYZ color model is build based on direct measurements of human visual perception hence it is close to the human vision. Due to this characteristic, XYZ color space regard as the basis from which many other color spaces are defined. The tristimulus values in XYZ color model become X, Y and Z. These tristimulus values are transformed from R, G and B values. This transformation is given as equation 2.3.

$$\begin{bmatrix} X \\ Y \\ Z \end{bmatrix} = \begin{bmatrix} 0.4900 & 0.3100 & 0.2000 \\ 0.1770 & 0.8124 & 0.0106 \\ 0.0000 & 0.0100 & 0.9900 \end{bmatrix} \begin{bmatrix} R \\ G \\ B \end{bmatrix} \qquad (2.3)$$

The transformed color space is XYZ color space. According to this transformation, the tristimulus values would always be positive. Then equation 2.1 becomes

$$P(\lambda) = x(\lambda) \cdot X + y(\lambda) \cdot Y + z(\lambda) \cdot Z \qquad (2.4)$$

and the result of color matching function displays as below.

11
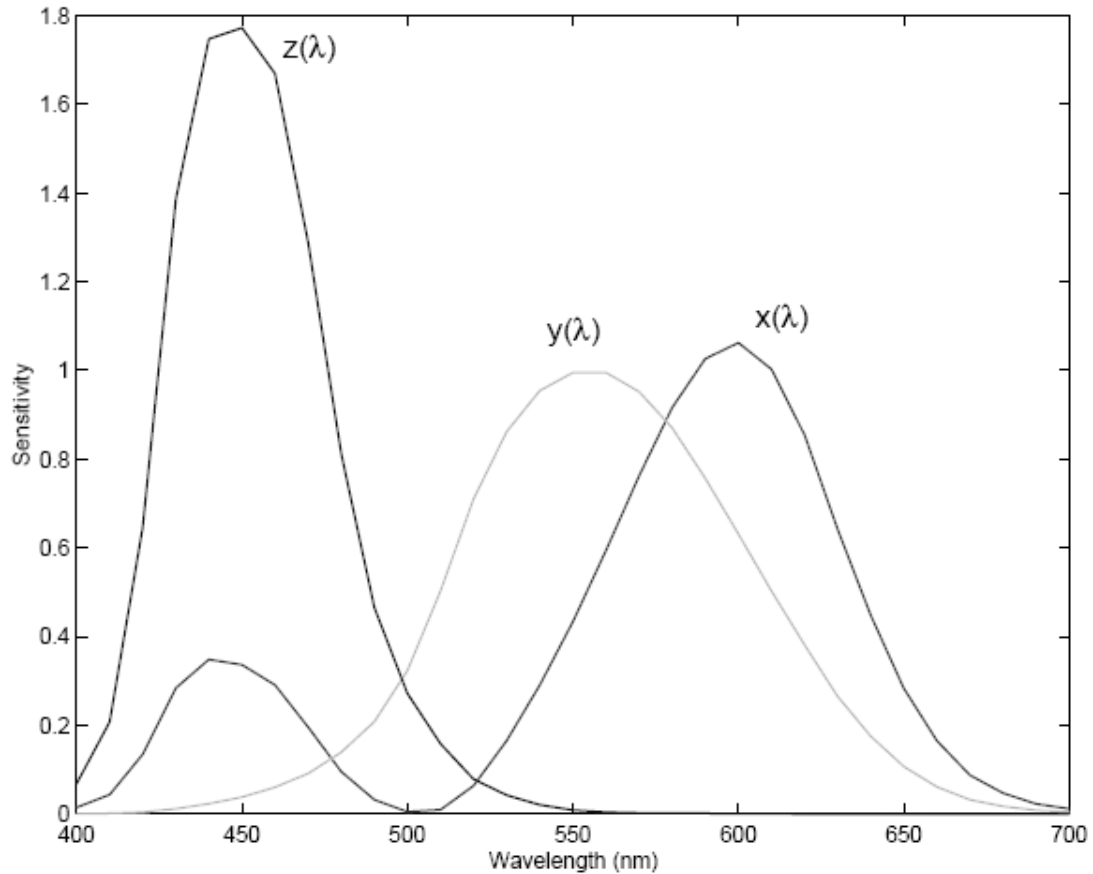
Fig. 2.7 The CIE 1931 XYZ color matching function

Another advantage of this color space is the component Y directly representing the luminance of a color.

Normalization of X, Y and Z sets three new stimulus x, y and z, as equation 2.5.

$$\begin{cases} x = \dfrac{X}{X+Y+Z} \\ y = \dfrac{Y}{X+Y+Z} \\ z = \dfrac{Z}{X+Y+Z} = 1 - x - y \end{cases} \qquad (2.5)$$

This produces the two dimensional chromaticity diagram xyY which is the projection of three dimensional XYZ color space. This chromaticity diagram allows some possible interpretations and is depicted as Fig. 2.8.
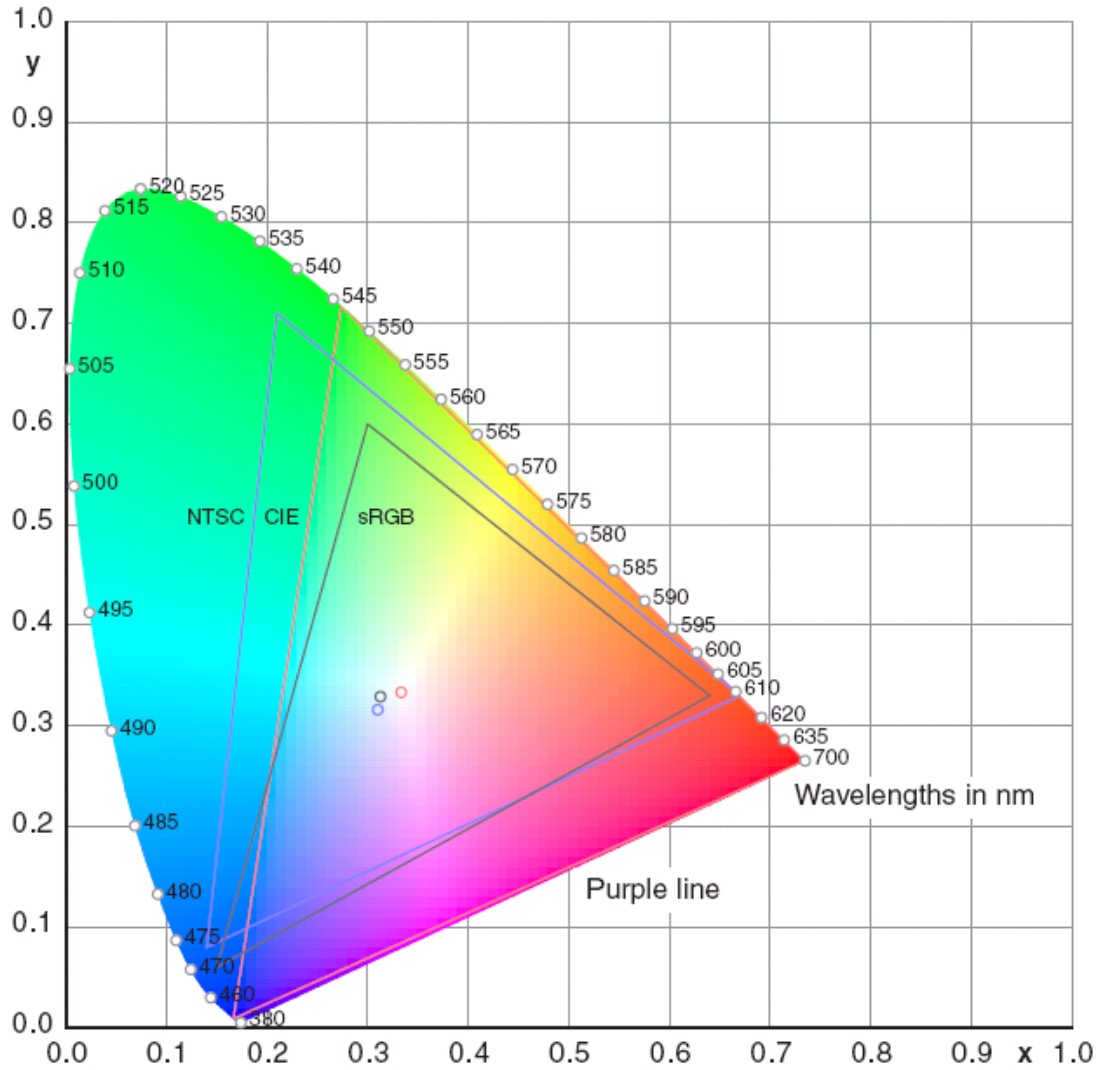
Fig. 2.8 The CIE 1931 color space chromaticity diagram xyY[3]

Note that x, y represent the chromaticity values while Y shows the luminance. Besides, mentioned that Fig. 2.8 also show other two color models. As discussed in section 2.2.1, different primaries is set defines different color models. Therefore, the transformation to XYZ color space should not be the same. These transformations of sRGB and NTSC are given by equation 2.6 and 2.7 respectively. Do not get confuse to equation 2.3. All of them are RGB color spaces. Equation 2.3 is CIE RGB color space. sRGB is a standard RGB color space proposed by Hewlett-Packard (HP) and Microsoft and is utilized on Internet, monitors and printers. NTSC is designed for analog television and has a larger gamut than most of today's monitors. Detailed introduction and mathematical process are given in [36]-[38].

---

[3] This figure refers to [38].

$$\begin{bmatrix} X \\ Y \\ Z \end{bmatrix} = \begin{bmatrix} 0.4125 & 0.3576 & 0.1804 \\ 0.2127 & 0.7152 & 0.0722 \\ 0.0193 & 0.1192 & 0.9502 \end{bmatrix} \begin{bmatrix} R \\ G \\ B \end{bmatrix} \qquad (2.6)$$

$$\begin{bmatrix} X \\ Y \\ Z \end{bmatrix} = \begin{bmatrix} 0.6067 & 0.1736 & 0.2001 \\ 0.2988 & 0.5868 & 0.1143 \\ 0.0000 & 0.0661 & 1.1149 \end{bmatrix} \begin{bmatrix} R \\ G \\ B \end{bmatrix} \qquad (2.7)$$

2.2.3 CIELab Color Model

When we try to compare two colors, use RGB or XYZ components is not precise. The reason is both of RGB and XYZ color space are not uniform color space. Non-uniform means when one color has the same Euclidean distance [see equation 2.8] between any two color points. These two colors maybe differ from each other or on the other hand they maybe recognize to be the same although these two colors have same ΔE_{RGB}.

$$\Delta E_{RGB} = \sqrt{(R_1 - R_2)^2 + (G_1 - G_2)^2 + (B_1 - B_2)^2} \qquad (2.8)$$

MacAdam had conducted an experiment on "similar" colors [30]. The same experimental platform displayed as Fig. 2.4 was conducted. Observer needed to match two color patterns in the view of field. The error in matching was recorded and yielded the sensitivity ellipses in the xyY chromaticity diagram as shown in Fig. 2.9. Those ellipses mean the differences in chromaticity are just noticeable regions. Within the ellipses, we may identify the colors are similar. Note that the ellipses are enlarged ten times in order to enhance its orientation.
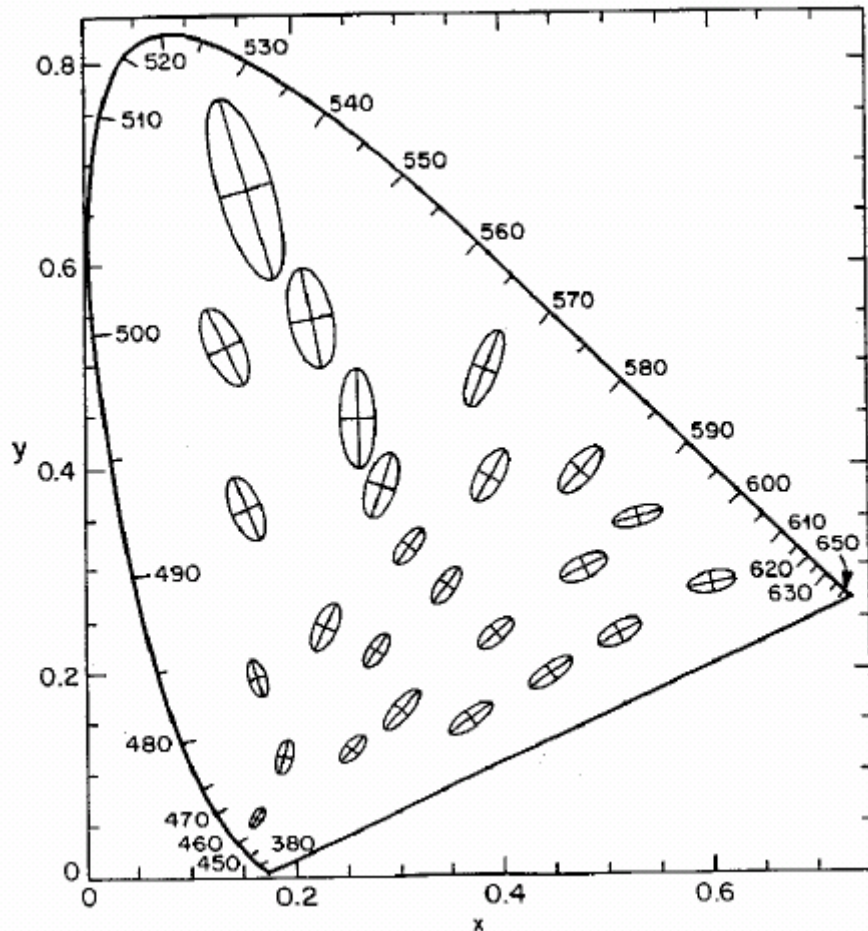
Fig. 2.9 MacAdam's ellipses (just noticeable regions) on the CIELuv diagram

As a result, if the color space is uniform, the same Euclidean distance of this color space can presents the same perception of human vision system sense to. CIE suggested two uniform color models in 1976, CIELuv and CIELab [24]. MacAdam's experiment was based on the CIELuv color model. Both color models are transformations of XYZ color model [see equation 2.9 and 2.10]. CIELuv reserves the characteristic that the mixture of any two colors would basically located at the line of the two sources but CIELab does not. However, we calculated the Euclidean distance, i.e., the color difference based on the CIELab color model as it is closer to the perception of human vision system. Fig. 2.10 shows the chromaticity diagram of CIELab color model.

$$L^* = \begin{cases} 116(\dfrac{Y}{Y_0})^{1/3} - 16 & for \ \dfrac{Y}{Y_0} > 0.008856 \\[4mm] 903.2963(\dfrac{Y}{Y_0}) & for \ \dfrac{Y}{Y_0} \le 0.008856 \end{cases}$$

$$u^* = 13L^*(u' - u_0)$$

$$v^* = 13L^*(v' - v_0) \tag{2.9}$$

$$where \begin{cases} u' = \dfrac{4X}{X + 15Y + 3Z} \\[4mm] v' = \dfrac{9Y}{X + 15Y + 3Z} \\[4mm] u_0, \ v_0 \ \text{are the coordinate of specific white point} \end{cases}$$

$$L^* = 116 \cdot f(\frac{Y}{Y_0}) - 16$$

$$a^* = 500[f(\frac{X}{X_0}) - f(\frac{Y}{Y_0})]$$

$$b^* = 200[f(\frac{Y}{Y_0}) - f(\frac{Z}{Z_0})]$$

$$where \ f(n) = \begin{cases} n^{1/3} & for \ n > 0.008856 \\ 903.2963n + 0.1379 & for \ n \le 0.008856 \end{cases} \tag{2.10}$$

$X_0, \ Y_0, \ Z_0$ are the XYZ tristimulus values of the reference white point
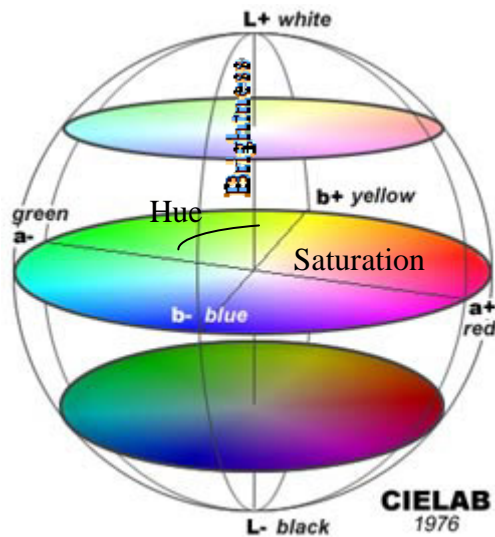
Fig. 2.10 The chromaticity diagram of CIELab color model

2.3 Performance Measurements

   As we carry out image processing, we may want to know how much does the result similar to the original image. That is to say, we want to know the performance of this process. Take image compression for example. There is a tradeoff between the compression ratio and image quality. The evaluation of quality may use mean square error (MSE). Such image measure can help the development and improvement of this process. MSE is just one kind of performance measurements indexes. In this dissertation, demosaicking has been discussed mostly. The images after demosaicking are usually compared to the raw image data. While various demosaicking algorithms have been proposed, we can effectively quantify the performance by these indexes. Note that the original one which compared with should be nonmosaicked image. The following introduced few measurements that we used in this thesis. We try to choose those indexes that can indicate the difference of two images from distinct aspects.

2.3.1 Peak Signal-to-noise Ratio (PSNR)

   Similar to mean square error (MSE), peak signal-to-noise ratio (PSNR) is the numerical difference between any two images. It is most commonly used as measure of quality of image processing. The PSNR in decibels (dB) is given by equation 2.11

$$PSNR = 10 \times \log_{10}(\frac{255^2}{MSE})$$

$$MSE = \frac{1}{M \times N} \sum_{n=1}^{M \times N} \|I(n) - P(n)\|^2 \qquad (2.11)$$

where $I(n)$ represent color value of nth pixel of the original image and $P(n)$ is the color value of the reconstructed image. Both of them have the size by $M \times N$.

   PSNR is defined on monochrome image. For color image with three RGB values per pixel, we can modify MSE to the sum over all squared differences values divided by image size and by three. Whereas, we keep PSNR to be derived from each color plane so that we can understand the individual performance of each plane. Normally, the PSNR value between 30 and 50 dB is considered as lossy image. The higher the PSNR value we receive, the better the image quality we get. When PSNR value is above 40 dB, it is hard to distinguish original image from reconstructed one by human eye. If the PSNR value is exceed 45 dB, that's mean the squared difference of each pixel between two images we compared is less than 1 in average.

2.3.2 Color Difference ($\triangle E_{ab}^{*}$)

As the discussion in section 2.2.3, we need to compare two colors under uniform color space in order to reveal the perception of human vision. Due to the same reason, the PSNR value is calculated in RGB color space which does not equate with human consciousness of color difference. Fig. 2.11 is an example of two images which have almost the same PSNR value of Y plane but the CIELab color differences ($\triangle E_{ab}^{*}$) are distinct from each other. We can observe the right image has some color misregistration around the fence region. Table 2.1 presents these indexes values.

Fig. 2.11 Two images with similar PSNR_Y but with different $\triangle E_{ab}^{*}$ value

Table 2.1 PSNR of Y plane and $\triangle E_{ab}^{*}$ values computed for the images in Fig. 2.11

	Left-hand image	Right-hand image
PSNR_Y	35.1198	35.8474
$\triangle E_{ab}^{*}$	0.9859	2.0270

The CIELab color difference ($\triangle E_{ab}^{*}$) measures the Euclidean distance between the

original image and the reconstructed one in CIELab color space [24][25]. It can better capture the color difference perceived by human observers. The $\triangle E_{ab}^{*}$ is given by the following equation where $L(n)$, $a(n)$ and $b(n)$ are the nth pixel of each plane of

$$\Delta E_{ab}^{*} = \frac{1}{M \times N} \sum_{n=1}^{M \times N} \sqrt{(L_1(n) - L_2(n))^2 + (a_1(n) - a_2(n))^2 + (b_1(n) - b_2(n))^2} \qquad (2.12)$$

CIELab color space in the original and reconstructed image.

A lower $\triangle E_{ab}^{*}$ value provides a better image quality. According to [25][30], $\triangle E_{ab}^{*} \approx 2.3$ correspond to an ellipse (just noticeable region) in Fig 2.9. The $\triangle E_{ab}^{*}$ greater than 2.3 indicates the color difference is visible. When the $\triangle E_{ab}^{*}$ is larger than 10, the reconstructed image is differ from the original one seriously.

2.3.3 Structural Similarity Index (SSIM)

Although MSE and PSNR are widely used for quality measurements, there are lots of evidences to show that these indexes are not matched to perceived human visual perception [40][41]. Fig. 2.11 is an obviously example. It is clearly that left-hand image has a better visual quality than right-hand one even if they have similar PSNR values. In order to modify these errors, a great deal of effort has used to develop the quality assessments that can estimate the quality in accordance with its visibility of human vision at the same time.

The structural similarity index (SSIM) proposed in [39] is able to quantify the visibility of errors between two images. The object of SSIM is to separate the influence of the illumination which may effect the comparison. Fig. 2.12 is the diagram of SSIM measurement.
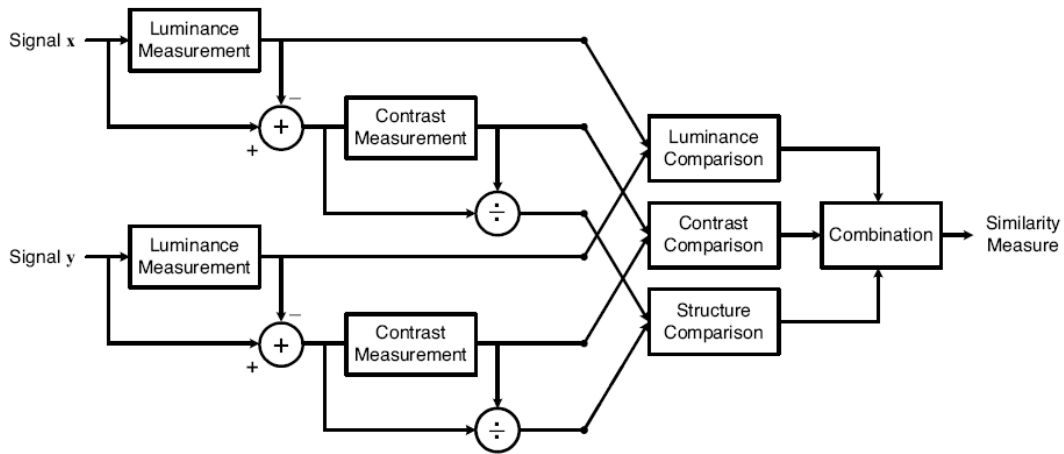
Fig. 2.12 The diagram of SSIM measurement[4]

This measurement mainly has three tasks: luminance, contrast and structure comparison, as depicted in Fig. 2.12. More introductions and computations in detail can refer to [39]. Also some downloads are available on [42]. Let's look some achievements of this index. The following two figures are refer to [42]. Fig. 2.13 best describe the function of SSIM. Almost of them have same MSE but SSIM can reflect the visual quality correspond to human perception of vision. Note that SSIM equal to 1 represents the same structural similarity of two images. Fig. 2.14 is another example of three images which have equivalent MSE. We can recognize the quality just by our eye.
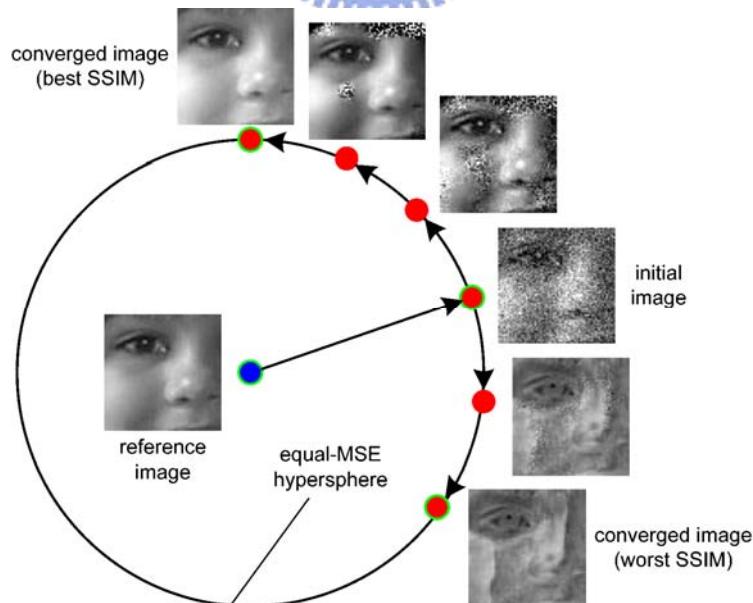
Fig. 2.13 Images with best / worse SSIM values lay on equal-MSE hypersphere

---

[4] This figure refers to [39]
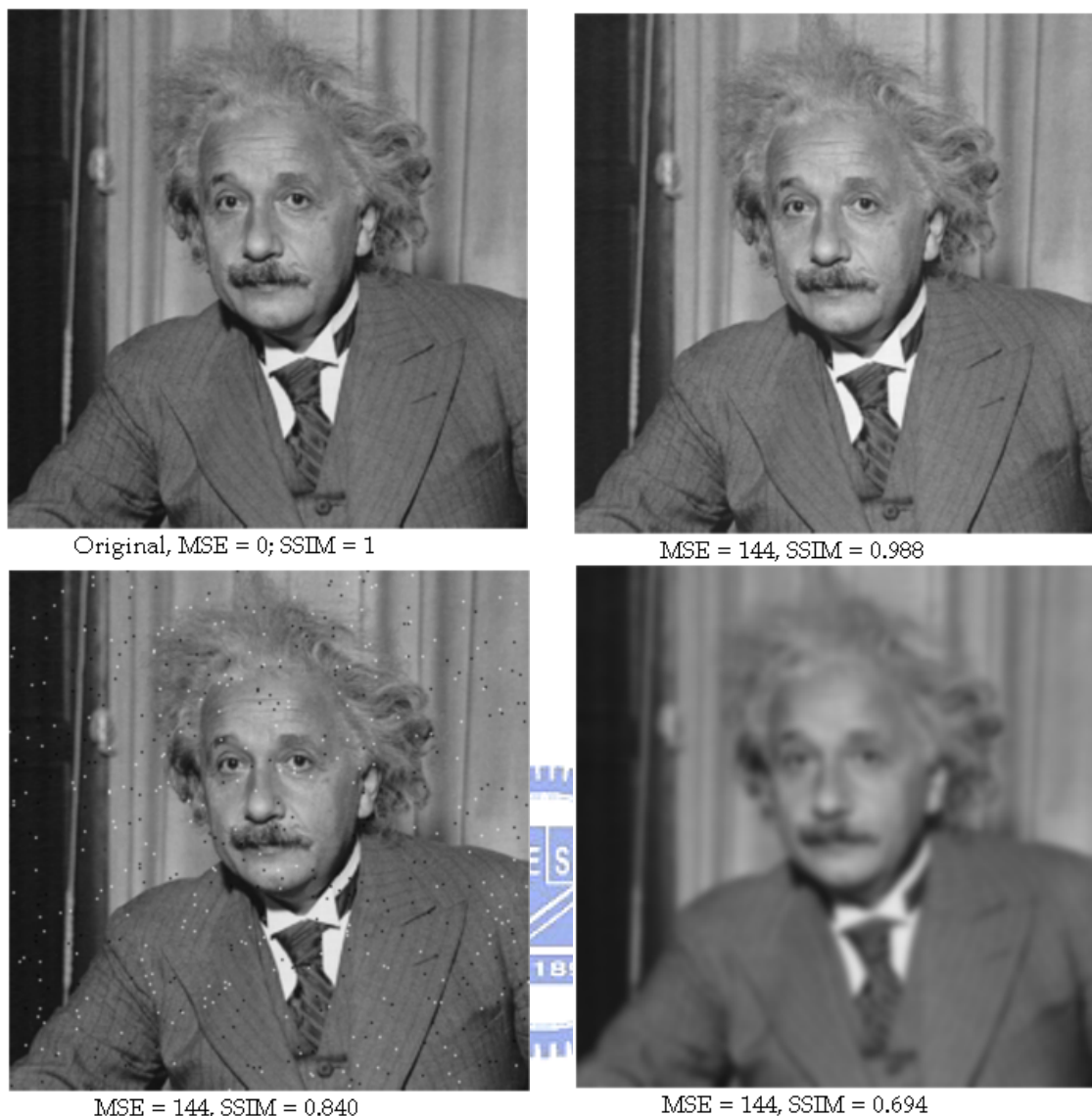
Fig. 2.14 SSIM evaluation of three images which have same MSE value

2.4 Common Demosaicking Methods for Bayer Pattern

As mentioned in section 1.1, most digital cameras use a single sensor array so that each pixel can capture only one sample of three color primaries. To obtain a full-color image, we need estimate the other two missing colors of each pixel. This process is known as demosaicking.

The simplest way of demosaicking is the spatial interpolation. The interpolation is been applied to each color plane separately, such as nearest-neighborhood replication, bilinear interpolation and cubic spline interpolation. Although those methods are easy to implement, the results may produce some aliasing and can not maintain edge information well. Various demosaicking algorithms have been discussed extensively in [2]-[22]. In this section, we will introduce some demosaicking methods and

discover their evolutions and improvements.

2.4.1 Ideal demosaicking

Demosaicking can be regard as the sample procedure of continuous signal. According to Whittaker-Shannon sampling theory, when the sampling frequency is not high enough (at least twice) compared to the maximum frequency of the continuous signal, there will be aliasing so that the original signal may not be reconstructed exactly. Fig. 2.15 illustrates this concept. Fig. 2.15(a) is the

(a.)

(b.)

(c.)

(d.)

Fig. 2.15 Example of sampling frequency higher / lower than twice of the maximum frequency

nonmosaicked raw image. When we run demosaicking on this image, the reconstructed one [see Fig. 2.15(b)] may produce aliasing because of violating the requirements by the sampling theorem. Nevertheless, the result of demosaicking on Fig. 2.15(c) shows no artifacts. The lowpass filter limits the Fourier spectrum of original image to half of the sampling frequency. Due to that, Fig. 2.15(d) is able to be reconstructed without aliasing.

The example above totally shows the sampling theory. In practice, however, real-world scenes do not have fixed frequency limit and we also not capable of changing that. To recover the original signal, a sinc function is used for the interpolation [43]. Unfortunately, this function is infinite and therefore is band-limited. Hence, this kind of interpolation is unable to implement practically.

2.4.2 Bilinear Interpolation

Bilinear interpolation is the simplest way of demosaicking. The interpolation is been applied to RGB color plane separately. Referring to Fig. 2.16, the missing G

Fig. 2.16 One sample of Bayer pattern

pixel of R_{44} is obtained by the average of G_{34}, G_{43}, G_{45} and G_{54}, as shown by equation 2.13. And the missing B of R_{44} is estimated also by the average of B_{33}, B_{35}, B_{53} and

$$G_{44} = \frac{G_{34} + G_{43} + G_{45} + G_{54}}{4}, \quad B_{44} = \frac{B_{33} + B_{35} + B_{53} + B_{55}}{4} \quad (2.13)$$

B_{55}. Likewise, R_{43} is the mean of R_{42} and R_{44}; B_{43} is the mean of B_{42} and B_{44}. Bilinear interpolation can be summarized by the following equation.

$$F_R = \frac{1}{4}\begin{bmatrix} 1 & 2 & 1 \\ 2 & 4 & 2 \\ 1 & 2 & 1 \end{bmatrix}, \; F_G = \frac{1}{4}\begin{bmatrix} 0 & 1 & 0 \\ 1 & 4 & 1 \\ 0 & 1 & 0 \end{bmatrix}, \; F_B = \frac{1}{4}\begin{bmatrix} 1 & 2 & 1 \\ 2 & 4 & 2 \\ 1 & 2 & 1 \end{bmatrix} \qquad (2.14)$$

While computing bilinear interpolation, convolution with F_R, F_G and F_B apply on R, G and B plane respectively. This type of interpolation is the process of lowpass filter and it can get acceptable results in low-frequency regions of an image. Whereas, it may produce some aliasing and blur the sharps edges in high-frequency regions. Fig. 2.17 is a demonstration of this phenomenon.

(a.)   (b.)
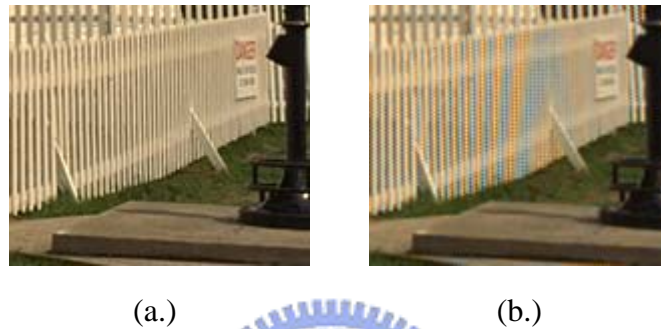
Fig. 2.17 Fence region of lighthouse (bilinear interpolation)

(a.) Original image (b.) Reconstructed image

2.4.3 Inter-channel Correlation Interpolation

To get better results, some demosaicking methods utilize the inter-channel correlation. In [4] ,Cok presents an observation that the ratios between R and G values are strongly similar in a local region of an image. So are the ratios between B and G values. Based on this concept, some algorithms have been developed [3]-[5] and interpolation would take other two color planes into account instead of interpolation itself. Besides color ratios, many methods also make use of inter-channel color differences (R-G or B-G) [4]-[9]. The conventional interpolation method proposed by [6] exploits the inter-channel color differences correlation sufficiently. When interpolating the missing color, the existed color can assist to upgrade the estimation at same pixel. The interpolation way is given by equation 2.15.

$$G - G_{lpf} = X - X_{lpf}, \; X = R \; or \; B$$
$$\Rightarrow G = G_{lpf} + \Delta X \qquad\qquad (2.15)$$

ΔX can help to upgrade the estimation value G_{lpf}. While interpolate R and B

plane, we just modify equation 2.15 to $X = X_{lpf} + \Delta G$. Referring to Fig. 2.16, G_{44} is estimated by the following equation.

$$
\begin{aligned}
G_{44} &= G_{lpf} + \Delta R \\
&= \frac{G_{34} + G_{43} + G_{45} + G_{54}}{4} + (R_{44} - \frac{R_{24} + R_{42} + 4R_{44} + R_{46} + R_{64}}{8})
\end{aligned}
\tag{2.16}
$$

Although exploiting the inter-channel correlation can come to a better result than bilinear interpolation. These methods, however, still have poor performance around sharp edges and fine details. The reason is the observation mentioned initially does not hold whenever the image has high-frequency regions.

2.4.4 Edge-directed Interpolation (Gradient and Laplacian based)

Since some artifacts may generate around the edges, several algorithm are based on the edge-interpolation [11]-[14]. Some algorithms analyze the spatial structure of a local region in an image by gradients [11] or the laplacian [12], [13], and then choose the best directions to do interpolation. Referring to Fig. 2.16, the concepts of edge-directed interpolation can be described by the equation below.

$$
\begin{cases}
D_H = \left| -R_{42} + 2R_{44} - R_{46} \right| + \left| G_{43} - G_{45} \right| \\
D_V = \left| -R_{24} + 2R_{44} - R_{64} \right| + \left| G_{34} - G_{54} \right|
\end{cases}
\tag{2.17}
$$

$$
G_{44} =
\begin{cases}
\dfrac{G_{43} + G_{45}}{2} + \dfrac{-R_{42} + 2R_{44} - R_{46}}{4} & \text{, for } D_H < D_V \\[2ex]
\dfrac{G_{34} + G_{54}}{2} + \dfrac{-R_{24} + 2R_{44} - R_{64}}{4} & \text{, for } D_H > D_V \\[2ex]
\dfrac{G_{34} + G_{43} + G_{45} + G_{54}}{4} + \dfrac{-R_{24} - R_{42} + 4R_{44} - R_{46} - R_{64}}{8} & \text{, otherwise}
\end{cases}
\tag{2.18}
$$

D_H and D_V is the classifiers and is composed of the laplacian for chroma data (R plane in this example) as well as gradient for G plane. According to these classifiers, we can realize the distribution along horizontal and vertical directions in this pixel. If the computation of this classifier is large, this direction may contain high-frequency components. Thus, we do interpolation along another direction.

2.4.5 Weights Based Interpolation

Since the observation in section 2.4.3 is necessary hold in smooth region, we can choose the direction which has few edges information and executes interpolation based on the observation. Just like the technique used in the last section, we can have a better result than using the observation only.

The algorithm proposed in [10][16] extends the above concepts. These methods compute an estimation value and a weight along each known direction. In [10], the estimation is calculated according to the assumptions below. Note that the symbol '~' ahead denote the missing color values that we want to estimate and the pixel arrangement can refer to Fig. 2.16.

$$\begin{cases} \widetilde{G}_{44} - \widetilde{G}_{24} = R_{44} - R_{24} \\ \widetilde{G}_{44} - G_{34} = G_{34} - \widetilde{G}_{24} \end{cases} \qquad (2.19)$$

Combining these two assumptions, we can get the equation (2.20).

$$R_{44} - R_{24} = \widetilde{G}_{44} - \widetilde{G}_{24} = (\widetilde{G}_{44} - G_{34}) + (G_{34} - \widetilde{G}_{24}) = 2(\widetilde{G}_{44} - G_{34})$$
$$\Rightarrow \widetilde{G}_{44} = G_{34} + \frac{R_{44} - R_{24}}{2} \qquad (2.20)$$

Therefore, G_{44} value can be estimated by equation 2.20 from the top interpolation direction.

And the weight is calculated from the gradient of the same direction, given by equation 2.21.

$$\left| \frac{G_{43} - G_{23}}{2} \right| + \left| R_{44} - R_{24} \right| + \left| \frac{G_{45} - G_{25}}{2} \right| + \left| G_{54} - G_{34} \right| + \left| G_{34} - G_{14} \right| \quad (2.21)$$

Equation 2.21 can reveal the sharpness in the specific direction. If this direction contains high-frequency ingredients, the weight should be small to reveal the assumptions in equation 2.19 are not fit to hold. So the weight along top direction is designed as following.

$$\alpha_{34} = \frac{1}{1 + \left| \frac{G_{43} - G_{23}}{2} \right| + \left| R_{44} - R_{24} \right| + \left| \frac{G_{45} - G_{25}}{2} \right| + \left| G_{54} - G_{34} \right| + \left| G_{34} - G_{14} \right|} \qquad (2.22)$$

Referring to Fig. 2.16, to properly combine the estimated value correspond to the assumptions in equation 2.19, G_{44} value can be interpolated by equation 2.23.

$$\widetilde{G}_{44} = \frac{\alpha_{34}\widehat{G}_{34} + \alpha_{43}\widehat{G}_{43} + \alpha_{45}\widehat{G}_{45} + \alpha_{54}\widehat{G}_{54}}{\alpha_{34} + \alpha_{43} + \alpha_{45} + \alpha_{54}}$$

$where \quad \widehat{G}_{34} = G_{34} + \dfrac{R_{44} - R_{24}}{2} \qquad \widehat{G}_{43} = G_{43} + \dfrac{R_{44} - R_{42}}{2}$ \qquad (2.23)

$\qquad \widehat{G}_{45} = G_{45} + \dfrac{R_{44} - R_{46}}{2} \qquad \widehat{G}_{54} = G_{54} + \dfrac{R_{44} - R_{64}}{2}$

$\qquad \alpha$ is calculated in similar way of equation 2.22

2.4.6 Homogeneity Based Interpolation

In [22], it uses another indicator instead of gradient or laplacian. This method utilizes the local homogeneity as an indicator. It has two estimated candidates along horizontal and vertical direction and then interpolates in the direction with fewer color artifacts according to the homogeneity. The homogeneity, measured in the CIELab color space, is the total number of similar luminance (L) and chrominance (a,b) values within a neighborhood of a pixel. This neighborhood is defined by the specific threshold of Euclidean distance in L and a, b channels, described as Fig. 2.18.
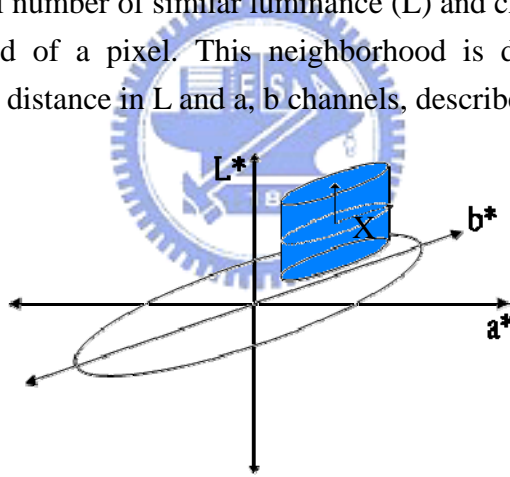
Fig. 2.18 Neighborhood's range of a pixel X in CIELab color space

While located within this blue cylindrical area in the CIELab color space, this point is regard as a neighbor and the Euclidean distance is recorded. That is, the more neighbors meet the conditions, the larger the homogeneity value is.

So this algorithm first interpolate along vertical and horizontal direction separately. The two reconstructed results are then transformed to CIELab color space and calculate their homogeneity. Finally, we combine these results to one image according to the direction with large homogeneity value.

CIELab is a uniform color space. As our discussion in section 2.2.3, this color space presents the same perception of human vision system sense to. Due to that,

homogeneity based interpolation can achieve significant result around edges. Fig. 2.19 displays its performance.

Fig. 2.19 Fence region of lighthouse (homogeneity based interpolation)

(a.) Original image (b.) Reconstructed image

2.4.7 Other Interpolation Methods

By taking the advantages of some methods of demosaicking mentioned above, hybrid demosaicking algorithms may appear and could reduce some artifacts more efficiently. In [3], Kimmel uses an edge-interpolation and then enhance the image by an inverse diffusion process. In [14], Li and Orchard interpolate based on the geometric duality between the low-resolution covariance and the high-resolution covariance. There are also more complicated demosaicking methods. In [17]-[19], these methods proposed a minimum mean-square error (MMSE) solution and also produce satisfactory results no matter in visually and in demosaicking performance measurements. In [9], it takes the directional information and judge the correlation in a local region. In [21], it proposed a different view of demosaicking in temporal domain. Interpolation can have the help of the intra-frame and inter-frame information by the motion estimation. However, in this dissertation, we pay our attention mostly on iterative demosaicking.

Chapter 3   *Demosaicking using Iterative Approach*

3.1 Introduction

Several demosaicking methods have been proposed for the last few decades, all of them are aim to suppress the aliasing and visible artifacts. Iteration is also employed in some algorithms. From some literature, several methods tend to use two-steps way to suppress the artifacts after initial interpolation. Gunturk in [15] exploits the detail and observation projection and repeats doing the projection after the edge-directed interpolation; Kimmel in [3] uses the second stage to enhance the result from the first stage; Li in [20] proposed an iterative method in the color difference domain. Though the computation of these algorithms may be complicated, these methods are effective in suppressing color misregistration and zipper effects in the demosaicked images. The rest of this chapter will introduce some iterative demosaicking methods. Then a discussion about the problem of iteration is taken on. In order to solve this problem and suppress artifacts effectively at the same time, we present a hybrid iterative demosaicking algorithm. Some comparisons are also made by the performance measurements mentioned in section 2.3 and display some test images derived from different demosaicking methods.

3.2 Projections onto Convex Sets (POCS)

Projection onto Convex Sets (POCS) in [15], proposed by Gunturk, is a landmark using iterative approach in this field for the last few years. This method makes two observations:

1) High-frequency subbands of R / B and G plane are highly correlated.
2) Low-frequency subbands of original and interpolated image are highly correlated.

These subbands are decomposed by discrete wavelet transform (DWT), as shown in Fig. 3.1, Low-frequency subbands means the top-left band (LL) and the rest are
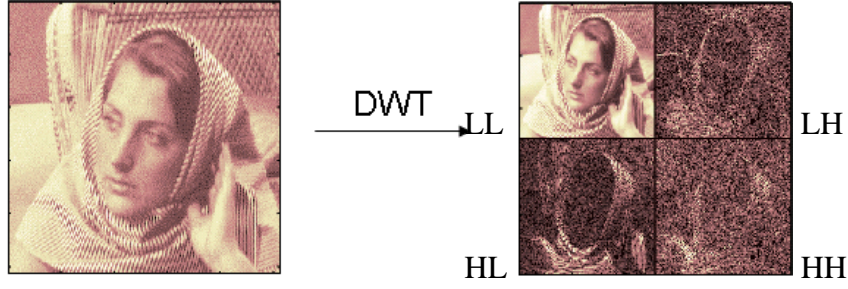
Fig. 3.1 Decomposition into four subbands by DWT

high-frequency subbands (LH, HL and HH). Highly correlated represents the correlation coefficient given by equation 3.1 is larger than 0.9.

$$C_{x,y} = \frac{\sum_{(i,j)}(x(i,j)-\mu_x)(y(i,j)-\mu_y)}{\sqrt{\sum_{(i,j)}(x(i,j)-\mu_x)^2}\sqrt{\sum_{(i,j)}(y(i,j)-\mu_y)^2}} \qquad (3.1)$$

In equation (3.1), (i,j) are the spatial coordinates in integers, $x(i,j)$ and $y(i,j)$ are two different color planes or subbands and μ_x and μ_y are the means of $x(i,j)$ and $y(i,j)$, respectively.

POCS also define two constraint sets: Detail and observation constraint set. Detail constraint set is the absolute difference between the detail subbands (high-frequency subbands) of R / B and G plane is constrained to be less than a threshold. Observation constraint set means the interpolated pixels are consistent to the observed data that CFA sampled. These two constraint sets have been proved to be convex.

This algorithm firstly makes interpolation to RGB plane. The interpolation way can be bilinear interpolation or edge-directed interpolation mentioned in section 2.4.4. Then the initial estimates execute the detail and observation projection iteratively. The detail projection is updating the detail subbands of R and B plane where the pixel is within the detail constraint set to the same location of G plane. The observation projection is inserting the observed data into their corresponding locations.

3.3 Demosaicking with Post-processing

Post-processing, the procedure of improvement, can upgrade the initial estimation further. The detail and observation projection in POCS is an example of this process. The purpose of the post-processing is designed to suppress the visible artifacts we obtained from the first stage. Some artifacts such as false color and zipper effect are

commonly seen in the demosaicking images. The reasons why these artifacts generated have been discussed extensively in [8], [10], [22]. And they also present some methods to reduce them. Fig. 3.2 shows some examples of these artifacts.

(a.)
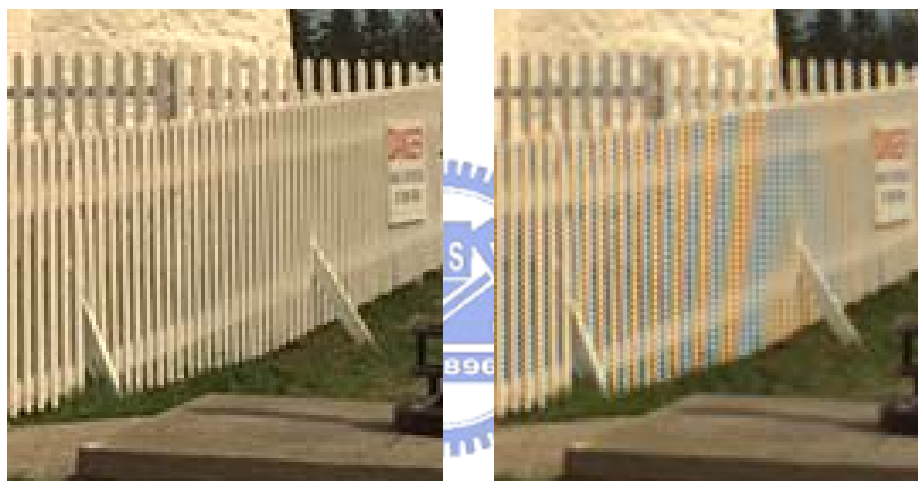
(b.)

Fig. 3.2 The example of (a.) false color and (b.) zipper effect

Fig. 3.2(a) shows the false color around the mast and Fig. 3.2(b.) shows the zipper effect on the fence region. The left hand is the original image and the right hand is the demosaicked image.

Lu and Tan in [10] directly named 'Post-processing' of their second step. Let make a briefly review of this step. The post-processing in [10] exploits the spatial correlation for reduce the artifacts. This spatial correlation is the inter-channel differences (R / B and G) changing smoothly. The outliers of a local region may be considered as aliasing or color artifacts. In order to use the relationship more effective, it adopts the median filtering as it can effectively diffuse the estimation errors into local neighborhoods. The size of median filter is 5 by 5. It adjusts the central pixel by the local region $\Re$ around it covering 5×5 pixels. Following is the adjustment:

$$G_{adjust} = \frac{(R_{oriental} - median(R_{x,y} - G_{x,y})) + (B_{oriental} - median(B_{x,y} - G_{x,y}))}{2}$$

$$R_{adjust} = G_{adjust} + median(R_{x,y} - G_{x,y}) \tag{3.2}$$

$$B_{adjust} = G_{adjust} + median(B_{x,y} - G_{x,y})$$

where $(x, y) \in \Re$, R_{adjust}, G_{adjust} and B_{adjust} are the values after modified.

Furthermore, to avoid the degeneration of the observed data, it adaptive use the median filter only on the artifact-prone regions. Fig.3.3 is an example of these regions. Using the Laplacian operator (on G plane only) to detect the edges and then set a threshold to define the edge map, given by equation 3.3.

$$f(i, j) = \frac{1}{11} \begin{bmatrix} 1 & 9 & 1 \\ 9 & -40 & 9 \\ 1 & 9 & 1 \end{bmatrix} * G(i, j)$$

$$M(i, j) = \begin{cases} 1, & for \ |f(i, j)| > 15 \\ 0, & otherwise \end{cases} \tag{3.3}$$

The median filter will only apply to those pixels which are in the edge map. Details of the method are discussed thoroughly in [10].
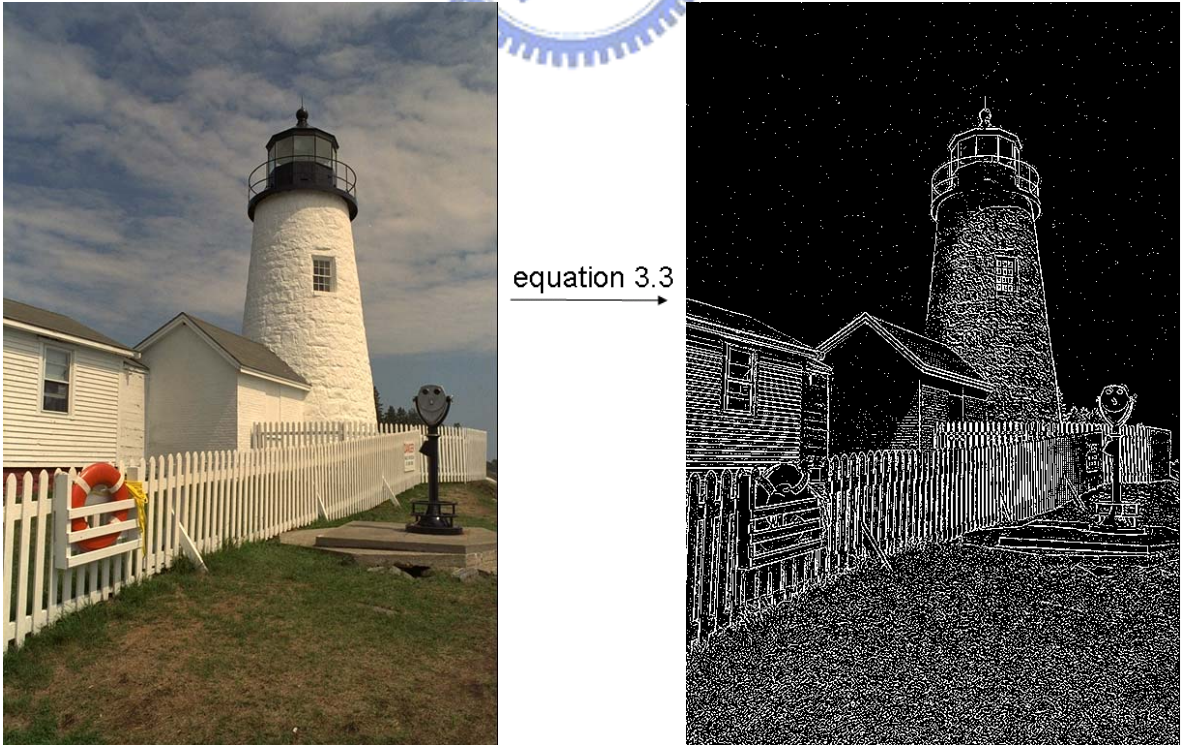
Fig. 3.3 The artifact-prone regions (white points) where post-processing apply on

3.4 Bottleneck of Iterative Approach

Among several ways, recursive methods can achieve a better result [2]. The iteration had been widely used in demosaicking since the closed-loop estimation can approximate the original color values and hence enable to reduce these artifacts. Li in [20] gives a discussion about the iteration strategy and brings up three important questions about the iteration mentioned as following:

1) When to start the iteration?
2) Does the iteration converge?
3) If the iteration is converge, when should we stop the iteration?

The convergence of the iteration had been proved in the literature [15]. The theory of projection-onto-convex-set (POCS) presented in the literature will be used in our proposed post-processing. However, despite the convergence property of iterative demosaicking method, the ultimate solution, i.e., the limit of the convergence process, is not the optimal solution. We can understand this argument visually in Fig. 3.4. The
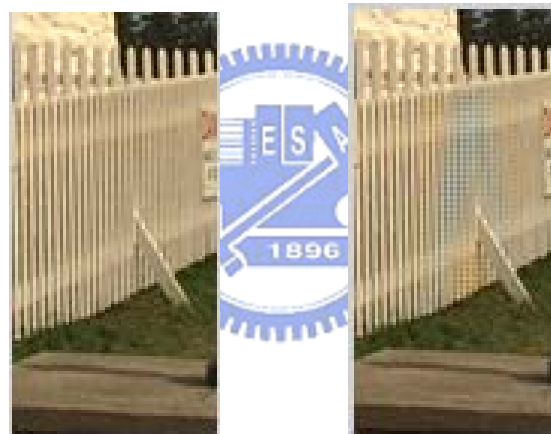
Fig. 3.4 The zipper effect may be generated of the ultimate solution.
(Left) The original image. (Right) The reconstructed image by 10 iterations.

artifact shown in Fig. 3.4 is the zipper effect. Compared to the zipper effect we mentioned in Fig. 3.3, the artifact in Fig. 3.4 seems to be light but still some "on-off" patterns could be seen. This kind of zipper effect is due to too many iterations executed when demosaicking.

Besides, each post-processing is based on different assumptions. If the assumptions are fail to hold during iteration, image quality would be worse and worse. Therefore, we should understand which situation may cause failure and try to optimize. From the above discussion, in order to minimize the risk of having these artifacts both in visually and in performance measurements, setting a stop criterion to stop iteration appropriate is necessary. The discussion of the stop criterion is presented in the next

section.

3.5 Proposed Recursive Demosaicking Algorithm

This chapter mainly discusses the algorithm we proposed. We present a hybrid iterative demosaicking algorithm which contains the interpolation step and the post-processing step. The first stage is interpolating the missing color values. The G plane is first to be fully reconstructed, and then adaptively using the detail subbands of R and B to upgrade the G plane value. Next the G plane is used to help the R and B plane interpolation. The interpolation manner could be bilinear, edge-directed interpolation…etc. In our algorithm, we use the homogeneity based interpolation in [22] and the weighted sum method in [10] since both of them provide good performance.

The second stage is post-processing step which is designed to suppress the artifacts we obtained from the first stage. We combine the post-processing in [10] with the observation projection in [15]. This extension then become iterative and can reduce the demosaicking artifacts more effective. Besides, we also consider the detail and observation projection in [15]. Arrange these two ways of post-processing with iteration ingeniously can provide satisfactory results in suppressing those artifacts. However, too many iterations may cause some aliasing according to the discussion in the last. Setting a stop criterion seems to be necessary. In our proposed algorithm, we will judge the image property by its spatial correlation coefficients first before the second stage. If the post-processing is not work on this image, the input image won't be entered to the second stage. If the post-processing is worthy to do for this image, we adaptively run the iteration according to its spatial correlation coefficients.

3.5.1 Stage 1: Interpolation Step

In this section, we describe the first stage of our proposed demosaicking algorithm. Fig. 3.5 depicts the flowchart of this interpolation step. The G plane is first to be fully
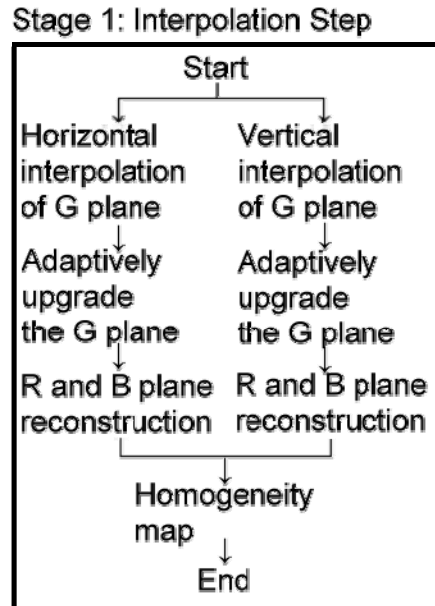
Fig. 3.5 Flowchart of the Stage 1: Interpolation step

reconstructed, and then used to help the R and B plane interpolation. Make this kind of interpolation order is the most popular way in the current demosaicking methods since it utilizes the inter-channel correlation and is surely have better results than bilinear interpolation. Demosaicking to each color plane can get the aid and the information of other two planes instead of interpolate separately.
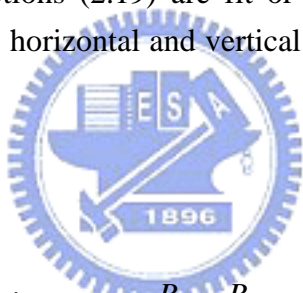
Besides, the homogeneity based interpolation in [22] can achieve significant results to those artifacts-prone regions. We exploit the homogeneity map in our algorithm. Hence, we first make interpolation along horizontal and vertical direction on G plane. Since the R and B plane interpolation can be helped by G plane, the better the G been reconstructed, the more reliable the G plane information that R and B plane can refer to. In order to make the G plane interpolated precisely, we exploit the detail subbands of R and B to upgrade the G plane value [15]. Next the G plane is used to assist the R and B plane interpolation. After that, calculate the homogeneity map of the results along different direction. According to this map, we are able to choose the direction with fewer color artifacts.

A. G Plane Interpolation along horizontal and vertical direction

Fig. 3.6 One sample of Bayer pattern

For the reason of convenience, we move Fig. 2.16 to here. The interpolation we used is the weighted sum method in [10]. Proper weights of the two estimated G values can reveal the assumptions (2.19) are fit or not. Referring to Fig. 3.6, the estimation values of G_{44} along horizontal and vertical direction are given by equation 3.4 and 3.5, respectively.

$$G_{44H} = \frac{\alpha_{43}\hat{G}_{43} + \alpha_{45}\hat{G}_{45}}{\alpha_{43} + \alpha_{45}}$$

$$where \quad \hat{G}_{43} = G_{43} + \frac{R_{44} - R_{42}}{2} \quad \hat{G}_{45} = G_{45} + \frac{R_{44} - R_{46}}{2}$$

$$\alpha_{43} = \frac{1}{1 + \left|\dfrac{G_{34} - G_{32}}{2}\right| + \left|R_{44} - R_{42}\right| + \left|\dfrac{G_{54} - G_{52}}{2}\right| + \left|G_{45} - G_{43}\right| + \left|G_{43} - G_{41}\right|} \quad (3.4)$$

$$\alpha_{45} = \frac{1}{1 + \left|\dfrac{G_{34} - G_{36}}{2}\right| + \left|R_{44} - R_{46}\right| + \left|\dfrac{G_{54} - G_{56}}{2}\right| + \left|G_{43} - G_{45}\right| + \left|G_{45} - G_{47}\right|}$$

$$G_{44V} = \frac{\alpha_{34}\hat{G}_{34} + \alpha_{54}\hat{G}_{54}}{\alpha_{34} + \alpha_{54}}$$

$$where \quad \widehat{G}_{34} = G_{34} + \frac{R_{44} - R_{24}}{2} \quad \widehat{G}_{54} = G_{54} + \frac{R_{44} - R_{64}}{2}$$

$$\alpha_{34} = \frac{1}{1 + \left|\frac{G_{43} - G_{23}}{2}\right| + \left|R_{44} - R_{24}\right| + \left|\frac{G_{45} - G_{25}}{2}\right| + \left|G_{54} - G_{34}\right| + \left|G_{34} - G_{14}\right|} \quad (3.5)$$

$$\alpha_{54} = \frac{1}{1 + \left|\frac{G_{43} - G_{63}}{2}\right| + \left|R_{44} - R_{64}\right| + \left|\frac{G_{45} - G_{65}}{2}\right| + \left|G_{34} - G_{54}\right| + \left|G_{54} - G_{74}\right|}$$

Once the G plane is fully reconstructed, it can be used to help the R and B plane interpolation. Before that, we upgrade the G plane value in order to give more precise information for the next interpolation.

B. Adaptively Upgrade the G Plane

In this section, we describe the method to upgrade the G plane. Gunturk in [15] has proposed a skill which replaces the detail subbands of G plane with R and B plane to upgrade the G plane. Nevertheless, this skill is work only under an assumption. The assumption said the inter detail subbands correlation coefficients calculated by equation 3.1 should be larger than 0.9 for R / B plane and G plane. However, some images are failed to satisfy this assumption. We discussed this problem by some examples presented in Table 3.1. We can observe the first test image

Table 3.1 Some example of upgrade the G plane after we finish interpolating G

Image No.	R / G Corr. Coef.				B / G Corr. Coef.				Upgrade the G plane	
	LL	LH	HL	HH	LL	LH	HL	HH	No	Yes
Fig. 3.25 #1	0.8460	0.9931	0.9805	0.9947	0.9914	0.9964	0.9926	0.9941	11.0093	5.7580
Fig. 3.25 #4	0.5905	0.8981	0.8877	0.9597	0.9560	0.9905	0.9874	0.9829	3.7255	7.0679
Performance measurement for G plane in terms of mean square error (MSE)										

has a strong correlation of it's detail subbands (LH, HL, HH) either in R / G or in B / G. Undoubtedly, upgrade the G plane can improve it's quality in the measurement of MSE. But the second test image dose not have the improvement as the first one and tends to be worse in the performance. Therefore, we need to set a judgment to classify the image we interpolated. In our proposed algorithm, we exploit the inter-channel correlation coefficients calculated also by equation 3.1. The x and y in equation 3.1 then change to one of three primary color plane instead of detail subbands. The

correlation coefficients of R / G, B / G and R / B could be computed, but we use R / G and B / G as the upgrade employs these two correlations only. Statistically, we find the lower the R / G or B / G correlation coefficient is, the more the chance that the detail subbands correlation are not strong. None the less, this observation is hold to the raw images. Does it also hold while demosaicking? In our experiments, we find the conventional interpolation method described in section 2.4.3 can give the approximations of inter-channel correlation coefficients, in other words, the real coefficients are similar to the values we got from the conventional interpolation. Table 3.2 describes this observation as follow.

Table 3.2 The inter-channel correlation coefficients between real value and the approximate

Image No.	Fig. 3.25 #2			Fig. 3.25 #3			Fig. 3.25 #4		
	R / G	B / G	R / B	R / G	B / G	R / B	R / G	B / G	R / B
The Real Value	0.5279	0.9740	0.4063	0.7185	0.5534	0.2890	0.6004	0.9568	0.6850
The Approximate	0.5332	0.9720	0.4245	0.7167	0.5579	0.2863	0.6051	0.9551	0.6879
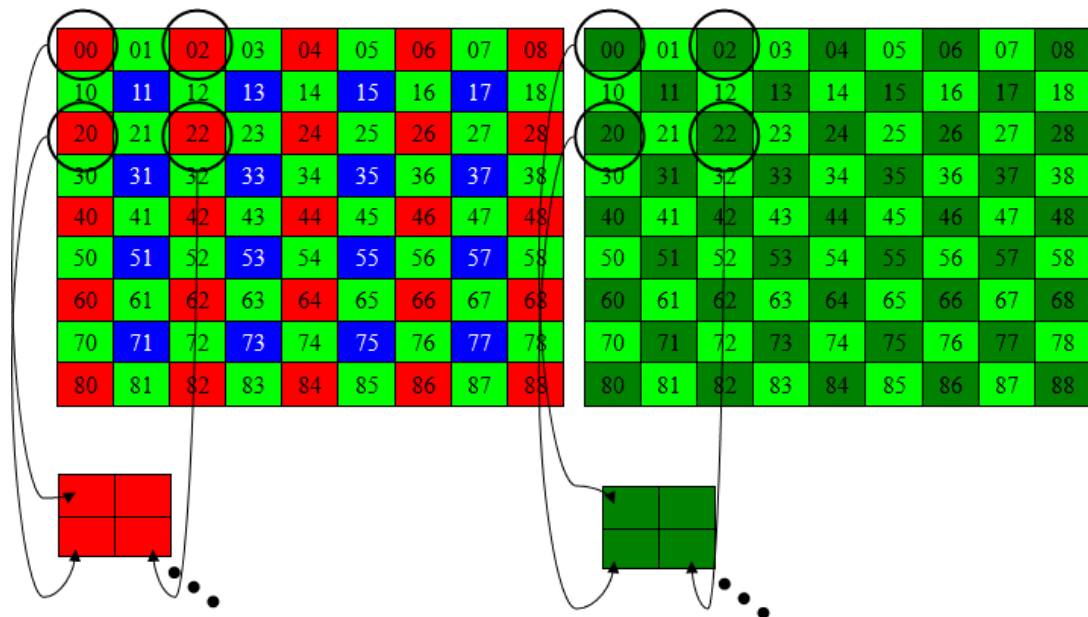
Fig. 3.7 Downsample vision of observed R and estimated G

Since we can get the approximation mentioned above, we use it to classify the images as the steps below

1) Use the observed samples of R and downsample it. Note that all pixels of this downsampled version are observed data, i.e. the known pixel value from CFA [see Fig. 3.7].

2) Use the interpolated G plane at the corresponding R locations and downsample it. Note that all pixels of this downsampled version are from

38

the results of G interpolation [see Fig. 3.7].

3) Decompose the downsampled version from above two steps into four subbands (LL, LH, HL, HH).

4) Adaptively choose the image that is suitable for upgrade the G plane according to the approximate in Table 3.2. If the image is fit, replace the detail subbands (LH, HL, HH) of the G plane with R. If not, maintain the detail subbands.

5) Reconstructed the downsampled G plane and then insert all pixels to the place they located initially.

6) Repeat the step above for the observed samples of B.

After the G plane is been upgraded along horizontal and vertical direction, we can use the more accurate G plane to assist R and B plane interpolation, as detailed in the following section.

C. R and B Plane Interpolation

Since the G plane is fully populated, the R and B planes can have the aid of the G plane no matter the observed samples or the interpolated ones. This step is achieved as follow: interpolate the missing R values at observed B and vice versa, and then fill the rest of the missing R and B values at observed G. Reconstructed G planes along horizontal and vertical direction are been used in the same manner.

Fig. 3.8 Reconstructed G plane and observed R, B plane

Referring to Fig. 3.8, the dark green area means the estimation value of G plane. The missing B_{44} is interpolated as equation 3.6 and 3.7. The missing R located at observed B is interpolating at the same way. It may confuse about the little difference of equation 3.6 and 2.23. Observed that equation 2.23 is refer to the pixel two spatial space away and equation 3.6 is just one spatial space may understand the difference between them.

$$\widetilde{B}_{44} = \frac{\alpha_{33}\widehat{B}_{33} + \alpha_{35}\widehat{B}_{35} + \alpha_{53}\widehat{B}_{53} + \alpha_{55}\widehat{B}_{55}}{\alpha_{33} + \alpha_{35} + \alpha_{53} + \alpha_{55}}$$

$$where \quad \widehat{B}_{33} = B_{33} + (G_{44} - G_{33}) \qquad \widehat{B}_{35} = B_{35} + (G_{44} - G_{35}) \qquad (3.6)$$

$$\widehat{B}_{53} = B_{53} + (G_{44} - G_{53}) \qquad \widehat{B}_{55} = B_{55} + (G_{44} - G_{55})$$

$$\alpha_{33} = \frac{1}{1 + \left|\dfrac{G_{43} - G_{32}}{2}\right| + \left|\dfrac{G_{34} - G_{23}}{2}\right| + \left|G_{44} - G_{33}\right| + \left|G_{33} - G_{22}\right|}$$

$$\alpha_{35} = \frac{1}{1 + \left|\dfrac{G_{45} - G_{36}}{2}\right| + \left|\dfrac{G_{34} - G_{25}}{2}\right| + \left|G_{44} - G_{35}\right| + \left|G_{35} - G_{26}\right|}$$

$$(3.7)$$

$$\alpha_{53} = \frac{1}{1 + \left|\dfrac{G_{43} - G_{52}}{2}\right| + \left|\dfrac{G_{54} - G_{63}}{2}\right| + \left|G_{44} - G_{53}\right| + \left|G_{53} - G_{62}\right|}$$

$$\alpha_{55} = \frac{1}{1 + \left|\dfrac{G_{45} - G_{56}}{2}\right| + \left|\dfrac{G_{54} - G_{65}}{2}\right| + \left|G_{44} - G_{55}\right| + \left|G_{55} - G_{66}\right|}$$

Finally, we proceed to fill the rest the missing R and B values at observed G. As shown in Fig. 3.9, R_{43} is estimated as equation 3.8 and 3.9. Likewise, the B_{43} is interpolated as the same way. Just replace the R with B in equation 3.8 and 3.9. Also note that the dark red and dark blue are the estimation value from last step.
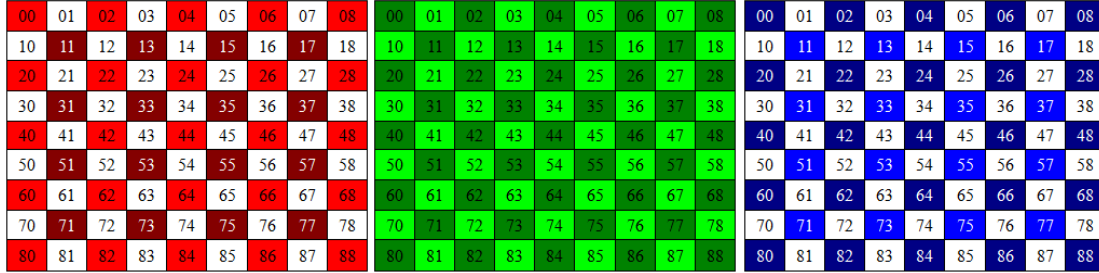
Fig. 3.9 Reconstructed G plane and half-reconstructed R, B plane

$$\widetilde{R}_{43} = \frac{\alpha_{33}\widehat{R}_{33} + \alpha_{42}\widehat{R}_{42} + \alpha_{44}\widehat{R}_{44} + \alpha_{53}\widehat{R}_{53}}{\alpha_{33} + \alpha_{42} + \alpha_{44} + \alpha_{53}}$$

$$where \quad \widehat{R}_{33} = R_{33} + (G_{43} - G_{33}) \qquad \widehat{R}_{42} = R_{42} + (G_{43} - G_{42}) \qquad (3.8)$$

$$\widehat{R}_{44} = R_{44} + (G_{43} - G_{44}) \qquad \widehat{R}_{53} = R_{53} + (G_{43} - G_{53})$$

$$\alpha_{33} = \cfrac{1}{1 + \left|\cfrac{G_{42} - G_{32}}{2}\right| + \left|\cfrac{G_{32} - G_{22}}{2}\right| + \left|\cfrac{G_{44} - G_{34}}{2}\right| + \left|\cfrac{G_{34} - G_{24}}{2}\right| + \left|G_{43} - G_{33}\right| + \left|G_{33} - G_{23}\right|}$$

$$\alpha_{42} = \cfrac{1}{1 + \left|\cfrac{G_{33} - G_{32}}{2}\right| + \left|\cfrac{G_{32} - G_{31}}{2}\right| + \left|\cfrac{G_{53} - G_{52}}{2}\right| + \left|\cfrac{G_{52} - G_{51}}{2}\right| + \left|G_{43} - G_{42}\right| + \left|G_{42} - G_{41}\right|}$$

$$\alpha_{44} = \cfrac{1}{1 + \left|\cfrac{G_{33} - G_{34}}{2}\right| + \left|\cfrac{G_{34} - G_{35}}{2}\right| + \left|\cfrac{G_{53} - G_{54}}{2}\right| + \left|\cfrac{G_{54} - G_{55}}{2}\right| + \left|G_{43} - G_{44}\right| + \left|G_{44} - G_{45}\right|}$$

$$\alpha_{53} = \cfrac{1}{1 + \left|\cfrac{G_{42} - G_{52}}{2}\right| + \left|\cfrac{G_{52} - G_{62}}{2}\right| + \left|\cfrac{G_{44} - G_{54}}{2}\right| + \left|\cfrac{G_{54} - G_{64}}{2}\right| + \left|G_{43} - G_{53}\right| + \left|G_{53} - G_{63}\right|}$$

(3.9)

We may observer that the weights α of this step are all concern about G. As we mentioned before, G plane is used to assist R and B interpolation since it contains more accurate data from CFA. Now the image from CFA sampled has been fully reconstructed. We get two reconstructed data along horizontal and vertical direction. The mission of next step is to choose the direction which has fewer artifacts.

D. Homogeneity Map

The homogeneity map is presented in [22]. As introduced in section 2.4.6, this technique is able to achieve significant result around edges. Our proposed algorithm also exploits this technique. This step is processed by the following statements:

1) We have two reconstructed image along different direction, named $R_H(i, j)$ and $R_V(i, j)$. Transform them into CIELab color space, $R_{H,Lab}(i, j)$ and $R_{V,Lab}(i, j)$.

2) Calculate the homogeneity map of $R_{H,Lab}(i, j)$ and $R_{V,Lab}(i, j)$. Detail concepts and computations can refer to [22].

3) The homogeneity map $H_H(i, j)$ and $H_V(i, j)$ are used to combine $R_H(i, j)$ and $R_V(i, j)$ to final output, as given by equation 3.10. Note that A is a lowpass filter such as an averaging filter.

$$R(i, j) = \begin{cases} R_H(i, j) & ,if \ A * H_H(i, j) \geq A * H_V(i, j) \\ R_V(i, j) & ,if \ A * H_H(i, j) < A * H_V(i, j) \end{cases}$$

(3.10)

We may wonder why the map makes convolution with an averaging filter. Since frequent switch from interpolation in one direction to another may cause some discontinuities of $R(i, j)$, taking a average of the homogeneity map can reduces the problem of discontinuity. Fig. 3.10 depicted the homogeneity map of lighthouse. White part means the homogeneity of horizontal direction is larger the vertical. We should choose this direction which may contains few artifacts. Black part is otherwise.
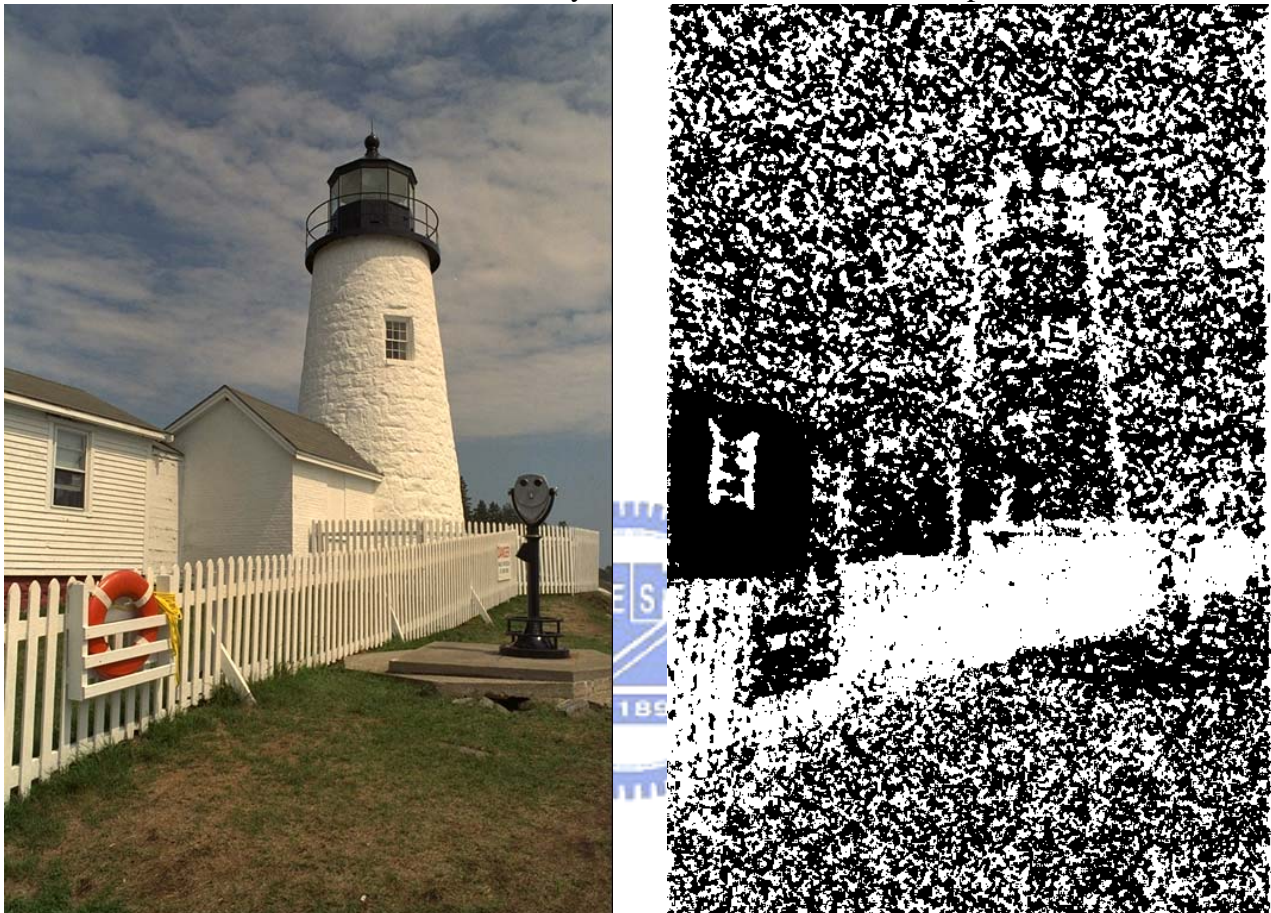
Fig. 3.10 Homogeneity map of lighthouse

E. Results

Now the output of first stage: interpolation step is completed by applying all the interpolation steps described above. The following figure makes a quick review of all steps in this stage. See Fig. 3.11.

Fig. 3.11 Rough figure description of interpolation step

The next section will introduce the second stage: post-processing step. Recursive processes we used and the stop criterion are the main points of that section.

3.5.2 Stage 2: Post-processing Step with Adaptive Stop Criterion

In our proposed post-processing algorithm, we use three different types of post-processing as shown in Fig. 3.12. These are spatial correlation iteration and

Stage 2: Post-Processing Step

Start
↓
Spatial correlation iteration
↓
Detail and observation projection
↓
End
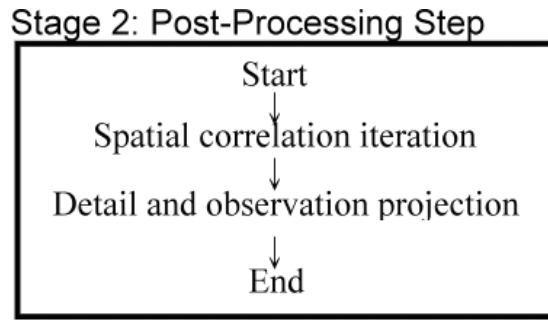
Fig. 3.12 Flowchart of the post-processing step

detail and observation projection. The first step is achieved by combining the post-processing in [10] with the observation projection in [15]. The second post-processing that we used has been shown in [15]. So the following just introduce spatial correlation iteration.

A. Spatial Correlation Iteration

The post-processing in [10] has been discussed in section 3.3. However, we find some data sampled from the CFA would be revised without turning these back to the observed ones. In order to turning back, we utilize the observation projection in [15] to return the original color values. Therefore, this extension combining the median filter and the observation projection then become iterative. This extension can modify the initial estimations from interpolation and improve them substantially. We summary this post-processing step as the algorithm described below:

1) Use the Laplacian operator to define the edge map, given by equation 3.3.
2) Apply the median filter to adjust these artifact-prone regions using equation 3.2.
3) Restore the observed data using the observation projection.

Repeat it as m times, defined by the user.

B. Arrangement of the post-processing

The methods we introduced in this chapter are all effective in suppressing the demosaicking artifacts. Do them also work well if we putting these method together? How to arrange these post-processing? To find the answer we need to understand the influences to the image of each post-processing. We discuss these in the view of performance measurement: peak signal-to-noise ratio (PSNR) and the CIELAB color difference value ($\triangle E_{ab}^{*}$) introduced in chapter 2 before. For the first one, spatial

correlation iteration, it can improve the PSNR of the three color plane and $\triangle E_{ab}^{*}$, and

the second one is able to refine the PSNR only to R and B color plane as well as

$\triangle E_{ab}^*$. In the proposed post-processing algorithm, we arrange these methods in the

purpose of minimize the color difference $\triangle E_{ab}^*$. Since the PSNR of G plane only has

the chance to be improved in spatial correlation iteration, and the G plane accuracy is also important for the detail and observation projection. We arrange the spatial

correlation iteration first to upgrade the PSNR of all plane and $\triangle E_{ab}^*$. And the detail

and observation then upgrade quality again except for the PSNR of G plane. Therefore, in our proposed post-processing, we arrange these two methods as depicted in Fig. 3.12. The question is how many times should all post-processing done? It may be concern with the image correlation no matter in spatial domain or in frequency domain. The following will give a discussion about this.

C. Stop Criterion for Iteration in the Post-processing Step

The necessity of setting a stop criterion has been discussed in section 3.4. Before creating the stop criterion, we need to understand the assumptions made in the post-processing step. The two steps depicted in Fig. 3.12 have their own property.

1) The spatial correlation iteration uses the median filter calculating by equation 3.2. But if the inter-plane correlation is not good enough, the result from the median filter would not be so correct. As a whole, the R_{adjust}, G_{adjust} and

    B_{adjust} are deviate far away from the original distribution, not to say repeating

    this step many times.
2) The detail and observation projection replaces the detail subbands of R and B color plane with the detail subbands of G. However, if the inter detail subbands correlation coefficients are not larger than 0.9, the iteration may not be able to improve the image quality very effectively, similar to the discussion in section 3.5.1(B).

Although we understand the conditions of executing the post-processing beforehand, we can not predict whether the image we processing is hold the assumptions or not. Fortunately, the technique we used in section 3.5.1(B) and Table 3.2 can give a good prediction of approximating the inter-plane correlation. Since we can predict the inter-plane correlation in advance, we decide to set a stop criterion for the spatial correlation iteration, i.e., the first step of our proposed post-processing. There are two keypoints of the stop criterion: 1) If the image is not suitable to execute the post-processing step, do not enter it to the process. 2) If the image is fit, do the

iteration and stop it when the visible artifacts may appear.

Our implementation of stage 2 can be renewed as shown in Fig. 3.13. We can see the judgment at the first step. If the image get no improvement from the
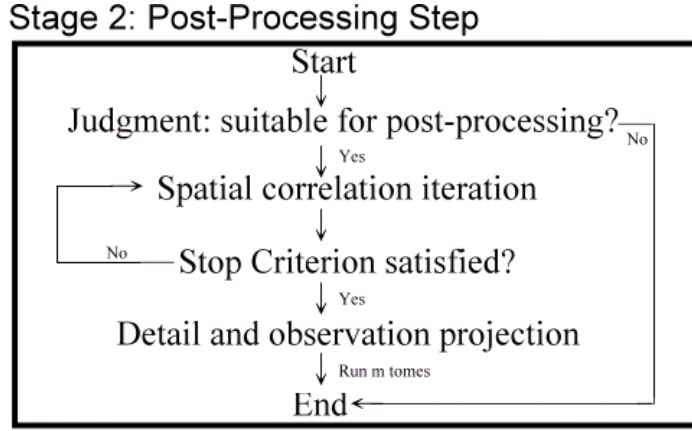
Fig. 3. 13 The flow of the post-processing with the stop criterion

post-processing, the process would not execute on this image. If the image is suitable to do the process, the two methods would apply in the order depicted above. Since the image property for spatial correlation iteration can be predicted, we should carefully observe the correlation between two iteration and then use the stop criterion to minimize the risk of suffering from the artifacts.

In the process of searching the stop criterion, we focus on the distribution of the inter-plane correlation. We discovered that if the post-processing can not improve the performance, the inter-plane correlation would distribute separately, i.e., the difference of the inter-plane correlation between two iterations would be large. To straightly reveal the distribution of the inter-plane correlation, we execute the spatial correlation iteration by changing the number of iteration from zero to eight, and then calculate the standard deviation σ respect to R to G correlation and B to G correlation respectively. We take $\frac{1}{10}\sigma$ as an index value and use it to judge the iteration as following equation.

$$\begin{cases} Diff_{R-G} = \left| C_{R-G}{}^{n+1} - C_{R-G}{}^{n} \right| \leq k \cdot index \\ Diff_{B-G} = \left| C_{B-G}{}^{n+1} - C_{B-G}{}^{n} \right| \leq k \cdot index \end{cases} \quad (k = 1, 2, 3, ...) \qquad (3.11)$$

where C_{R-G} and C_{R-G} denote the R to G correlation and B to G correlation and $Diff_{R-G}$ denotes the difference of the $n+1$th iteration and the nth iteration. In general, each image has own inter-plane correlation and k value while best case happened. We then run all the test images in the Fig. 3.25 and make a statistic of best case depicted as Fig. 3.14.

Fig. 3.14 The statistical graph of the k value correspond to the inter-plane correlation

In Fig. 3.14, the vertical coordinate means the k value which is close to the optimal solution, and the horizontal coordinate represents the inter-plane correlation of each test images in Fig. 3.25. However, this figure records the best case of each test image. In order to approximate the optimal solution, we utilize the curve fitting to minimize the error between the base case and the optimal one [see figure left-hand side]. The result of optimal solution is shown as equation 3.12 and is used to set the stop criterion and judgment. Since the inter-plane correlation can be predicted in advance, we can use equation 3.12 to determine the k value. And the criterion will judge the image before the post-processing.

$$k = -27.9954 \cdot Cor + 27.5538 \qquad (3.12)$$

Note that Cor represents the inter-plane correlation we predicted from the result of conventional interpolation.

The judgment and the stop criterion are processing as below:

1) Judgment: If the inter-plane correlation is smaller than 0.75, the image would not enter the post-processing.

2) Criterion: If the image has passed the judgment, k value is decided according to equation 3.12.

3.6 Comparison and Experimental Results

So far we have introduced lots of demosaicking algorithms above, some methods even employed in commercial cameras today. And we also point out few drawbacks and present a hybrid iterative demosaicking algorithm. Now we want to make comparisons and display their performances. In our experiments, we compare them not only visually but also in terms of performance measurements. For the visual comparison, we use two different kinds of test images. One kind is some synthesis images. These particular images are able to emphasis the fine details that every algorithm works on. In other words, these images consider the extreme cases for Bayer CFA. Another kind has twenty-four images which are popularly used to compare in demosaicking field. We will display some region-of-interest (ROI) to reveal the effects of different algorithms. Eventually, we directly see the performance according to the measurements mentioned in section 2.3.

3.6.1 Synthesis Images

The following figures are the test patterns we used. Fig. 3.15(a.) is gray level and

(a.)   (b.)
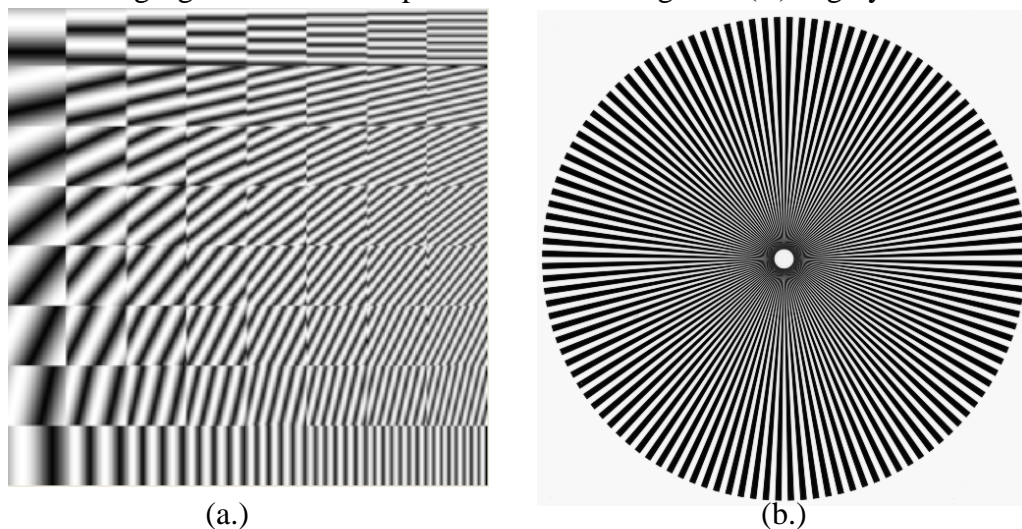
Fig. 3.15 Synthesis test images

consists of 8 by 8 blocks. Each block has different directions and increasing spatial frequencies. Fig. 3.15(b.) is a binary image and has edges in almost directions.

Likewise, it also has the decreasing spatial frequencies away from the center. Fig. 3.16 shows the results of different demosaicking algorithms processed on Fig. 3.15(a).

(a.)

(b.)

(c.)

(d.)

(e.)

(f.)
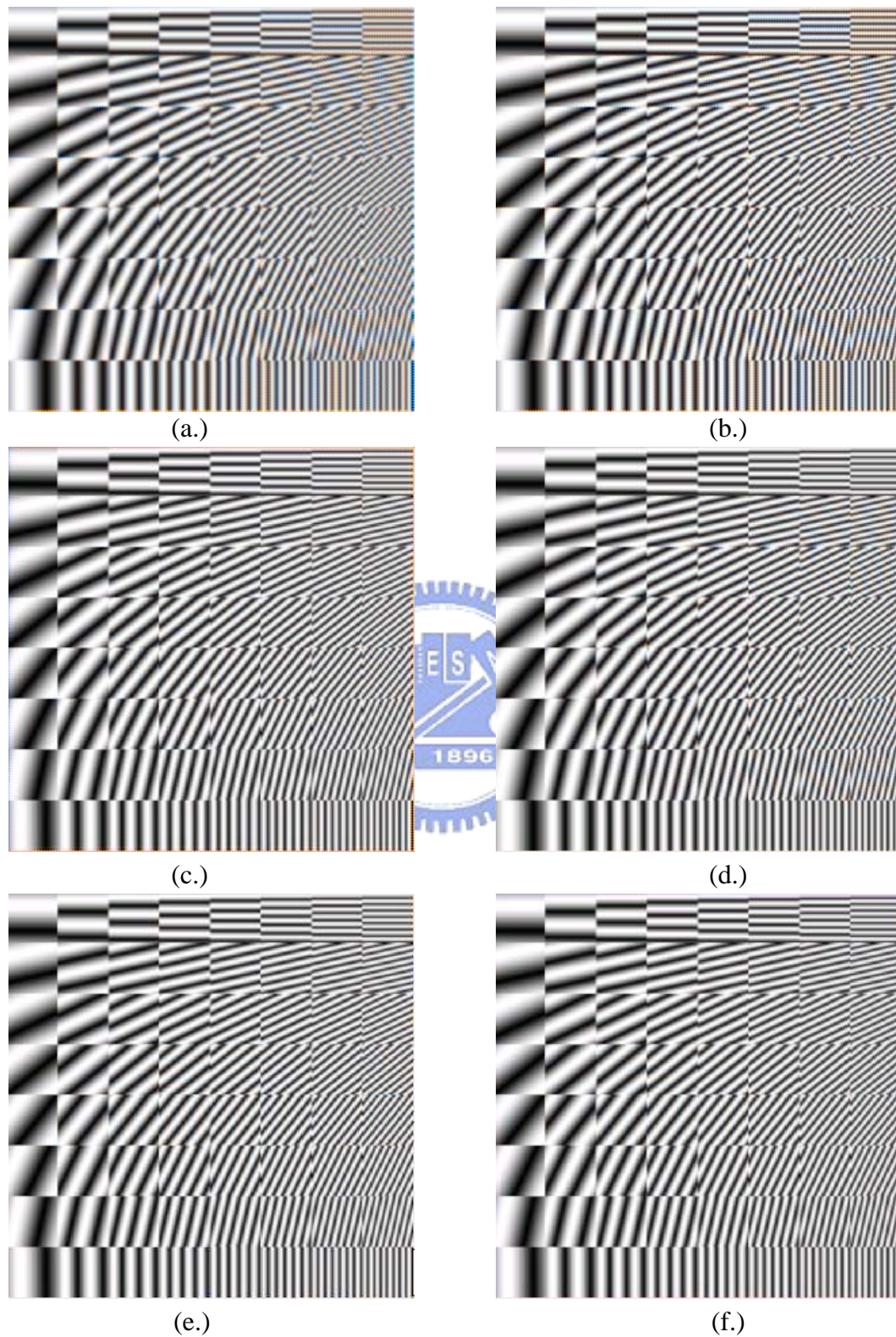
Fig. 3.16 Demosaicking results of Fig. 3.15(a.)

(a.) Bilinear (b.) Conventional [6] (c.) POCS [15]

(d.) New [10] (e.) Homogeneity [22] (f.) Proposed

And we define ROI of Fig. 3.15(a.) in order to observe the effects clearly of each algorithm. The ROI is depicted as Fig. 3.17.
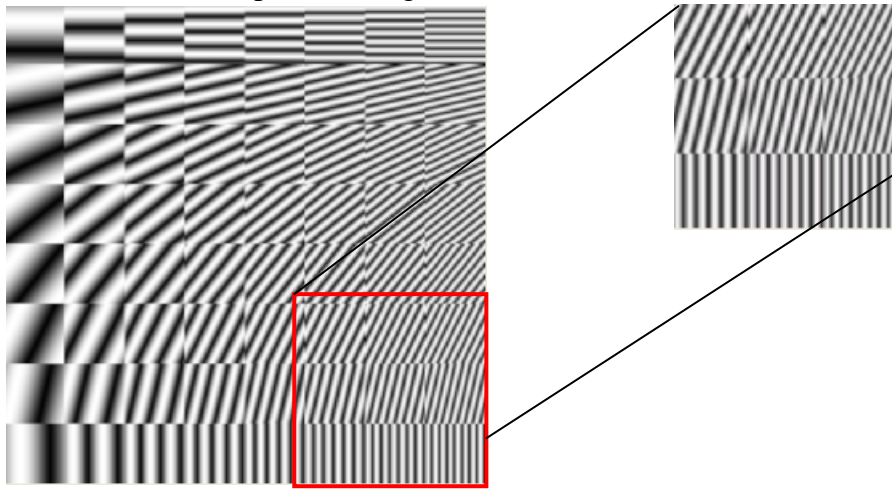
Fig. 3.17 ROI region of Fig. 3.15(a.)

Fig. 3.18 them depicts the demosaicking results processed on Fig. 3.17.
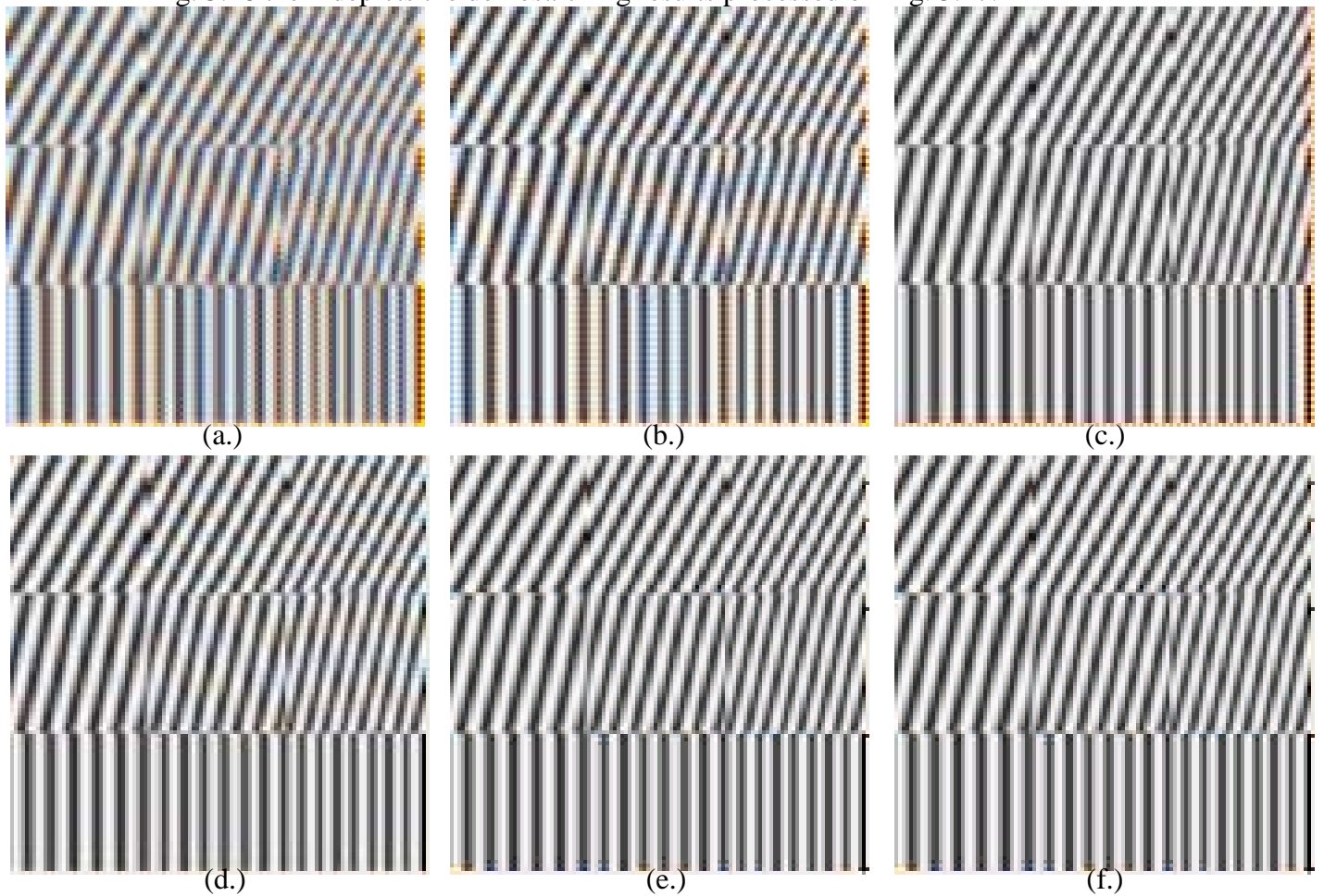
Fig. 3.18 Demosaicking results of Fig. 3.17 (ROI)

(a.) Bilinear (b.) Conventional [6] (c.) POCS [15]

(d.) New [10] (e.) Homogeneity [22] (f.) Proposed

In Fig. 3.18, we can visually recognize the aliasing of high-frequency regions. Bilinear is the worst result which been damage by aliasing and even blurring. Conventional makes improvement of blur but still has aliasing problems. POCS and New get better performance. The aliasing almost disappears but still exists lightly. Homogeneity and Proposed algorithm have the best results. It is hard to distinguish between the original image and the reconstructed one. The last four algorithms seem to perform better since they all utilize post-processing to modify initial estimations. Method (c.), (e.) and (f.) even use recursive approach to suppress visible artifacts.

Now we demosaicking on another test pattern shown in Fig. 3.15(b.). However, this figure has high resolution. It is hard to identify the aliasing and decide the performance. Since this figure is circle and symmetric for up-down or left-right direction, we can define the ROI by one quarter of this circle, as shown in Fig. 3.19.
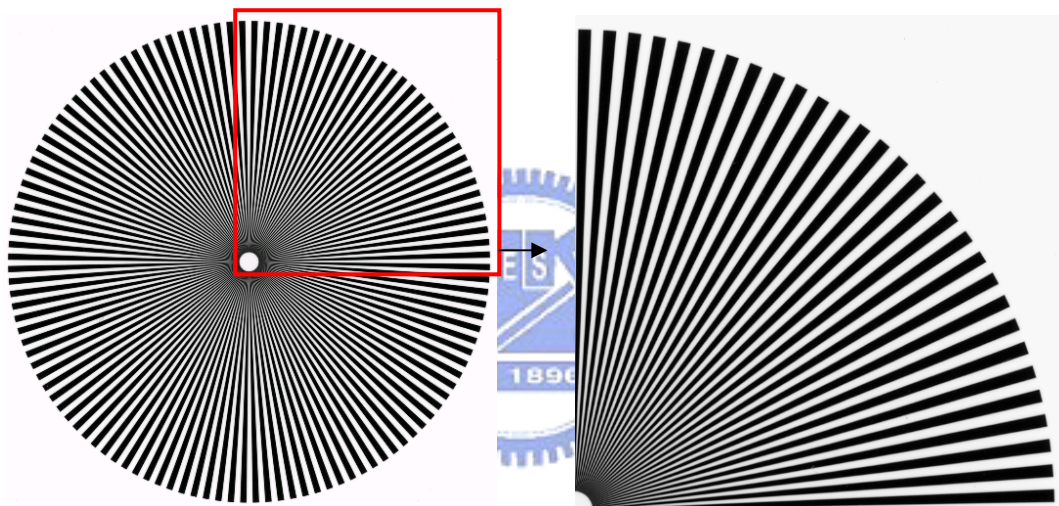
Fig. 3.19 ROI region of Fig. 3.15(b.)

And the results of different algorithms are shown in Fig. 3.20.
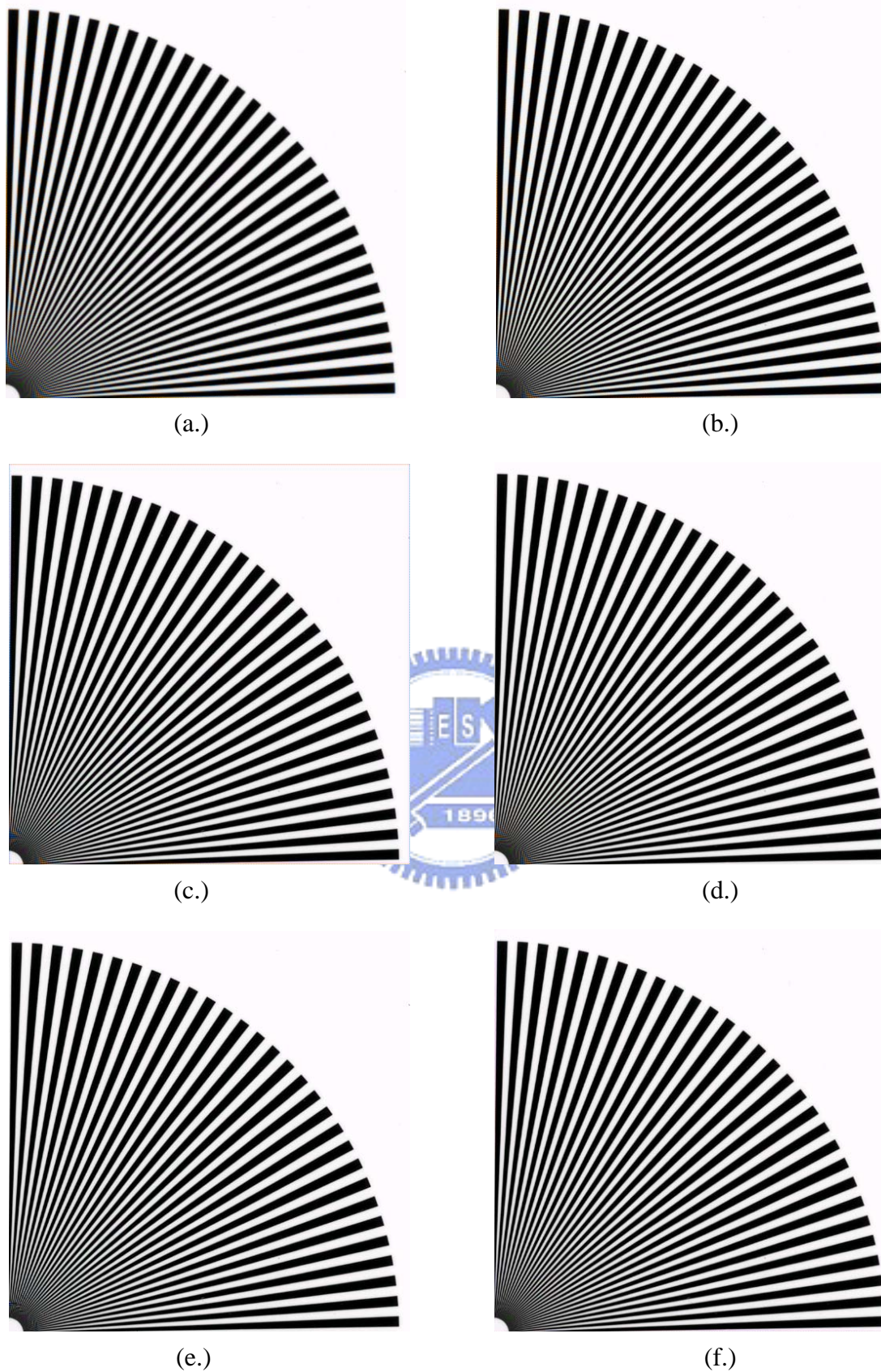
(a.)

(b.)

(c.)

(d.)

(e.)

(f.)

Fig. 3.20 Demosaicking results of Fig. 3.19 (ROI)

(a.) Bilinear (b.) Conventional [6] (c.) POCS [15]

(d.) New [10] (e.) Homogeneity [22] (f.) Proposed

As shown in Fig. 3.20, the artifact-prone regions are located near the center of the circle which has high spatial frequency. And the results have similar trends between these algorithms as we seen in the previous test pattern.

3.6.2 Natural Scenes Images

We use the following figures shown in Fig. 3.21 and Fig. 3.22 for our test images. For the purpose of observe easily, we all process these images of specific ROI which may contain edges and fine details.

Fig. 3.21 ROI region of Fig. 3.25 #19

Fig. 3.22 ROI region of Fig. 3.25 #8

Fig. 3.23 and Fig. 3.24 display the results of above two figures respectively.

(a.)   (b.)   (c.)

(d.)   (e.)   (f.)
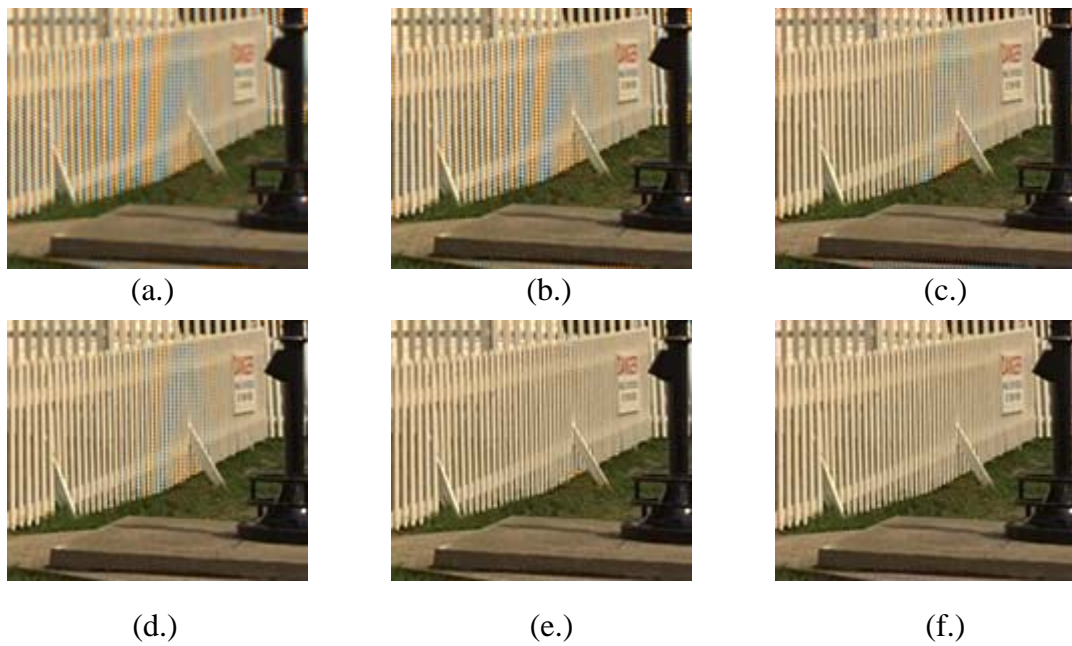
Fig. 3.23 Demosaicking results of Fig. 3.21 (ROI)
(a.) Bilinear (b.) Conventional [6] (c.) POCS [15]
(d.) New [10] (e.) Homogeneity [22] (f.) Proposed

(a.)   (b.)   (c.)

(d.)   (e.)   (f.)
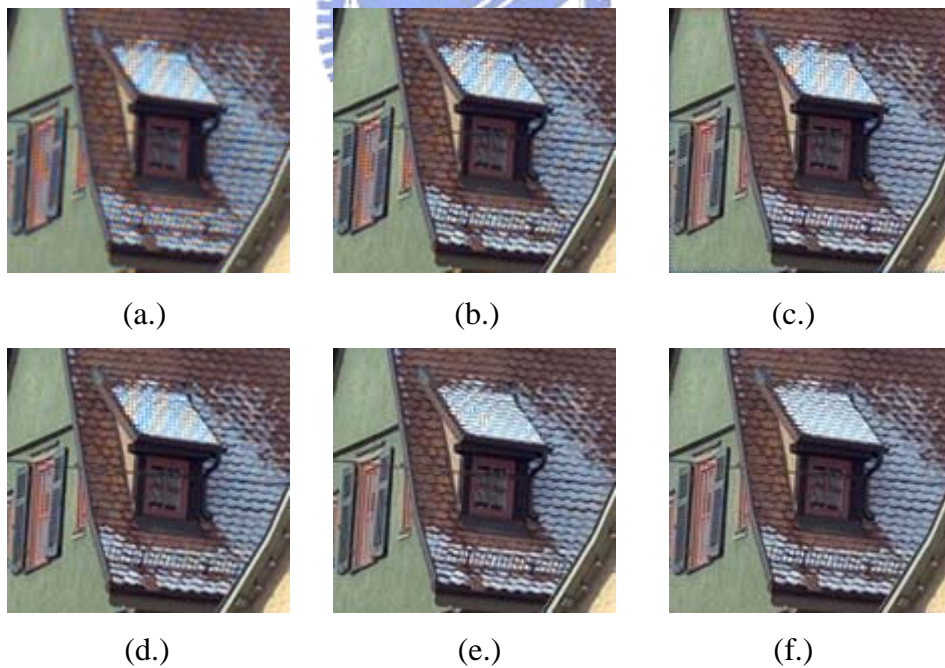
Fig. 3.24 Demosaicking results of Fig. 3.22 (ROI)
(a.) Bilinear (b.) Conventional [6] (c.) POCS [15]
(d.) New [10] (e.) Homogeneity [22] (f.) Proposed

As can be seen from Fig. 3.23, there exists aliasing around the fence. Fig. 3.23(a.)

to (d.) are all suffer from visually artifacts. But Fig. 3.23(d.) and (e.) makes good performance of this specific region. Likewise, aliasing occurs on the rooftop of the window in Fig. 3.24. The trend of performance is similar to Fig. 3.23.

3.6.3 Performance Measurement Results
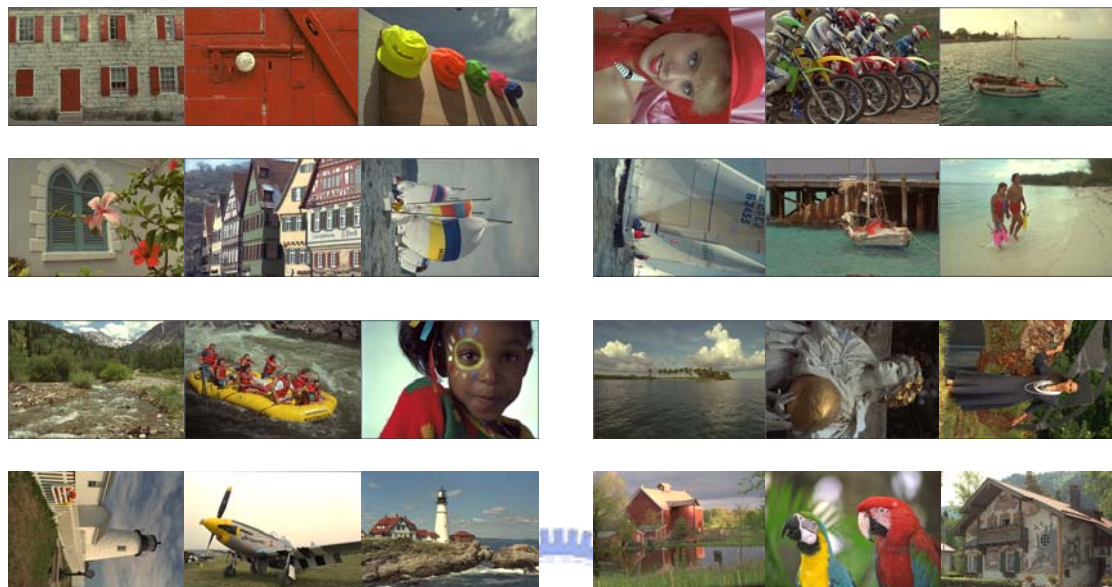
Fig. 3.25 Test images
(These images are marked as Image 1 to Image 24, from the left-to-right, and top-to-bottom)

Although we can visually observe the effect of each algorithm, it is not easy to choose the better one from similar performance. To compare each algorithm precisely, we adopt the performance measurements mentioned in section 2.3. These measurement indexes conclude PSNR, $\triangle E_{ab}^{*}$ and SSIM. In our experiments, we use the test images shown in Fig. 3.25. These natural images from the Kodak Photo are commonly use for the current demosaicking and can be available in [26]. For our proposed demosaicking algorithm, we use the parameter $m = 2$ for the post-processing depicted in Fig. 3.13. We demonstrate our proposed method by comparing it with six state-of-the-art demosaicking method—bilinear interpolation, Gunturk's method [15], Lu and Tan's method [10], Alleysson's method [23], Hirakawa's method [22] and Li's method [20]. For the Gunturk's method, we set the iteration number is 7 and the threshold T as 0.02 and make use of the one-level decomposition of the subbands. For the Hirakawa's method, we set $\delta = 2$. The image quality in terms of PSNR, $\triangle E_{ab}^{*}$ and SSIM are reported in Table 3.3, 3.4 and 3.5,

respectively. Note that the bold type value means the best one through the algorithms we compared in this test image.

Table 3.3 Peak Signal-to-noise Ratio Comparison of Different Demosaicking Method

Image No.	Channel	Bilinear	Method [15]	Method [10]	Method [23]	Method [22]	Method [20]	Proposed
1	R	24.6841	35.7346	32.3942	34.9475	34.6206	36.6601	**39.2554**
	G	29.3635	38.9064	36.8346	39.5243	36.2820	40.8909	**41.4683**
	B	29.2954	35.9257	35.4537	35.2839	34.7859	37.6548	**38.2121**
2	R	30.5583	35.0137	32.4868	34.0877	36.4087	35.5249	**38.1941**
	G	35.4630	38.4480	40.6330	39.4376	**41.5646**	40.0856	40.8978
	B	31.4180	36.0592	38.9858	36.1975	**40.1705**	38.9228	37.9774
3	R	31.1295	38.4768	33.9918	38.4244	40.6392	38.9541	**41.6784**
	G	36.0856	40.5146	41.3518	41.9124	43.7566	42.0993	**43.9398**
	B	32.6765	37.1935	38.7537	38.0033	**40.1532**	38.9456	40.1372
4	R	30.8966	36.4687	33.2129	**39.9754**	36.6715	36.8343	39.1537
	G	35.7442	39.4182	40.5648	40.8305	**41.4141**	40.8581	40.9721
	B	32.3929	39.9686	39.8046	38.9362	40.6165	**40.7602**	39.5840
5	R	25.1783	35.7410	32.7734	34.8472	35.1472	35.4555	**38.5762**
	G	29.0823	37.9827	37.9392	38.3493	37.4663	38.0781	**40.3361**
	B	25.9916	34.8139	**35.5474**	34.6245	34.4349	35.1111	35.2181
6	R	25.9985	36.8372	32.8373	36.0509	37.6040	37.7778	**40.3441**
	G	30.7318	39.5360	37.8396	40.6410	39.1382	41.4063	**43.1370**
	B	26.7381	35.7318	35.4225	35.4588	36.4738	37.1654	**37.5487**
7	R	30.7217	39.1486	34.3171	38.6888	40.1131	40.0737	**42.1312**
	G	35.5465	41.0277	41.5756	42.2447	42.7181	42.7468	**44.1054**
	B	32.0169	37.3317	38.7901	37.7623	39.0557	**39.3064**	38.3749
8	R	22.2966	33.8624	31.3766	31.3617	33.2216	34.2794	**38.8360**
	G	27.2854	37.3833	35.7007	36.5403	35.3680	38.5543	**39.1466**
	B	22.7166	33.8196	33.3655	31.5061	33.2576	34.9584	**35.2547**
9	R	29.9406	39.6149	34.2896	39.0182	40.6981	40.9267	**42.1486**
	G	35.1474	41.4774	41.2255	42.6450	43.0743	44.0068	**44.2825**
	B	31.5447	38.2619	39.0589	38.7539	39.8952	**40.4849**	40.1774
10	R	29.9322	39.5299	34.3887	39.7949	40.0783	40.3706	**41.4405**
	G	34.7878	41.4364	41.4493	43.4449	42.9230	43.6376	**43.6739**
	B	31.4499	38.3414	38.9456	39.4017	39.5119	**40.2123**	39.5449
11	R	27.5131	36.9857	33.2669	36.3333	36.6602	37.4353	**39.8441**
	G	32.0102	39.9488	38.7444	40.9616	39.0450	41.6653	**42.4235**
	B	28.3983	37.2063	37.3247	37.3147	37.4883	38.4982	**38.7601**
12	R	30.1784	39.8918	34.4169	38.9180	40.6058	41.0958	**42.1009**
	G	35.7831	42.1194	41.7382	43.4932	44.0297	**44.5264**	44.4664
	B	32.0500	38.7687	39.2680	39.2741	40.9713	**41.4236**	40.3014
13	R	22.8444	33.6926	30.8484	34.4930	31.5343	34.4419	**36.1295**
	G	26.4047	36.0145	33.2084	37.6598	32.4086	37.5530	**38.6564**
	B	23.1188	32.5773	31.5973	33.2128	30.6164	33.2735	**33.9967**
14	R	27.4480	33.8506	32.2438	32.3152	34.1703	33.2568	**37.8873**
	G	31.6848	37.0140	38.1796	36.7797	38.0151	36.5378	**39.7978**
	B	28.2134	33.4978	**35.7796**	32.9697	34.9453	33.6036	35.4481
15	R	28.8948	35.3817	32.3507	34.7037	35.5073	35.2978	**38.1219**
	G	34.0925	39.2425	39.6735	40.2753	40.6966	40.3236	**40.9227**
	B	30.3953	37.0317	37.7602	37.0102	38.6001	**38.6941**	38.4801
16	R	29.0113	38.7294	33.4692	38.6999	41.4353	38.6298	**43.2914**
	G	34.0251	41.1583	39.7110	43.5030	42.9261	43.3823	**46.3576**
	B	29.6993	37.6698	33.7101	38.2501	40.6183	39.3689	**41.3128**
17	R	29.6539	38.3534	33.7554	39.6231	39.3799	38.3577	**41.3375**
	G	33.8688	40.3636	39.5400	42.9592	40.8211	42.4780	**43.8117**
	B	30.5022	37.2144	37.7809	38.6909	38.2701	38.8816	**39.0416**
18	R	26.7376	34.3462	32.8506	35.4349	34.0038	35.5331	**36.7171**
	G	30.2492	37.5391	36.0966	**38.7971**	35.6875	38.5239	38.5920
	B	27.0037	35.3231	34.2786	34.7155	33.2761	35.1862	**35.4229**

19	R	26.1501	37.2663	32.0194	35.9729	37.9696	37.6820	**40.2023**
	G	31.3420	39.4156	38.7791	40.6866	39.6739	42.1023	**42.6246**
	B	27.1095	**38.6897**	37.1109	35.8657	37.4932	38.3847	38.7023
20	R	29.0816	35.5636	33.7482	37.9151	**38.9239**	38.3538	38.5573
	G	33.0888	37.3779	39.2275	41.6877	40.6775	41.4824	**42.0306**
	B	28.4438	35.9963	31.3022	36.2254	36.9343	36.9313	**37.5166**
21	R	27.1632	37.0983	33.7587	36.7682	36.6396	38.2112	**39.6253**
	G	31.3600	38.7586	38.0590	41.0174	37.9464	41.5733	**41.9749**
	B	27.5408	34.8800	35.9813	36.0150	35.5877	**37.4274**	36.8998
22	R	29.1831	35.4084	33.9713	36.3022	35.7033	36.1079	**37.4339**
	G	33.1174	37.8446	38.9436	39.2482	38.4803	39.7031	**40.0064**
	B	29.3487	35.1373	36.7683	35.4534	35.4865	**36.8836**	36.3649
23	R	31.3377	37.7621	33.2818	37.1895	38.9823	37.6577	**40.6403**
	G	36.8178	40.1441	41.6624	41.3245	42.2828	41.9007	**43.8409**
	B	33.7479	38.8050	39.7045	37.8592	39.6315	**40.2823**	39.4444
24	R	26.3319	32.5037	33.8326	**35.2495**	32.6299	33.6921	34.0810
	G	29.4064	34.7295	35.4127	**37.8917**	34.9580	36.7272	37.3236
	B	22.2652	31.7337	31.4127	**32.6206**	31.6108	32.8012	32.4338
Average	R	28.0361	36.5526	33.1618	36.5465	37.0562	37.1921	**39.4887**
	G	32.6037	39.0751	38.9203	40.4940	39.6814	40.8685	**41.8662**
	B	28.8982	36.2491	36.4128	36.3086	37.0786	37.7151	**37.7565**

Table 3.4 CIELAB Color Difference Comparison of Different Demosaicking Method

Image No.	Bilinear	Method [15]	Method [10]	Method [23]	Method [22]	Method [20]	Proposed
1	4.2846	1.4103	1.5438	1.5101	1.2475	1.2724	**1.0860**
2	2.0355	1.2207	1.1749	1.2637	0.9136	1.1096	**0.9053**
3	1.4323	0.8784	0.8791	0.7906	**0.6054**	0.7994	0.7098
4	1.9231	1.0482	1.0848	1.0179	0.9127	1.0138	**0.8898**
5	4.7072	1.9133	1.8027	1.9409	1.6661	1.9795	**1.5934**
6	2.9889	1.1171	1.2016	1.1533	0.8520	1.0258	**0.8317**
7	1.6837	0.9704	0.9344	0.9729	**0.7751**	0.8915	0.8164
8	5.2150	1.7296	1.7877	2.0732	1.4885	1.5906	**1.4259**
9	1.7740	0.8962	0.9209	0.8703	**0.6992**	0.8019	0.7422
10	1.7708	0.8738	0.9291	0.8504	**0.7335**	0.8070	0.7749
11	3.0311	1.2593	1.3561	1.3036	1.0395	1.1592	**0.9965**
12	1.4015	0.6884	0.7514	0.6893	**0.5150**	0.5907	0.5893
13	5.3043	1.9558	2.1473	1.7842	1.9213	1.8011	**1.5877**
14	3.3424	1.7545	1.4995	1.6623	1.2910	1.7535	**1.2447**
15	2.2616	1.2779	1.3258	1.2829	1.0737	1.2322	**1.0629**
16	2.6079	1.0608	1.1544	1.0790	**0.7464**	0.9660	0.7618
17	2.6012	1.3741	1.4479	1.2820	**1.1383**	1.2588	1.1450
18	3.7096	1.8634	1.8631	1.8436	1.8606	1.9673	**1.6736**
19	2.7994	1.1349	1.2013	1.1689	1.0126	1.0721	**0.9456**
20	1.9289	1.0323	1.0318	0.9411	0.8642	0.9821	**0.8532**
21	2.9844	1.2066	1.3068	1.2248	1.0943	1.0995	**1.0170**
22	2.2649	1.2774	1.2020	1.2122	1.1743	1.2075	**1.0928**
23	1.2018	0.8547	0.8531	0.8249	0.7071	0.8218	**0.7016**
24	2.9500	1.3158	1.2532	1.2681	1.2489	1.2458	**1.1851**
Average	2.7577	1.2547	1.2772	1.2504	1.0659	1.1854	**1.0263**

Table 3.5 Structural Similarity Comparison of Different Demosaicking Method

Image No.	Bilinear	Method [15]	Method [10]	Method [23]	Method [22]	Method [20]	Proposed
1	0.8081	0.9856	0.9822	0.9814	0.9730	0.9869	**0.9901**
2	0.8981	0.9679	0.9771	0.9509	0.9671	0.9718	**0.9781**
3	0.9325	0.9850	0.9869	0.9827	0.9844	0.9849	**0.9872**
4	0.9138	0.9783	0.9815	0.9745	0.9729	0.9785	**0.9829**
5	0.8782	0.9861	**0.9883**	0.9816	0.9811	0.9827	0.9878
6	0.8473	0.9851	0.9826	0.9822	0.9815	0.9850	**0.9890**
7	0.9533	0.9877	**0.9903**	0.9842	0.9859	0.9874	0.9885
8	0.8259	0.9846	0.9823	0.9790	0.9756	0.9855	**0.9870**
9	0.9208	**0.9842**	0.9834	0.9821	0.9777	0.9836	0.9837
10	0.9199	0.9852	0.9852	0.9836	0.9798	0.9852	**0.9856**
11	0.8694	0.9845	0.9839	0.9803	0.9799	0.9843	**0.9882**
12	0.9075	0.9852	0.9850	0.9825	0.9819	0.9851	**0.9870**
13	0.7728	0.9817	0.9750	0.9830	0.9597	0.9839	**0.9858**
14	0.8715	0.9791	0.9822	0.9724	0.9758	0.9753	**0.9841**
15	0.9144	0.9746	0.9762	0.9725	0.9683	0.9747	**0.9781**
16	0.8775	0.9876	0.9848	0.9844	0.9846	0.9869	**0.9907**
17	0.9254	0.9880	0.9870	0.9875	0.9819	0.9875	**0.9887**
18	0.8709	**0.9797**	0.9788	0.9777	0.9668	0.9783	0.9792
19	0.8753	0.9842	0.9821	0.9818	0.9744	0.9833	**0.9860**
20	0.9180	0.9713	0.9757	0.9751	0.9691	0.9759	**0.9762**
21	0.8886	0.9810	0.9805	0.9797	0.9731	0.9814	**0.9822**
22	0.8847	0.9716	0.9742	0.9719	0.9637	0.9739	**0.9745**
23	0.9561	0.9818	**0.9854**	0.9769	0.9793	0.9818	0.9836
24	0.8757	0.9829	0.9837	0.9822	0.9760	0.9838	**0.9840**
Average	0.8877	0.9818	0.9823	0.9788	0.9756	0.9820	**0.9845**
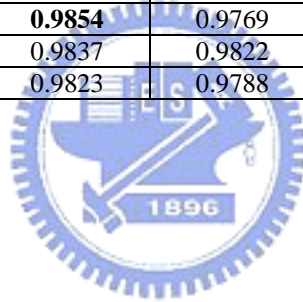
3.6.4 Results

Lots of demosaicking methods have been discovered nowadays, different algorithm may have its own advantages. So compare two algorithm by the image individually may not be fare. To increase the reliability, we should use more test images and then compute the average value of the performance measurement. As shown in Table 3.3, the algorithm we proposed outperforms almost all of various other methods. Although our algorithm just has little improvement in the index PSNR of B plane, we still present competitive result. Another measurement is shown in Table 3.4. We can observe that Hirakawa's method in [22] and our proposed algorithm have the comparable performance among these algorithms. Li's method in [20] also provides satisfactory achievement compare to the remaining algorithm. All of them ([20], [22], proposed) give the discussion about the visible artifacts and aim to suppress them in the post-processing step. So they can work well in reducing the artifacts and also reveal in the color difference $\triangle E_{ab}^{*}$. The last measurement, SSIM, is shown in Table 3.5. Our proposed method has almost highest SSIM. Therefore, despite the similar results in the measurement $\triangle E_{ab}^{*}$ and SSIM, we finally recommend the proposed algorithm as it can has good performance in the measurement PSNR and in human vision as well.

Chapter 4 *Demosaicking Problems of Gastrointestinal Narrow-band Image*

4.1 Introduction

Now we have developed a recursive demosaicking algorithm for Bayer pattern. However, the demosaicking of gastrointestinal (GI) narrow-band Image (NBI) actually is different to normal demosaicking. According to the following figure, the existing capsule endoscope system continually emits white light and NB light
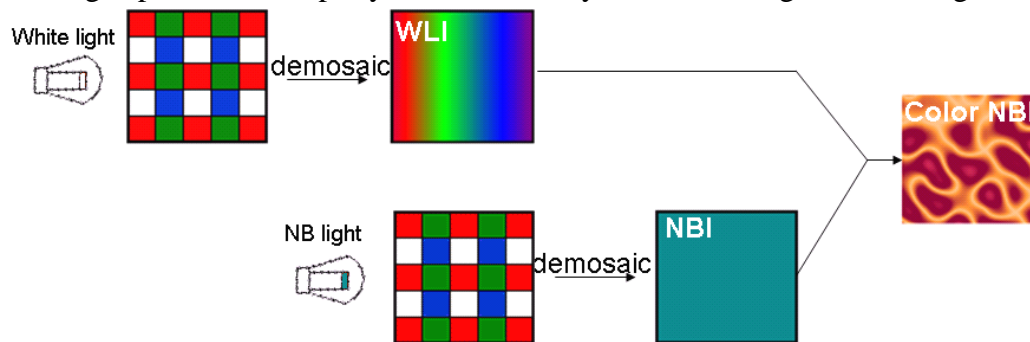
Fig. 4.1 Sensor structure of existing capsule endoscope system

sequentially when capturing image. And the CFA in used is not Bayer CFA but withdrawing one G component. We focus on the problem of reconstruct the white light image (WLI) by only three samples in 2-by-2 CFA block. In this chapter, we will discuss the demosaicking problem based on this issue. And some discussions of different CFA arrangements will also made.

4.2 Modification of the Demosaicking Method for Different CFA Arrangements

4.2.1 RGYB CFA Pattern

The CFA can be chosen from many different kinds. However, the familiar arrangement is withdrawing one G sample from Bayer pattern, depicted by Fig. 4.2.

00	01	02	03	04	05	06	07	08
10	11	12	13	14	15	16	17	18
20	21	22	23	24	25	26	27	28
30	31	32	33	34	35	36	37	38
40	41	42	43	44	45	46	47	48
50	51	52	53	54	55	56	57	58
60	61	62	63	64	65	66	67	68
70	71	72	73	74	75	76	77	78
80	81	82	83	84	85	86	87	88

Fig. 4.2 One sample of Bayer pattern withdrawing one G sample

Note that the word "RGYB" means the order from left-to-right, top-to-bottom of the CFA sample of 2-by-2 square, as shown in Fig. 4.3.

RGYB ⟹
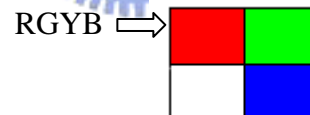
Fig. 4.3 Representation of CFA order

The simplest way is still bilinear interpolation, given by equation 4.1.

$$R_{R,G,B}(i, j) = I(i, j) * \frac{1}{4}\begin{bmatrix} 1 & 2 & 1 \\ 2 & 4 & 2 \\ 1 & 2 & 1 \end{bmatrix} \qquad (4.1)$$

Needless to say, the performance tends to be dissatisfied.

The sensor located at withdrawing G has no filter covered. When NB light emitting, this location is sense the N data. Besides, we can choose to open the sensor or not while white light emitting. In order to improve image quality, we decide to open it

since it can provide Y information when demosaicking WLI. Then we use the conventional method with the assist of Y information, given by equation 4.2.

$$G - G_{lpf} = X - X_{lpf}, \ X = R \ or \ B \ or \ Y$$
$$\Rightarrow G = G_{lpf} + \Delta X \tag{4.2}$$

Now we try to modify the proposed algorithm fitting this CFA. Our strategy is to estimate the G value located at Y pixel for the purpose of reconstructing Bayer pattern. Then execute the recursive demosaicking algorithm we proposed. Note that the more accurate the estimated G value is, the better the performance we received.

Hence, we first interpolate the G value located at Y pixel. For example, G_{34} is interpolated by equation 4.3 and 4.4. After that, we obtain an estimated Bayer pattern.

$$\widetilde{G}_{34} = \frac{\alpha_{23}\widehat{G}_{23} + \alpha_{25}\widehat{G}_{25} + \alpha_{43}\widehat{G}_{43} + \alpha_{45}\widehat{G}_{45}}{\alpha_{23} + \alpha_{25} + \alpha_{43} + \alpha_{45}}$$

$$where \ \ \widehat{G}_{23} = G_{23} + \frac{Y_{34} - Y_{12}}{2} \qquad \widehat{G}_{25} = G_{25} + \frac{Y_{34} - Y_{16}}{2} \tag{4.3}$$
$$\widehat{G}_{43} = G_{43} + \frac{Y_{34} - Y_{52}}{2} \qquad \widehat{G}_{45} = G_{45} + \frac{Y_{34} - Y_{56}}{2}$$

$$\alpha_{23} = \frac{1}{1 + \left|G_{45} - G_{23}\right| + \left|G_{23} - G_{01}\right| + \left|Y_{34} - Y_{12}\right| + \left|\dfrac{R_{24} - R_{02}}{2}\right| + \left|\dfrac{B_{33} - B_{11}}{2}\right|}$$

$$\alpha_{25} = \frac{1}{1 + \left|G_{43} - G_{25}\right| + \left|G_{25} - G_{07}\right| + \left|Y_{34} - Y_{16}\right| + \left|\dfrac{R_{24} - R_{06}}{2}\right| + \left|\dfrac{B_{35} - B_{17}}{2}\right|}$$

$$\alpha_{43} = \frac{1}{1 + \left|G_{25} - G_{43}\right| + \left|G_{43} - G_{61}\right| + \left|Y_{34} - Y_{52}\right| + \left|\dfrac{R_{44} - R_{62}}{2}\right| + \left|\dfrac{B_{33} - B_{51}}{2}\right|} \tag{4.4}$$

$$\alpha_{45} = \frac{1}{1 + \left|G_{23} - G_{45}\right| + \left|G_{45} - G_{67}\right| + \left|Y_{34} - Y_{56}\right| + \left|\dfrac{R_{44} - R_{66}}{2}\right| + \left|\dfrac{B_{35} - B_{57}}{2}\right|}$$

Then we proceed to use the proposed demosaicking method on estimated Bayer pattern.

Equation 4.3 and 4.4 used to estimate G located at Y pixel is the weighted sum method. The Y information on this method is just used to improve the accuracy of G candidate by their difference. However, we discover another way to exploit Y

information more. We first reconstruct the R, G and B values located at Y pixel. Then utilize these R, G and B values to calculate Cb and Cr. At last, we have Y, Cb and Cr. Transform them into RGB color space and then withdraw the G plane. This G plane is also an estimated G value located at Y pixel. We summarize above description as following steps.

1) Reconstruct the R, G and B values located at Y pixel by weighted sum method.
2) Downsample the R, G, B and Y plane at the location of Y.
3) Calculate Cb and Cr by equation 4.5.

$$Cb = 128 + \frac{1}{256}\left(-37.945 \times R - 74.494 \times G + 112.439 \times B\right)$$

$$Cr = 128 + \frac{1}{256}\left(112.439 \times R - 94.154 \times G - 18.285 \times B\right)$$

(4.5)

4) Transform Y, Cb and Cr to RGB color space.
5) Withdraw the G plane from RGB color space in last step. Insert all pixels to the place they located initially.
6) Execute the proposed algorithm on estimated Bayer pattern.

We will compare these methods in section 4.2.3.

4.2.2 BGRY CFA Pattern

00	01	02	03	04	05	06	07	08
10	11	12	13	14	15	16	17	18
20	21	22	23	24	25	26	27	28
30	31	32	33	34	35	36	37	38
40	41	42	43	44	45	46	47	48
50	51	52	53	54	55	56	57	58
60	61	62	63	64	65	66	67	68
70	71	72	73	74	75	76	77	78
80	81	82	83	84	85	86	87	88

Fig. 4.4 One sample of BGRY CFA

This CFA arrangement is come from the idea of B and NB pixel located diagonally when NB light emitting. Since B filter is able to absorb some NB information, we can

improve the reconstructed NBI quality. Then the interpolation methods mentioned in last section are modified as following.

Bilinear Interpolation:
    Remain the same as equation 4.1.

Conventional Interpolation:
    Remain the same as equation 4.2.

Proposed Method (Use Y difference)
    The strategy of estimating G value at Y pixel is unable in this CFA. To recover another G sample is also not practical to run demosaicking. The chance is to estimate B value located at Y pixel, given by equation 4.6 and 4.7 [referring to Fig. 4.4]. And then reconstruct the mosaic data to full color image by proposed method.

$$\widetilde{B}_{34} = \frac{\alpha_{23}\widehat{B}_{23} + \alpha_{25}\widehat{B}_{25} + \alpha_{43}\widehat{B}_{43} + \alpha_{45}\widehat{B}_{45}}{\alpha_{23} + \alpha_{25} + \alpha_{43} + \alpha_{45}}$$

$$where \quad \widehat{B}_{23} = B_{23} + \frac{Y_{34} - Y_{12}}{2} \qquad \widehat{B}_{25} = B_{25} + \frac{Y_{34} - Y_{16}}{2} \qquad (4.6)$$

$$\widehat{B}_{43} = B_{43} + \frac{Y_{34} - Y_{52}}{2} \qquad \widehat{B}_{45} = B_{45} + \frac{Y_{34} - Y_{56}}{2}$$

$$\alpha_{23} = \frac{1}{1 + \left|B_{45} - B_{23}\right| + \left|B_{23} - B_{01}\right| + \left|Y_{34} - Y_{12}\right| + \left|\frac{G_{24} - G_{02}}{2}\right| + \left|\frac{R_{33} - R_{11}}{2}\right|}$$

$$\alpha_{25} = \frac{1}{1 + \left|B_{43} - B_{25}\right| + \left|B_{25} - B_{07}\right| + \left|Y_{34} - Y_{16}\right| + \left|\frac{G_{24} - G_{06}}{2}\right| + \left|\frac{R_{35} - R_{17}}{2}\right|}$$

$$\alpha_{43} = \frac{1}{1 + \left|B_{25} - B_{43}\right| + \left|B_{43} - B_{61}\right| + \left|Y_{34} - Y_{52}\right| + \left|\frac{G_{44} - G_{62}}{2}\right| + \left|\frac{R_{33} - R_{51}}{2}\right|} \qquad (4.7)$$

$$\alpha_{45} = \frac{1}{1 + \left|B_{23} - B_{45}\right| + \left|B_{45} - B_{67}\right| + \left|Y_{34} - Y_{56}\right| + \left|\frac{G_{44} - G_{66}}{2}\right| + \left|\frac{R_{35} - R_{57}}{2}\right|}$$

Proposed Method (Use YCbCr transformation)
    Step 1 to 4 remain the same. Withdraw the B plane from RGB color space and then insert all pixels to the place they located initially. Finally, execute the demosaicking algorithm. Note that the CFA is no longer RGGB Bayer pattern but BGRB pattern. Just change the sample location of Bayer pattern to GBRG and then exchange G and B plane while demosaicking. Remember to switch them back after demosaicking.

Likewise, the results of above-mentioned methods will display in next section.

4.2.3 Experimental Results

Now we proceed to compare those methods with different CFA arrangements. However, for the sake of convenience and easy-observing, we just compare them by the performance measurements of the average through 24 images in Fig. 3.24. Table 4.1, 4.2 and Fig. 4.5 show the results.

Table 4.1 Performance Measurements of Different Demosaicking Methods (RGYB CFA)

Measurements	Bilinear	Conventional	Proposed (Y difference)	Proposed (YCbCr Transform)
PSNR_R	28.0701	31.3356	33.9974	**38.5207**
PSNR_G	28.0625	29.9110	34.4936	**39.9715**
PSNR_B	29.3289	31.8822	34.2762	**37.5637**
Color Difference	3.1278	2.5041	1.4585	**1.1257**
SSIM	0.8616	0.9442	0.9665	**0.9820**

Table 4.2 Performance Measurements of Different Demosaicking Methods (BGRY CFA)

Measurements	Bilinear	Conventional	Proposed (Y difference)	Proposed (YCbCr Transform)
PSNR_R	28.0701	32.0054	34.6046	**35.8841**
PSNR_G	28.7070	30.0436	33.7196	**36.2494**
PSNR_B	28.7210	31.6096	33.8435	**36.5705**
Color Difference	3.2208	2.3534	1.6169	**1.4798**
SSIM	0.8597	0.9454	0.9613	**0.9708**

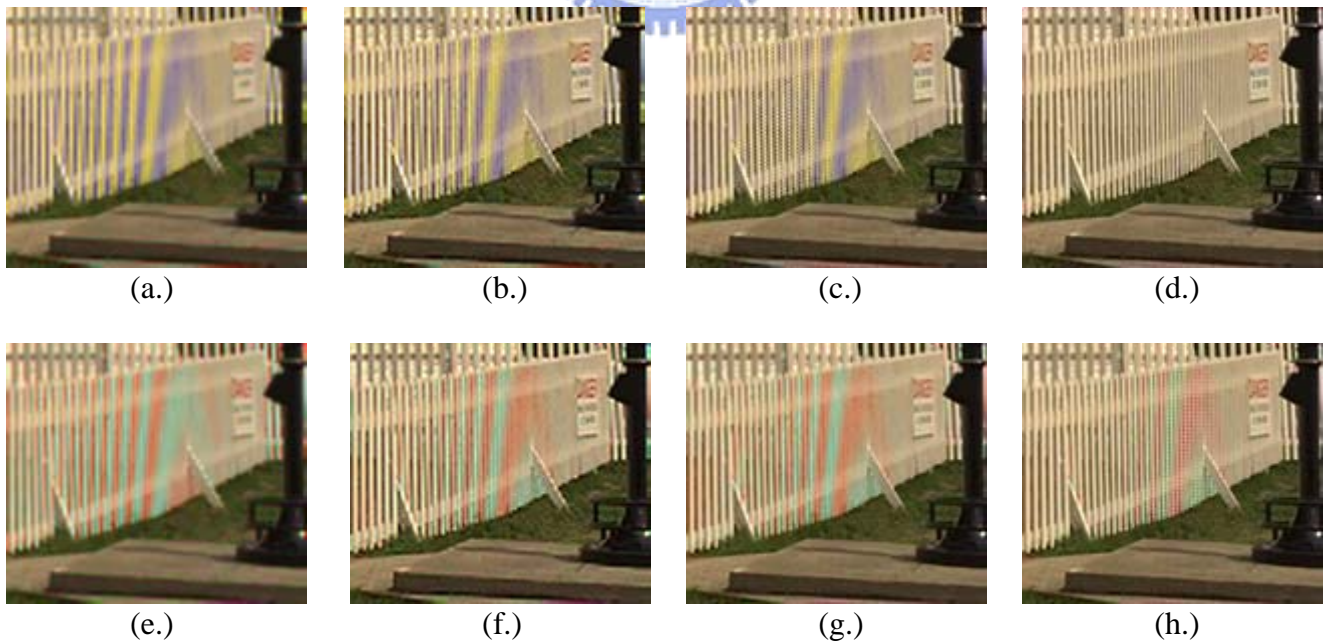| (a.) | (b.) | (c.) | (d.) |

| (e.) | (f.) | (g.) | (h.) |

Fig. 4.5 Demosaicking results of different methods based on different CFA

Methods: Bilinear, conventional, proposed (Y difference) and (YCbCr transform)

CFA: Upper row is RGYB CFA pattern and bottom row is BGRY CFA pattern

Since we only have three samples when reconstruct, it becomes easier to cause aliasing and artifacts. However, as shown in Fig. 4.5(a.)~(d.), we can achieve good performance by exploiting Y information to estimate G. Y contains more than half percentages of G element. So G values we estimated are reliable and close to the quantity from Bayer pattern. As a matter of result, we can recover the image almost without visual artifacts by three samples in 2-by-2 CFA. The measurements are record in Table 4.1. Through these methods, our proposed algorithm which uses YCbCr transformation performs better than others based on RGYB CFA.

For BGRY CFA, however, all methods seem not able to reduce artifacts as shown in Fig. 4.5(e.)~(h.). To reconstruct image by the pattern with two B samples and one R, G is differ from the perceptual of human. Recall that human eye is more sensitive to G component. Decrease the sampling rate of G and double the one of B are not practical and can not have good results at the same time. Besides, the strategy of using YCbCr transformation to enhance the color at same place is not as useful as the performance for RGYB CFA pattern according to Fig. 4.5(d.)(h.) and Table 4.2. That's because Y has the fewest B element. Use it to enhance B is limited to improvement.

As a result of the above experiments, we decide to choose RGYB CFA pattern as it closes to Bayer pattern and provides satisfied visual performance while demosaicking.

4.3 CFA with Narrow-band Information

As depicted in Fig. 4.1, the existing capsule endoscope system captures one WLI and one NBI and so on. According to the discussion of last section, the CFA is chosen to be RGYB and execute the demosaicking by the modified algorithm we proposed. Nonetheless, existing system has some drawbacks. In order to display NBI in color image, we will combine the WLI and NBI as discussed in section 1.2. So we run demosaicking and then do combination. Demosaicking may cause some quality loss to the input data. Besides, the most important point, the system is unable to combine the WLI and NBI at same location of each pixel since the capture time is actually not the same. This situation may bring about another damage of image quality. Therefore,
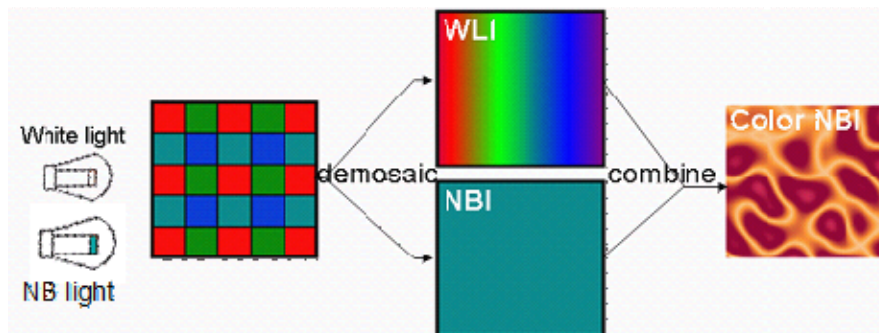

Fig. 4.6 Modification of existing capsule endoscope system

we attempt to do modifications of existing system. Fig. 4.6 depicted our idea. Depend on this structure, it is possible to have WLI and NBI at same location and also reduce the quality loss. At following sections, we still pay our attention on WLI demosaicking. However, it is difficult to experiment on demosaicking as we lack of the test images with NB information. We need to capture the test images with NB data by ourselves. The next section introduces the manufacture of test images. Then give some discussions about the arrangements of CFA. At last we make comparisons of these created test images.

4.3.1 Experimental platform

There are several principles of manufacturing the test image:

1) The capturing device sense the RGB color without demosaicking. That is, capture three color bands by three sensors.

2) There is no more process or modification of the data which device captured.

3) The data after capture must be save without compression, such as JPEG. The storage type should be the raw data (RAW).

4) Since we need NB information of the image, we capture two images exposed to white light and narrow-band light respectively. These two images must have same location. Besides, other capture conditions, such as ISO setting and shutter speed etc., are also to be the same.

The three former terms are related to the capture device. In order to fit these conditions, we choose the camera named "SIGMA DP1" to be our capture device. This special camera is able to sense all three color bands [44]. FOVEON X3 technology is the breakthrough of the sensors in this camera. FOVEON X3 is modified directly from the IC processing as depicted in Fig. 4.7. This is a stack of
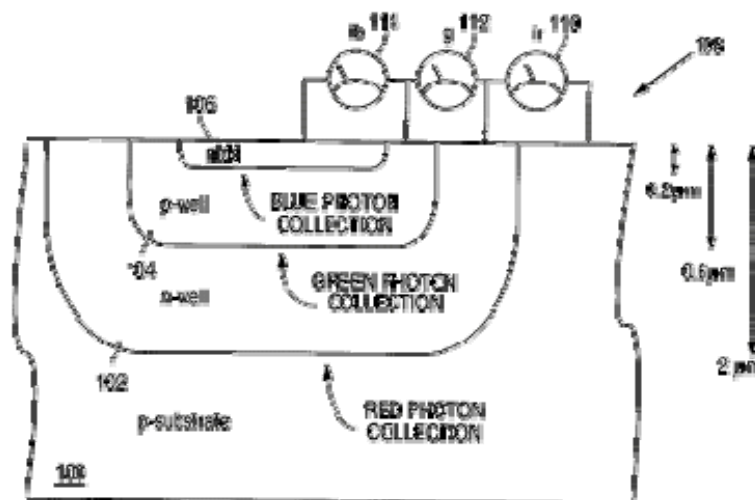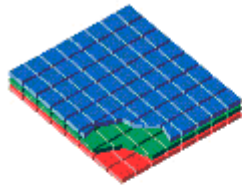

Fig. 4.7 The technology behind the X3 sensor[5]

---

[5] This figure refers to [46]

silicon which able to absorb different wavelengths of light. Fig. 4.8 best describes the difference between the traditional mosaic sensor and FOVEON X3. As a result, DP1
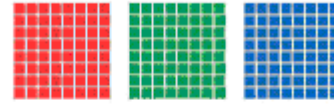

Foveon X3® Capture

A Foveon X3 direct image sensor features three separate layers of pixel sensors embedded in silicon.
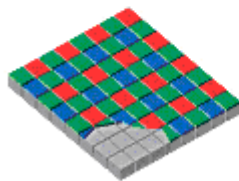
Since silicon absorbs different wavelengths of light at different depths, each layer records a different color. Because the layers are stacked together, all three colors are captured.

As a result, only Foveon X3 direct image sensors capture red, green, and blue light at every pixel location.

Mosaic Capture

In conventional systems, color filters are applied to a single layer of pixel sensors in a tiled mosaic pattern.
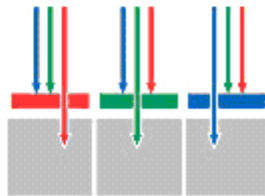
The filters let only one wavelength of light—red, green, or blue—pass through to any given pixel location, allowing it to record only one color.

As a result, mosaic sensors capture only 25% of the red and blue light, and just 50% of the green.

Fig. 4.8 The difference between the traditional mosaic sensor and FOVEON X3

which included this sensor can capture image with improved sharpness and immunity to color artifacts. Furthermore, it can play a competent role in our experiments

As for the light source, we need white light and narrow-band (NB) light while capturing image. Both of them are use SMD LED. Note that the NB light we used has the wavelength near 450nm. However, it is capable of covering the 415nm. Fig. 4.9(b.) displays the result of the NB light we used. We can

(a.)   (b.)
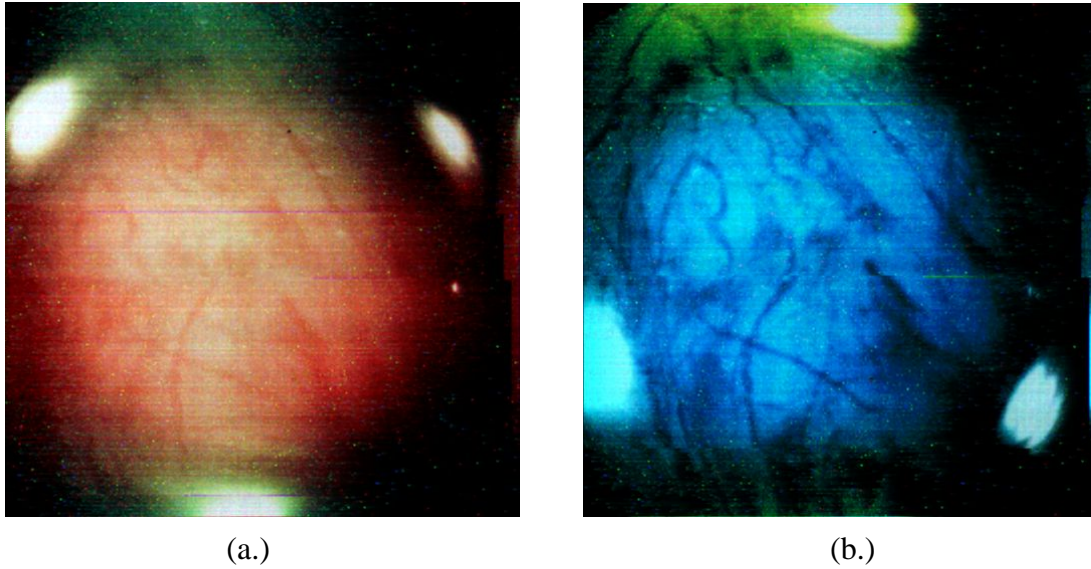
Fig. 4.9 Result of images exposed to white light and NB light, respectively[6]

observe the fine vessels under the mucosa clearly compared to Fig. 4.9(a.). Based on the same NB light, we organize the light source in rectangular lattice as depicted in Fig. 4.10. Just use the switch when changing to another light source.
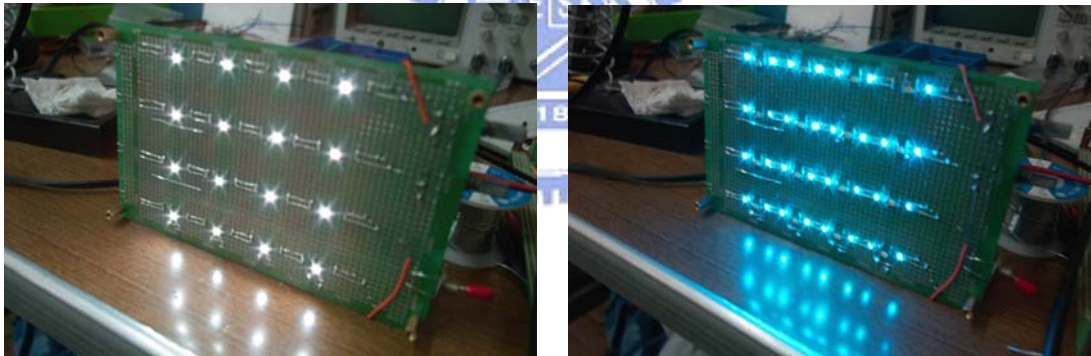
Fig. 4.10 Description of the light source (white and NB light) in our experiment

Next, we choose GretagMacbeth™ ColorChecker Color Rendition Chart to be our test pattern. As shown in Fig. 4.11, this chart contains 24 scientifically prepared

---

[6] These figures provided by Dr. S. M. Wu and courtesy of Chung-Shan Institute of Science and Technology.

Fig. 4.11 GretagMacbeth™ ColorChecker Color Rendition Chart
(each block is mark as 1 to 24, from the left-to-right, and top-to-bottom)

colored squares in a wide range of color. Besides, it is the industry standard color checking chart for cinematographers and photographers alike. Other characteristics in detail and waveform of each square can refer to [45]. Here we use this chart to be the pattern. Fig. 4.12 displays the results of the chart exposed to white and NB light captured by SIGMA DP1. Note that the capture parameters are ISO100, 0.25sec shutter speed, aperture value F4.0 and focal length of 16.6mm.


Fig. 4.12 Test image exposed to white and NB light respectively

4.3.2 RGNB CFA Pattern

00	01	02	03	04	05	06	07	08
10	11	12	13	14	15	16	17	18
20	21	22	23	24	25	26	27	28
30	31	32	33	34	35	36	37	38
40	41	42	43	44	45	46	47	48
50	51	52	53	54	55	56	57	58
60	61	62	63	64	65	66	67	68
70	71	72	73	74	75	76	77	78
80	81	82	83	84	85	86	87	88

Fig. 4.13 One sample of RGNB CFA

The CFA arrangements have been discussed in last section. The pattern which can reconstruct another G sample and build the estimated Bayer CFA can achieve a better result. Now the Y component has become to NB. We may wonder about the influence of NB so that all possible CFA arrangements will be discussed in this section.

Fig. 4.13 displays the arrangement similar to Bayer pattern. One G component is replaced with NB, just like the pattern in Fig. 4.2. Note that the NB information is acquired from the B plane of NB image. The interpolation algorithms are modified as below:

Bilinear Interpolation:

$$R_{R,G,B}(i, j) = I(i, j) * \frac{1}{4}\begin{bmatrix} 1 & 2 & 1 \\ 2 & 4 & 2 \\ 1 & 2 & 1 \end{bmatrix} \qquad (4.8)$$

Conventional Interpolation:

$$G - G_{lpf} = X - X_{lpf}, \ X = R \ or \ B \ or \ N$$
$$\Rightarrow G = G_{lpf} + \Delta X \qquad (4.9)$$

Proposed Method (Use N difference)

Refer to Fig. 4.13, estimate G value located at NB pixel by equation 4.10 and 4.11. Then reconstruct the mosaic data to full color image by proposed method based on the estimated Bayer CFA.

$$\widetilde{G}_{34} = \frac{\alpha_{23}\widehat{G}_{23} + \alpha_{25}\widehat{G}_{25} + \alpha_{43}\widehat{G}_{43} + \alpha_{45}\widehat{G}_{45}}{\alpha_{23} + \alpha_{25} + \alpha_{43} + \alpha_{45}}$$

$$where \ \ \widehat{G}_{23} = G_{23} + \frac{N_{34} - N_{12}}{2} \qquad \widehat{G}_{25} = G_{25} + \frac{N_{34} - N_{16}}{2} \qquad (4.10)$$

$$\widehat{G}_{43} = G_{43} + \frac{N_{34} - N_{52}}{2} \qquad \widehat{G}_{45} = G_{45} + \frac{N_{34} - N_{56}}{2}$$

$$\alpha_{23} = \cfrac{1}{1 + |G_{45} - G_{23}| + |G_{23} - G_{01}| + |N_{34} - N_{12}| + \left|\cfrac{R_{24} - R_{02}}{2}\right| + \left|\cfrac{B_{33} - B_{11}}{2}\right|}$$

$$\alpha_{25} = \cfrac{1}{1 + |G_{43} - G_{25}| + |G_{25} - B_{07}| + |N_{34} - N_{16}| + \left|\cfrac{R_{24} - R_{06}}{2}\right| + \left|\cfrac{B_{35} - B_{17}}{2}\right|} \qquad (4.11)$$

$$\alpha_{43} = \cfrac{1}{1 + |G_{25} - G_{43}| + |G_{43} - G_{61}| + |N_{34} - N_{52}| + \left|\cfrac{R_{44} - R_{62}}{2}\right| + \left|\cfrac{B_{33} - B_{51}}{2}\right|}$$

$$\alpha_{45} = \cfrac{1}{1 + |G_{23} - G_{45}| + |G_{45} - G_{67}| + |N_{34} - N_{56}| + \left|\cfrac{R_{44} - R_{66}}{2}\right| + \left|\cfrac{B_{35} - B_{57}}{2}\right|}$$

Proposed Method (Use YCbCr transformation)

Since we don't have Y information, this method is not available to use.

Experimental results of these methods will be compared in section 4.3.5.

4.3.3 BGRN CFA Pattern

00	01	02	03	04	05	06	07	08
10	11	12	13	14	15	16	17	18
20	21	22	23	24	25	26	27	28
30	31	32	33	34	35	36	37	38
40	41	42	43	44	45	46	47	48
50	51	52	53	54	55	56	57	58
60	61	62	63	64	65	66	67	68
70	71	72	73	74	75	76	77	78
80	81	82	83	84	85	86	87	88

Fig. 4.14 One sample of BGRN CFA

The algorithms based on this CFA are shown as following:

Bilinear Interpolation:

Remain the same as equation 4.8.

Conventional Interpolation:

Remain the same as equation 4.9.

Proposed Method (Use N difference)

The strategy remains the same while processed on BRGY CFA pattern. Estimate B value located at NB pixel firstly, given by equation 4.12 and 4.13 [referring to Fig. 4.14]. And then reconstruct the mosaic data to full color image by proposed method.

$$\widetilde{B}_{34} = \frac{\alpha_{23}\widehat{B}_{23} + \alpha_{25}\widehat{B}_{25} + \alpha_{43}\widehat{B}_{43} + \alpha_{45}\widehat{B}_{45}}{\alpha_{23} + \alpha_{25} + \alpha_{43} + \alpha_{45}}$$

$$where \quad \widehat{B}_{23} = B_{23} + \frac{N_{34} - N_{12}}{2} \qquad \widehat{B}_{25} = B_{25} + \frac{N_{34} - N_{16}}{2} \qquad (4.12)$$

$$\widehat{B}_{43} = B_{43} + \frac{N_{34} - N_{52}}{2} \qquad \widehat{B}_{45} = B_{45} + \frac{N_{34} - N_{56}}{2}$$

$$\alpha_{23} = \frac{1}{1 + |B_{45} - B_{23}| + |B_{23} - B_{01}| + |N_{34} - N_{12}| + \left|\dfrac{G_{24} - G_{02}}{2}\right| + \left|\dfrac{R_{33} - R_{11}}{2}\right|}$$

$$\alpha_{25} = \frac{1}{1 + |B_{43} - B_{25}| + |B_{25} - B_{07}| + |N_{34} - N_{16}| + \left|\dfrac{G_{24} - G_{06}}{2}\right| + \left|\dfrac{R_{35} - R_{17}}{2}\right|}$$

$$(4.13)$$

$$\alpha_{43} = \frac{1}{1 + |B_{25} - B_{43}| + |B_{43} - B_{61}| + |N_{34} - N_{52}| + \left|\dfrac{G_{44} - G_{62}}{2}\right| + \left|\dfrac{R_{33} - R_{51}}{2}\right|}$$

$$\alpha_{45} = \frac{1}{1 + |B_{23} - B_{45}| + |B_{45} - B_{67}| + |N_{34} - N_{56}| + \left|\dfrac{G_{44} - G_{66}}{2}\right| + \left|\dfrac{R_{35} - R_{57}}{2}\right|}$$

Likewise, experimental results are shown in section 4.3.5.

4.3.4 RGGN CFA pattern

This arrangement is originate from the following reasons:

1) Human eye is less sensitive to B.
2) The wavelength of NB is close to B. The information from NB may also covers B information.
3) G component is important in demosaicking. CFA with twice sampling rate of G can reserve the information of the scene the most.
4) Based on this structure, we can obtain a color image with NB information. No need to do another combination.

Due to these motivations, we decide to experiment on this pattern. RGGN CFA is depicted as Fig. 4.15.

Fig. 4.15 One sample of RGGN CFA pattern

Now, the most important thing we need to check is the effect of replacing B plane with NB information. We use the test pattern in Fig. 4.12 and change the B plane of white light image by the NB plane. Fig. 4.16 is the outcome. According to Fig. 4.16,

Fig. 4.16 Original image and the result of replace B with NB

although these two images look like almost the same, few colors between two figures are still dissimilar. To reveal the difference of color, the index introduced in section 2.3.2 is the best commentator. Table 4.3 shows this index and other measurements.

Table 4.3 Performance Measurement Comparison of Fig. 4.16

Measurements	
PSNR_Y	39.3997
Color Difference	8.6815
SSIM	0.9704

Note that we use PSNR of Y plane instead of PSNR of RGB since the PSNR of R and G are infinite.

As can be seen from Table 4.3, the PSNR is nearly 40dB but the color difference is 8.6815. This value is larger than 2.3 and even almost 4-times large. That is to say, these two images are out of MacAdam's ellipses (just noticeable regions) and can be recognize easily. The main problem of this phenomenon is the bandwidth of NB light.

74

Recall that NB light means the narrow-bandwidth of wavelength around 415nm (our NB is near 450nm). Now NB is playing the role of color filter. The bandwidth of blue filter is broad-band and therefore some signals that B absorbed can not be covered by NB as well [as shown in Fig. 4.17]. Take #10: purple color of Fig.4.11 for instance, the
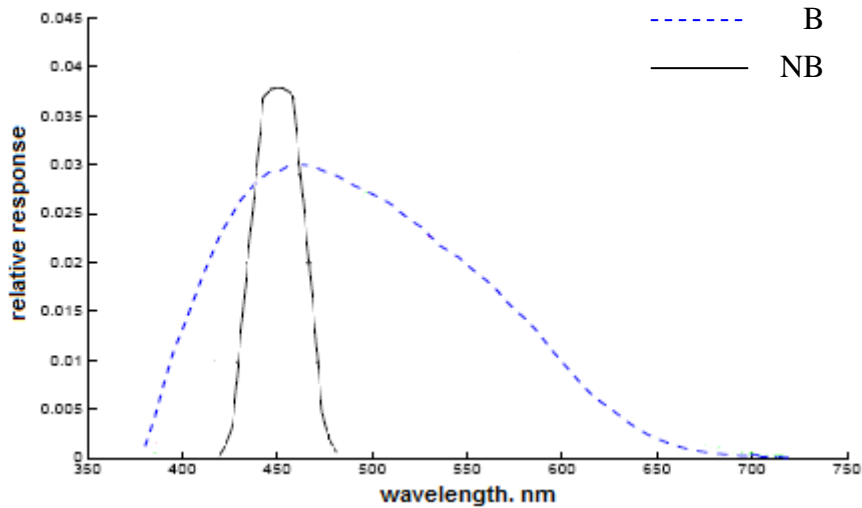
Fig. 4.17 Relative response of B and NB bands

waveform of this color is depicted as Fig. 4.18. The NB filter absorb less than B filter in the range near 400nm. Hence, the purple color under NB light is darker than under white light.
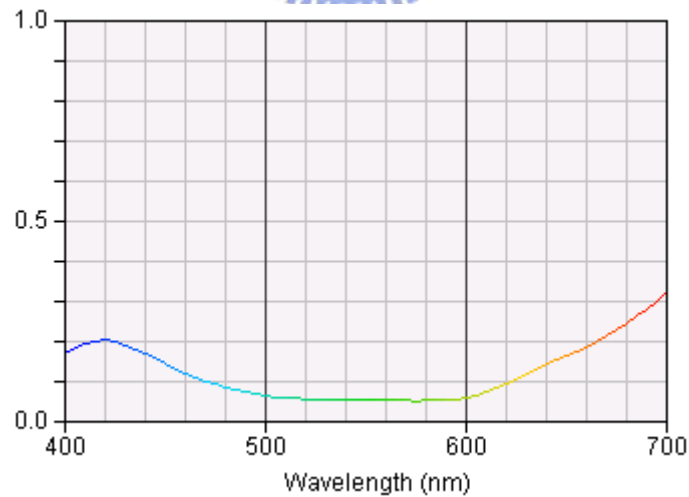

Fig. 4.18 Waveform of #10: purple color in colorchecker chart

As a conclusion, the RGGN CFA pattern is not practical to use. Nevertheless, we still process experiment based on this CFA. Result is shown in the next section.

4.3.5 Comparisons of test images

In order to increase the accuracy of experiments, we use not only Fig. 4.12, but also Fig. 4.19 to be the test patterns. Comparisons of different methods based on RGNB and BGRN CFA to those test images are recorded in Table 4.4 and 4.5. Note that the values in the following tables are the average of all images.
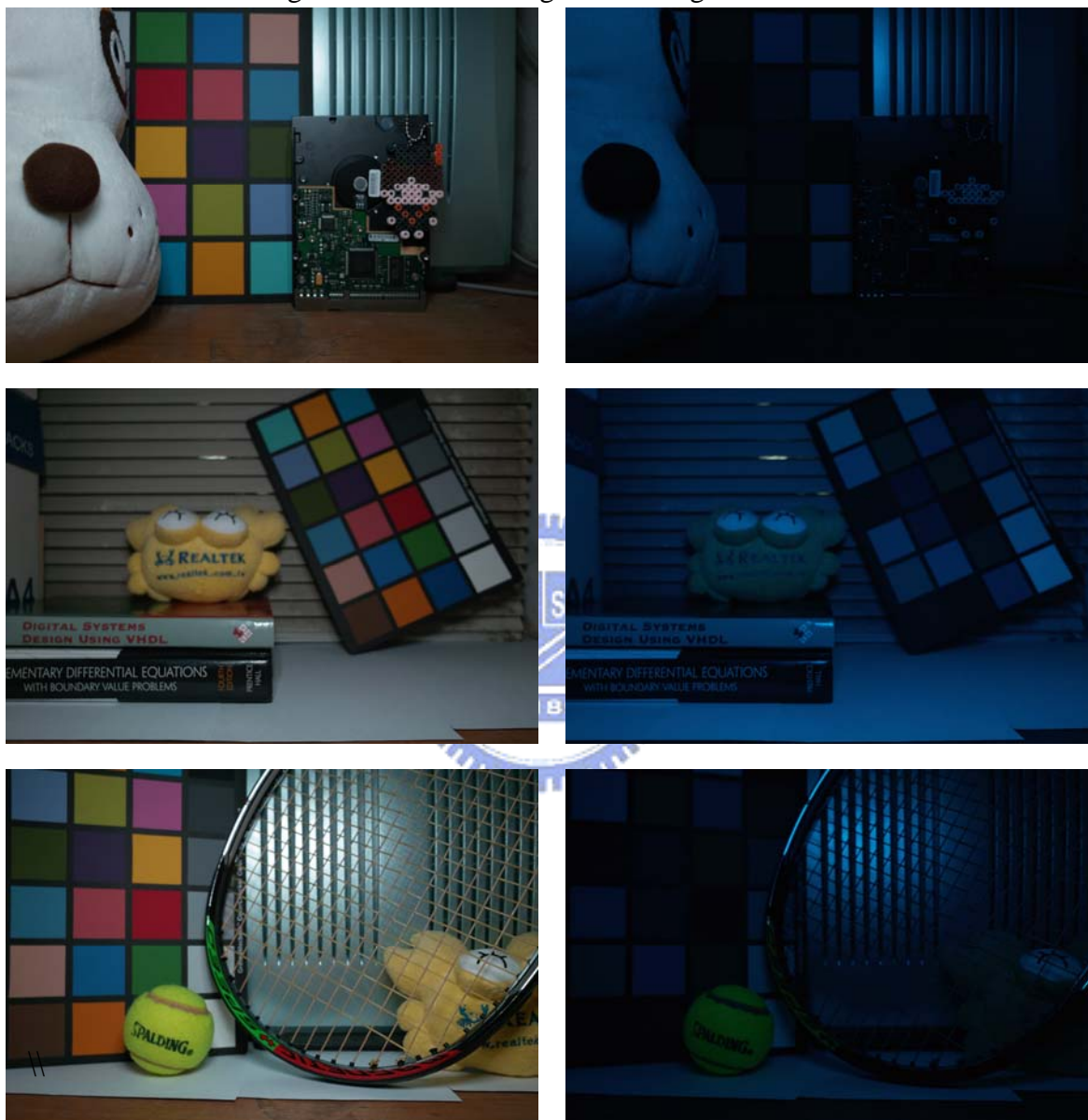
Fig. 4.19 Other test patterns exposed to white and NB light respectively

Table 4.4 Performance Measurements of Different Demosaicking Methods (RGNB CFA)

Measurements	Bilinear	Conventional	Proposed (N difference)
PSNR_R	41.5849	42.4228	**44.7847**
PSNR_G	41.7558	42.9830	**45.6170**
PSNR_B	41.6038	43.3175	**45.8580**
Color Difference	0.7827	0.7930	**0.6021**
SSIM	0.9869	0.9887	**0.9921**

Table 4.5 Performance Measurements of Different Demosaicking Methods (BGRN CFA)

Measurements	Bilinear	Conventional	Proposed (N difference)
PSNR_R	41.5849	41.8092	**44.3362**
PSNR_G	41.7600	43.1319	**44.7095**
PSNR_B	41.5851	43.3936	**45.4337**
Color Difference	0.8263	0.7974	**0.6312**
SSIM	0.9870	0.9880	**0.9921**

Table 4.6 Performance Measurements of Different Demosaicking Methods (RGGN CFA)

Measurements	Proposed (Y difference)
PSNR_R	46.3290
PSNR_G	51.0223
PSNR_B	14.8607
Color Difference	18.7986
SSIM	0.9034

Table 4.6 show the measurement values of proposed method based on RGGN CFA. According to Table 4.5 and 4.5, the algorithm we proposed can achieve better performance. Besides, the results of proposed method based on RGNB and BGRN are comparable. Just like the data in Table 4.1 and 4.2, without using YCbCr transformation, the effects on RGYB and BGRY are similar. Here, RGNB CFA is recommended since it provides better performance.

With regard to RGGN CFA, we have discussed this pattern as not practical. Table 4.6 presents its demosaicking result. Although the tremendous performance of PSNR_R and PSNR_G, other three indexes are terrible and even worse than bilinear interpolation. Therefore, this pattern does not take into consideration while demosaicking.

4.4 Influence about different brightness of NB image

While discussing the differences between each CFA arrangement in last section, we discover that there is a limitation about the brightness of NB image. That is to say, the brightness of NB plane can be neither too bright nor too dark. Fig. 4.20 and Table 4.7 describe this incident.

(a.)　　　　　　　　　　　　(b.)　　　　　　　　　　　　(c.)

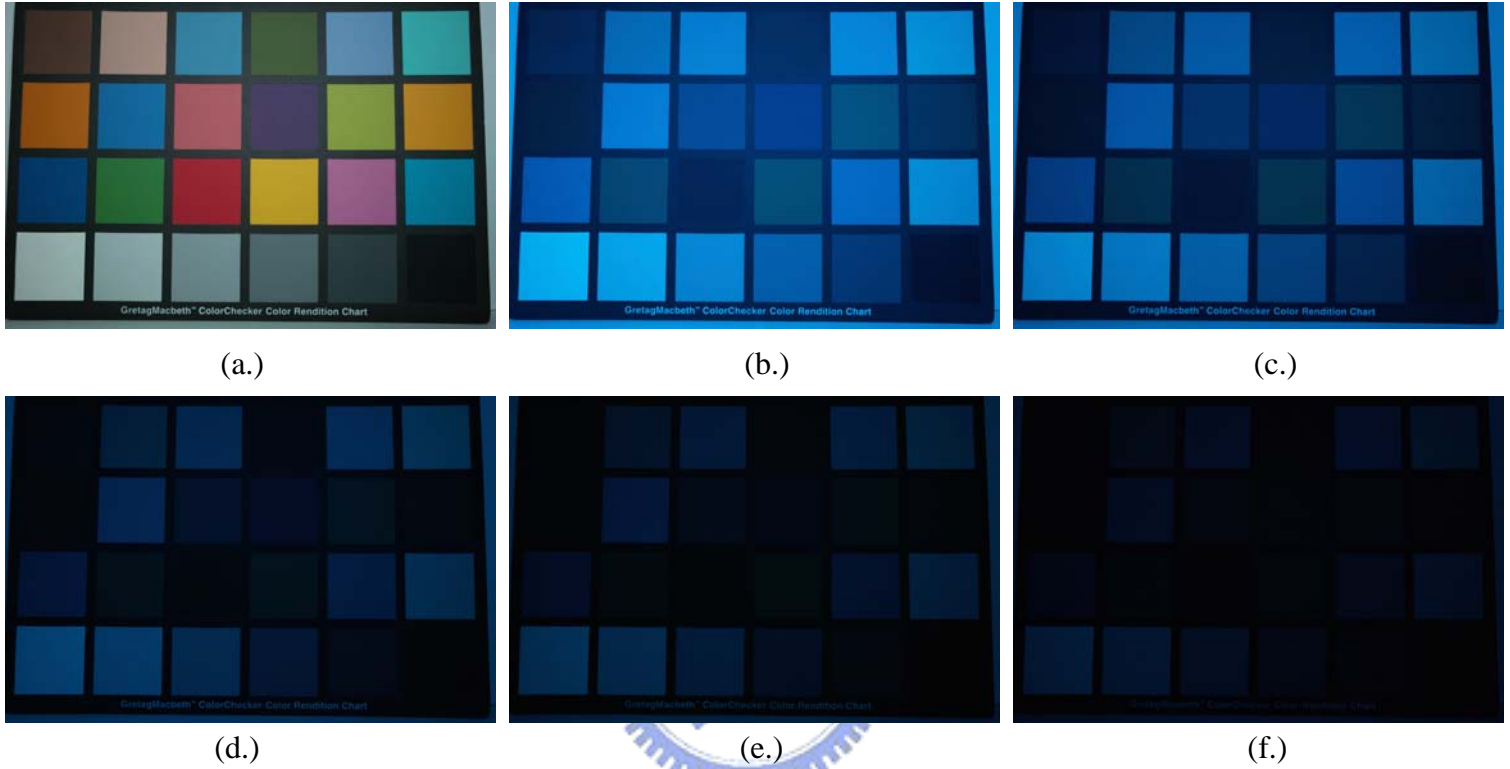(d.)　　　　　　　　　　　　(e.)　　　　　　　　　　　　(f.)

Fig. 4.20 Image exposed to white light and NB light with different brightness

Table 4.7 Performance Measurements of Fig. 4.20(a.) with different brightness of NB

RGNB CFA	Without NB info.	With Fig. 4.20(b.)	With Fig. 4.20(c.)	With Fig. 4.20(d.)	With Fig. 4.20(e.)	With Fig. 4.20(f.)
PSNR_R	46.5070	45.7743	46.6759	47.1085	47.0620	46.3814
PSNR_G	45.1351	44.2922	45.1766	45.8921	46.0167	44.4773
PSNR_B	45.4047	46.2761	46.1875	46.4870	46.5944	44.7034
Color Difference	0.4487	0.4929	0.4751	0.4599	0.4561	0.4722
SSIM	0.9933	0.9933	0.9934	0.9930	0.9930	0.9920

Refer to the data of Table 4.7, we believe there exists a valid region so that NB information can assist to improve quality. Review equation 4.10 of demosaicking on RGNB CFA pattern, we exploit the NB difference to help the reconstruction of G. However, according to the above table, the brightness of NB image should be proper. We bring up some questions here to this problem:

　　　　1) How much range does the NB information valid to use?

　　　　2) How much improvement does the NB information give?

　　　　3) How much are different CFA patterns affected?

To understand this problem, we proceed to do experiment with changeable brightness of NB image. We exploit histogram slide to adjust the brightness of NB image. Theoretically, extremely light or dark image can not improve image quality and even has same performance without NB information. We call this kind of image as saturation. Between these saturated brightness, there should be an effective region. Concerning the CFA arrangements, we choose RGNB and BGRN to experiment. As discussed in section 4.3, those two CFA arrangements can provide satisfied results. We do not subsume RGGN CFA in our discussion on accounting of its performance.

Fig. 4.21 is the tendency diagrams of Fig. 4.12 with different brightness based on RGNB and BGRN CFA respectively.
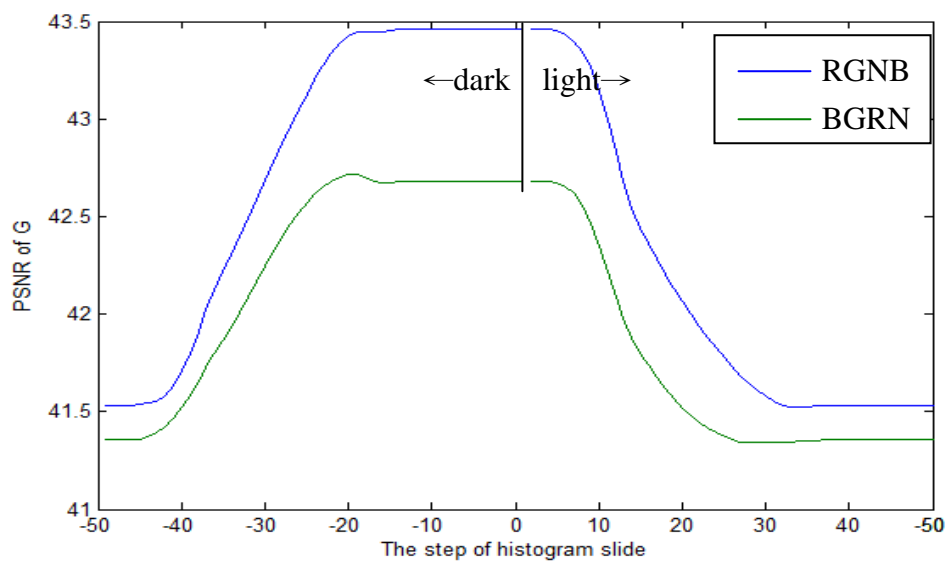

Fig. 4.21 PSNR of G to Fig. 4.12 with different brightness of NB image and different CFA

We define the valid region which can improve the quality of demosaicking without NB information at least 0.5 dB [see Fig. 4.22].
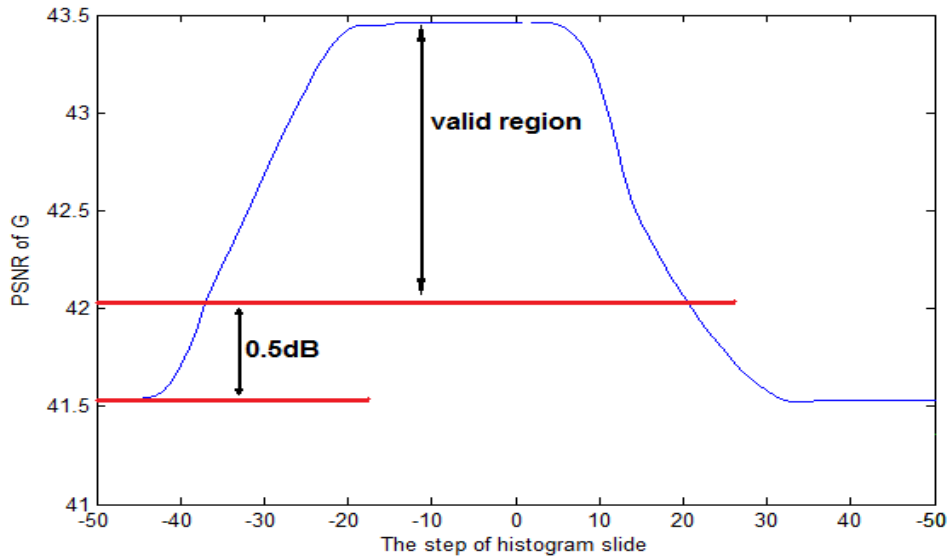
Fig. 4.22 Definition of valid region

According to this definition, RGNB CFA has the region $\in[-36 \quad 20]$. To explain it clearly, the valid field is allow 36 steps to dark of histogram slide and 20 steps to light. The region of BGRN CFA is $\in[-35 \quad 14]$. Although they have similar valid bound, utilize N information on RGNB CFA is capable of increasing image quality to 1.931dB than 1.3017dB of BGRN CFA. As a result, we still recommend RGNB CFA. Not only the better performance of demosaicking, but also the ability to increase quality more by NB information.

4.5 Results

Through lots of discussions in this chapter, we discover that the CFA which close to Bayer pattern can perform better. Both RGYB and RGNB CFA are similar to Bayer pattern. At the location of withdrawing G, we utilize the sensed signal to estimate G information so that Bayer pattern can be reproduced. Besides, other CFA arrangements are not able to reconstruct Bayer pattern since the withdrawing G are not at the diagonal direction with observed G. Although we use the same way to estimate another color (R or B) at withdrawing G, the results are become worse. Since human eye is more sensitive to G compared to R and B, the performance with twice sampling rate of G would be better than others.

Chapter 5 *Conclusion and Future Work*

5.1 Conclusion

In this thesis, we presented a recursive demosaicking algorithm both for Bayer pattern and for narrow-band gastrointestinal image. This method contains two successive steps: the interpolation step and the post-processing step. The first step is use the weighted sum interpolation to reconstruct along different directions. Then it upgrades the plane adaptively by exploiting the strong correlation of the detail subbands and use homogeneity map to choose the direction with fewer color artifacts. The second stage is composed of two different kinds of post-processing. Arrange them technically by the property of each post-processing can provide satisfactory results in suppressing those artifacts. Furthermore, to avoid the artifacts that may cause by too many iterations, we set a stop criterion to judge the image is suitable to execute post-processing or not. The proposed algorithm was compared with other existing methods; it showed a better quality both visually and in terms of performance measurement.

As for the narrow-band gastrointestinal image, we modify the demosaicking algorithm corresponding to specific CFA. According to experiments, our proposed method is able to achieve satisfied performance based on only three samples in 2-by-2 CFA block. Besides, lots of discussion and experiments have been done to discover the differences of CFA arrangements. We conclude RGNB is the best choice since it can provide better image quality among several of CFA arrangements. Besides, it is similar to Bayer pattern and has the ability to increase image quality more by NB information. Therefore, we recommend RGNB to be the CFA of narrow-band gastrointestinal endoscope system.

5.2 Future work

There are some extensions about this dissertation. The first one is about demosaicking strategy. If the performance improvement between recursive approach and bilinear interpolation is fewer in particular region, we can just use bilinear interpolation. That is to say, while process in flat region which does not have high-frequency component, we can simply run bilinear interpolation. When encounter the artifacts-prone area, and then use more complicate and more useful algorithm. According to this skill, we can be able to save lots of computation time and reduce the complexity. But the question is how to recognize between the low-frequency and

high-frequency region? This is another research material.

The second one is about the narrow-band gastrointestinal image endoscopic system. Our ideal is to display color NBI. But the current combination way is designed so that 415nm image is assigned to B and G plane and 540 nm image is assigned to R plane. However, the color of this image is pseudo-color. If we capture the image by emitting white light and NB light simultaneously [see Fig. 5.1], we can obtain the normal color which human perceived normally while demosaicking. But the influences of emitting white light and NB light at the same time are being ambiguous. This problem is left as a future work.
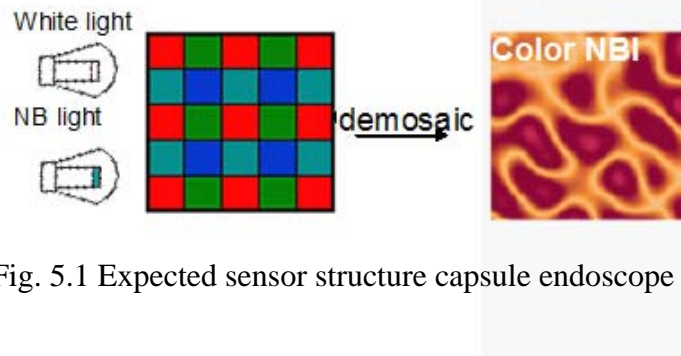

Fig. 5.1 Expected sensor structure capsule endoscope system

References

[1] B. E. Bayer, "Color imaging array," U.S. Patent 3 971 065, July 1976.

[2] B. K. Gunturk, J. Glotzbach, Y. Altunbasak, R. W. Schafer, and R. M. Mersereas, " Demosaicking: color filter array interpolation," *IEEE Signal Process. Mag.*, vol. 22, no. 1, pp. 44-54, Jan. 2005.

[3] R. Kimmel, "Demosaicing: image reconstruction from color CCD samples," *IEEE Trans. Image Processing*, vol. 7, no. 3, pp. 1221-1228, Sep. 1999.

[4] D. Cok, "Signal processing method and apparatus for producing interpolated chrominance values in a sampled color image signal," U.S. Patent 4 642 678, Feb. 1987.

[5] J. E. Adams, "Interactions between color plane interpolation and other image processing functions in electronic photography," *Proc. SPIE*, vol. 2416, pp. 144-151, Feb. 1995

[6] T. Kuno, H. Sugiura, and N. Matoba, "New interpolation method using discriminated color correlation for digital still cameras," *IEEE Trans. Consumer Electron.*, vol. 45, no. 1, pp. 259-267, Feb. 1999.

[7] T. Usui *et al.*, "Studies on image coding using correlation between lightness and chrominance," *Color forum JAPAN '98*, 10-3, 133-136, 1998.

[8] T. W. Freeman, "Median filter for reconstructing missing color samples," U.S. Patent 4 724 395, 1988.

[9] S. Moriya *et al.*, "Advanced demosaicking method based on the changes of colors in a local region," *IEEE Trans. Consumer Electron.*, vol. 52, no. 1, pp. 206-214, Feb. 2006

[10] W. Lu and Y. P. Tan, "Color filter array demosaicking: new method and performance measures," *IEEE Trans. Image Processing*, vol. 12, no. 10, pp. 1194-1210, Oct. 2003

[11] C. Laroche and M. Prescott, "Apparatus and method for adaptively interpolation a full color image utilizing chrominance gradients," U.S. Patent 5 373 322, Dec. 1994.

[12] J. Hamilton and J. Adams, "Adaptive color plane interpolation in single sensor color electronic camera," U.S. Patent 5 629 734, May 1997.

[13] J. Adams, "Design of practical color filter array interpolation algorithms for digital cameras," *Proc SPIE*, vol. 3028, pp. 117-125, Feb. 1997

[14] X. Li and M. T. Orchard, "New edge-directed interpolation," *IEEE Trans. Image Processing*, vol. 10, no. 10, pp. 1521-1527, Oct. 2001

[15] B. K. Gunturk, Y. Altunbasak, and R. M. Mersereau, "Color plane interpolation using alternating projections," *IEEE Trans. Image Processing,* vol. 11, no. 9, pp.

997-1013, Sep. 2002.

[16] H. A. Chang and H. H. Chen, "Stochastic color interpolation for digital cameras," *IEEE Trans. Circuit and systems for video technology,* vol. 17, no. 8, pp. 964-973, Aug. 2007.

[17] H. J. Trussell and R. E. Hartwig, "Mathematics for demosaicking," *IEEE Trans. Image Processing*, vol. 3, no. 4, pp. 485-492, Apr. 2002.

[18] L. Zhang and X. Wu, "Color demosaicking via directional linear minimum mean square-error estimation," *IEEE Trans. Image Processing*, vol. 14, no. 12, pp. 2167-2178, Dec. 2005

[19] D. D. Muresan and T. W. Parks, "Adaptively quadratic (AQua) image interpolation," *IEEE Trans. Image Processing*, vol. 13, no. 5, pp. 690-698, May 2004.

[20] X. Li, "Demosaicing by successive approximation," *IEEE Trans. Image Processing*, vol. 14, no. 3, pp. 370-379, Mar. 2005.

[21] X. Wu and L. Zhang, "Temporal color video demosaicking via motion estimation and data fusion," *IEEE Trans. Circuit Syst Video Technl*, vol. 16, no. 2, pp. 231-240, Feb. 2006.

[22] K. Hirakawa and T. W. Parks, "Adaptive homogeneity-directed demosaicking algorithm," *IEEE Trans. Image Processing,* vol. 14, no. 3, pp. 360-369, Mar. 2005.

[23] D. Alleysson, S. Süsstrunk and J. Hérault, "Linear demosaicing inspired by the human visual system," *IEEE Trans. Image Processing,* vol. 14, no. 4, pp. 439-449, Apr. 2005.

[24] "Recommendations of uniform color space, color difference equations, psychrometric color terms," CIE, Supplement no. 2 to CIE publication no. 15(E.-1 31) 1971/(TC-1.3), 1978.

[25] M. Mahy, E. Van, and O. A., "Evaluation of uniform color spaces developed after the adoption of CIELAB and CIELUV," *Color Res. Application*, vol. 19, no. 2, pp. 105-121, 1994.

[26] [Online] Available: http://www.cs.technion.ac.il/~ron/Demosaic/

[27] K. Gono, "Multifunctional endoscopic imaging system for support of early cancer diagnosis," *IEEE Journal of Selected Topics in Quantum Electronics*, vol. 14, no. 1, pp. 62-69, Jan.-Feb. 2008.

[28] K. Gono, K. Yamazaki, N. Doguchi, T. Obi, M. Yamagichi, N. Ohyama, H. Machida, Y. Saono, S. Yoshida, Y. Hamamoto, and T. Endo, "Endoscopic observation of tissue by narrowband illumination," *Opt. Rev.*, vol. 10, pp. 211-215, 2003.

[29] K. Gono, T. Obi, M. Yamaguchi, N. Ohyama, H. Machida, Y, Sano, S. Yoshida, Y.

Hamamoto, and T. Endo, "Appearance of enhanced tissue features in narrowband endoscopicimagine," *J. Biomed. Opt.*, vol. 9, pp. 568-577, May/Jun. 2004.

[30] D. L. MacAdam, *Selected Papers on Colorimetry Fundamentals*, SPIE Milestone Series, Bellingham, WA, USA, 1993.

[31] E. R. Kandal, J. H. Schwartz and T. M. Jessell, *Principle of Neutral Science*, 4th ed., pp. 507-513, McGraw-Hill, NY, USA, 2000.

[32] R. C. Gonzalez and R. E. Woods, *Digital Image Processing,* 3rd ed., pp. 395, Pearson Prentice-Hall, Inc., USA, 2007.

[33] G. Sharma and H. J. Trussell, "Digital color imaging," *IEEE Trans. Image Processing*, vol. 6, no. 7, pp. 901-932, July, 1997.

[34] J. Guild, "The colorimetric properties of the spectrum," *Philosophical Trans. of the Royal Society of London*, vol. 230, pp. 149-187, 1931.

[35] A. C. Harris and I. L. Weatherall, "Objective evaluation of colour variation in the sand-burrowing beetle *Chaerodes trachyscelides* White (*Coleoptera: Tenebrionidae*) by instrumental determination of CIELAB values," Journal of the Royal Society of New Zealand, vol. 20, no. 3, pp. 253-259, Sep. 1990.

[36] [Online] Available: http://www.color.org/sRGB.xalter

[37] M. S. Kiver, *Color Television Fundamentals*, pp. 323, McGraw-Hill, NY, USA, 1964.

[38] [Online] Available: http://www.fho-emden.de/~hoffmann/ciexyz29082000.pdf

[39] Z. Wang, A. C. Bovik, H. R. Sheikh and E. P. Simoncelli, "Image quality assessment: From error visibility to structural similarity," *IEEE Trans. Image Proc.*, vol. 13, no. 4, pp. 600-612, Apr. 2004.

[40] B. Girod, "What's wrong with mean-squared error," in *Digital Images and Human Vision*, A. B. Watson, Ed. Cambridge, MA: MIT Press, 1993, pp.207-220.

[41] A. M. Eskicioglu and P. S. Fisher, "Image quality measures and their performance," *IEEE Trans. Commun.*, vol. 43, pp. 2959-2965, Dec. 1995.

[42] [Online] Available: http://www.ece.uwaterloo/%7Ez70wang/research/ssim/

[43] K. Topfer, J. E. Adams and B. W. Keekan, "Modulation transfer functions and aliasing patterns of CFA interpolation algorithms," *Proc. IS&T PICS*, pp. 367-370, Portland, OR, 1998.

[44] R. Lyon and P. Hubel, "Eyeing the camera: Into the next century," *IS&T/TSID 10th Color Imaging Conf. Proceedings*, pp. 349-355, Scottsdale, AZ, USA, 2002.

[45] [Online] Available: http://www.brucelindbloom.com/index.html?ColorCheckerC alculator.html

[46] R. B. Merrill, "Color separation in an active pixel cell imaging array using a triple-well structure," U.S. Patent 5 965 875, Oct. 1999.